МІНІСТЕРСТВО ОСВІТИ І НАУКИ УКРАЇНИ
ДВНЗ «УЖГОРОДСЬКИЙ НАЦІОНАЛЬНИЙ УНІВЕРСИТЕТ»

НАУКОВИЙ ВІСНИК
УЖГОРОДСЬКОГО УНІВЕРСИТЕТУ

СЕРІЯ
«ФІЗИКА»

Науковий журнал

Випуск 51
2022

УЖГОРОД
2022

ISSN 2415-8038

Засновником журналу Науковий вісник Ужгородського університету. Серія «Фізика» є
ДВНЗ «Ужгородський національний університет», фізичний факультет
та Закарпатське фізичне товариство

Рекомендовано до друку та поширення
через мережу Інтернет Вченою Радою
ДВНЗ «Ужгородський національний університет»
(протокол № 6 від 21 червня 2022 р.)

Свідоцтво про державну реєстрацію
друкованого засобу масової інформації
Серія КВ № 7972 від 09.11.2003 р.

Збірник входить до переліку фахових видань України
Категорія: Б. Науки: фізико-математичні. Спеціальності: 104 – Фізика та астрономія,
105 – Прикладна фізика та наноматеріали
(Наказ Наказ Міністерства освіти і науки України від 11.07.2019 р. № 975)

Збірник представлено у міжнародних наукометричних базах даних,
репозиторіях та пошукових системах: Google Scholar, BASE, НБУ ім. В.І. Вернадського,
Crossref, OpenAIRE, WorldCat

Науковий вісник Ужгородського університету. Серія «Фізика» / за ред. В.М. Різака та ін.
Ужгород: ДВНЗ «Ужгородський національний університет», 2022. Вип. 51. 88 с.

Адреса редакції:
ДВНЗ «Ужгородський національний університет»
88000, вул. Волошина, 54, м. Ужгород
Закарпатська область, Україна
тел/факс: (03122) 3-20-24
E-mail: info@physics.uz.ua
www: https://physics.uz.ua/uk

MINISTRY OF EDUCATION AND SCIENCE
OF UKRAINE UZHHOROD NATIONAL UNIVERSITY

SCIENTIFIC HERALD
OF UZHHOROD UNIVERSITY

SERIES
“PHYSICS”

Scientific Journal

Issue 51
2022

UZHHOROD
2022

ISSN 2415-8038

The journal Scientific Herald of Uzhhorod University. Series “Physics” is founded
by Faculty of Physics, Uzhhorod National University
and Transcarpathian Physical Society

*Recommended for printing and distribution
via the Internet by the Academic Council
of Uzhhorod National University
(Minutes No. 6 of June 21, 2022)*

**Certificate of state registration
of the print media**
Series KV No. 7972 of 09.11.2003

The collection is included in the list of professional publications of Ukraine
Category: B. Branch of Sciences: Physics and Mathematics. Specialty: 104 – Physics and Astronomy, 105 – Applied Physics and Nanomaterials
(Order of the Ministry of Education and Science of Ukraine of 11.07.2019 No. 975)

The collection is presented international scientometric databases, repositories and scientific systems: Google Scholar, BASE, VNLU, Crossref, OpenAIRE, WorldCat

Rizak V.M., et al. Scientific Herald of Uzhhorod University. Series “Physics”. Issue 51. Uzhhorod: Uzhhorod National University; 2022. 88 p.

The address of editorial board:
Uzhhorod National University
88000, 54 Voloshyn Str., Uzhhorod
Transcarpathian region, Ukraine
Tel./fax: (03122) 3-20-24
E-mail: info@physics.uz.ua
www: https://physics.uz.ua/en

НАУКОВИЙ ВІСНИК УЖГОРОДСЬКОГО УНІВЕРСИТЕТУ. СЕРІЯ «ФІЗИКА»
ВИПУСК 51

Редакційна колегія

SCIENTIFIC HERALD OF UZHHOROD UNIVERSITY. SERIES "PHYSICS"
ISSUE 51

Editorial Board

НАУКОВИЙ ВІСНИК УЖГОРОДСЬКОГО УНІВЕРСИТЕТУ. СЕРІЯ «ФІЗИКА»
ВИПУСК 51

ЗМІСТ

SCIENTIFIC HERALD OF UZHHOROD
UNIVERSITY. SERIES “PHYSICS”
ISSUE 51

CONTENTS

Scientific Herald of Uzhhorod University Series "Physics"

Journal homepage: https://physics.uz.ua/en

Issue 51, 9-17

Received: 05.04.2022. Revised: 19.05.2022. Accepted: 08.06.2022

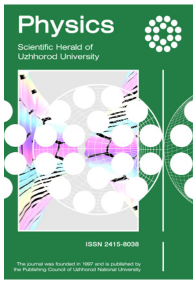

UDC 533
PACS 87.15.K
DOI: 10.54919/2415-8038.2022.51.9-17

Mass Spectrometric Studies of Valine Molecules by Electron Shock in the Gas Phase

Alla Bulhakova*

Institute of Electron Physics of the NAS of Ukraine
88017, 21 Universitetska Str., Uzhhorod, Ukraine

Abstract

Relevance. Valine is one of the eight amino acids not synthesised by the human body, necessary for the synthesis and growth of body tissues, muscle coordination; regulation of nervous processes, nitrogen metabolism, and stabilisation of the hormonal background. Since α-amino acids contain an asymmetric carbon atom, they can exist as optical isomers (mirror antipodes) that play an essential role in protein biosynthesis. The structure of matter and the physical processes that occur in it are studied using the method of mass spectrometry and spectral analysis. This indicates the relevance of the problem that was studied in this paper.

Purpose. Mass spectrometric studies of the formation of ionic products of single and dissociative ionisation of the valine molecule ($C_5H_{11}NO_2$) with electrons according to the method of beams intersecting within the energy range of bombarding electrons 6-70 eV. To consider the mechanisms of formation of the most intense ion fragments during dissociative ionisation by electron shock.

Methods. The experiment was conducted on an installation with a monopole mass spectrometer of the MX-7304A type, which belongs to the class of dynamic mass analysers with electron shock ionisation in the range of mass numbers 0-120 Da. The mass spectra of molecules were investigated at different temperatures of the source of molecules in the range of 300-600 K.

Results. The obtained results are compared with the mass spectra of the D-, L-, and DL-enantiomeric forms of the valine molecule with data from the NIST and SDBS databases. The features of the processes of formation of ion fragments of valine molecules by electronic shock are analysed in detail, and the dynamics of the yield of ion fragments in the range of evaporation temperatures of the initial substance of 300-440 K is also studied. The total relative ionisation cross-section of the molecule under study was measured according to mass spectrometric method with an ionising electron energy of 5-60 eV. Based on the results of experimental studies, a threshold section of the dependence of the total relative cross-section of valine ionisation is determined and given in this paper.

Conclusions. A detailed analysis of the processes of formation of fragment ions in the mass spectra allows demonstrating the influence of the structural forms of valine enantiomers on the redistribution of relative intensities of product ions

Keywords: electron, mass spectrometry, ionisation, amino acid

Suggested Citation:
Bulhakova A. Mass spectrometric studies of valine molecules by electron shock in the gas phase. *Scientific Herald of Uzhhorod University. Series "Physics"*. 2022;(51):9-17.

*Corresponding author

Introduction

Among all the molecules present in a living cell, the first place is occupied by proteins that account for at least half of the dry weight of the cell. Proteins perform various functions and serve as molecular tools by which genetic information finds its real embodiment. To build all proteins, whether they are proteins from the oldest bacteria or from higher organisms, the same set of 20 amino acids is used, covalently bound to each other in a certain sequence inherent only in this protein. Each amino acid, due to the specific features of its side chain, has a chemical individuality [1].

Valine is one of the eight amino acids not synthesised by the human body. At the same time, this aliphatic α-amino acid is necessary for the synthesis and growth of body tissues, muscle coordination; regulation of nervous processes, nitrogen metabolism, and stabilisation of the hormonal background [2]. Valine belongs to a group of simple aliphatic nonpolar α-amino acids that exist as various conformers. Two types of amino acid isomerism are known: structural isomerism, which is associated with the structural features of the carbon skeleton and the relative location of functional groups, and optical isomerism (spatial). Since α-amino acids contain an asymmetric carbon atom, they can exist as optical isomers (mirror antipodes) that play an essential role in protein biosynthesis.

The structure of matter, mechanisms, and features of physical processes occurring in it are investigated using methods of interaction with slow electrons, which include electron mass spectroscopy, i.e., the study of mass spectra, temperature dependences of the occurrence of positive ion fragments, dissociative ionisation of amino acid molecules under the action of low-energy (430 eV) electrons and determination of the appearance energies of ionised fragments [3; 4]. This indicates the relevance of the problem that was studied in this paper.

Ionising radiation, interacting with a living organism, can cause various changes in the genotype due to its effect on the genetic DNA and RNA macromolecules. This radiation, penetrating the body, generates streams of low-energy secondary electrons, the energy of which can range from 0.1 to tens of electron volts [5]. Secondary electrons initiate the processes of excitation [6; 7] and ionisation [8], which lead to destructive changes in DNA and RNA. According to the existing ideas [9], it is with slow electrons that the main part of destructive changes at the molecular level of biostructures is associated, and the main target is genetic macromolecules [10]. Assessment of the effects of physical excitation and ionisation processes caused by electron shock in biostructures requires obtaining information about the most probable channels of fragmentation of biomolecules. This was one of the tasks of this study.

The purpose of this paper was to investigate the process of electron ionisation of valine molecules in the gas phase according to mass spectrometric method at different evaporation temperatures of the first substance. It was also important to compare the relative intensities of practically all the peaks of the mass spectra obtained in this study with data from other authors and from the well-known NIST and SDBS databases. A detailed analysis of the processes of formation of fragment ions in the mass spectra allows demonstrating the influence of the structural forms of valine enantiomers on the redistribution of relative intensities of product ions.

Materials and Methods

The experiment was performed on a monopole mass spectrometer MX 7304A, which was described in detail earlier [8; 11]. This mass spectrometer is a single-pole version of the quadrupole analytical instrument and comprises an ion source, an analysis system, and a useful signal detection system. This device was placed in a vacuum installation with oil-free pumping. The system provided a residual gas vapour pressure of at least 210^{-6} Torr in working conditions. The ion source of the mass spectrometer allowed obtaining electron beams of regulated energy from 6 to 70 eV, a current in the range of 0.05-0.5 Ma, with a minimum energy spread of DE½ = 200 meV, where this value is the full width at half the maximum electron energy distribution. The range of recorded masses was 1-120 DA, with a resolution not worse than $\Delta M = 1$ Da. The concentration of the valine molecules under study in the region of interaction with electrons was $10^{10} \div 10^{11}$ cm^{-3}. The temperature of the source of molecules was maintained in the range of 300-600 K [2].

The mass scale was calibrated for isotopes of Ar and Xe atoms, and control mass spectra were measured for freon, sulphur hexafluoride, and krypton. The energy scale was calibrated from the initial section of the ionisation section of the Kr atom, which allowed determining the electron energy with an accuracy of ± 0.08 eV.

Valine of the Sigma Aldrich company was used for research (purity 0.999, No. CAS72-18-4, the presence of water molecules was excluded). The structural formula of valine is represented by in Figure 1A. The experiment was carried out in two stages: at the first stage, mass spectra in the range of 1-120 Da were carefully measured at ionisation energies (E_i) 20, 30, 40, 50 and 70 eV, and in the second case, the energy dependences of the relative dissociative ionisation cross-sections of the valine molecule were measured in the energy range of ionising electrons from 5 to 60 eV. The measurement method was reduced to simultaneous measurement of fragment ions; for this, the energy range was first set, then the test masses were set (no more than 20), and the total measurement time was calculated using the Formula (1):

$$T_{full} = t_1 \times n \times C \qquad (1)$$

where t_1 is the measurement time of a single fragment; n is the number of fragments; C is the number of cycles determined depending on the value of the useful signal.

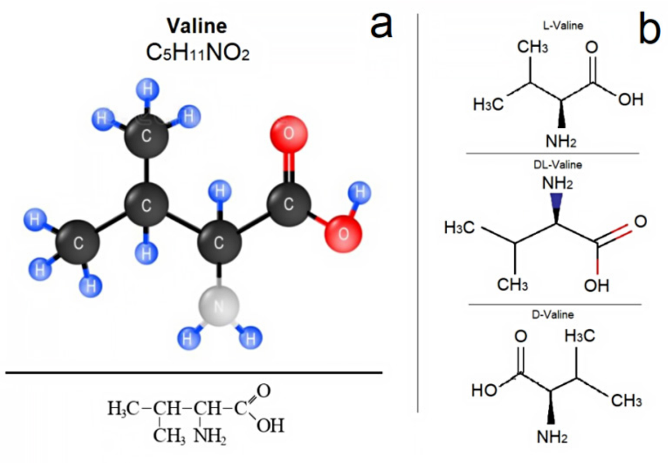

Figure 1. (a) structural formulas of valine and its enantiomers L-, DL-, and (b) D-forms

Results and Discussion

Before proceeding to the discussion of the results, it is advisable to consider the structural diagrams of the valine $C_5H_{11}NO_2$ molecule shown in Figure 1 and its enantiomers of L-, DL-, and D-forms. A distinctive feature of the valine molecule is the presence of hydrogen atoms bound to 4 substitutes, namely the 1st is a hydrogen atom, the 2nd is a carboxyl COOH group, the 3rd is an NH_2 amino group, the 4th, the most significant is an alkyl group, i.e., a side chain of Cα atoms, the composition of which determines the main properties of this amino acid. Valine enantiomers should have similar energy characteristics: ionisation potentials, heat of formation, activation energies, and mass spectra of fragments formed by dissociation of molecular ions. Enantiomers differ only in vector characteristics, which determine the properties of a molecule depending on its structure. Notably, α-amino acids contain an asymmetric carbon atom (C_α-atom) and can exist as optical isomers. The carboxyl group can rotate, and the hydrogen atom can be oriented both towards nitrogen and in the opposite direction. Conformational variability of molecules contributes to the reorientation of flexible carboxyl (-COOH) and amino (-NH_2) groups (Fig. 1b), forming various intramolecular hydrogen bonds. For example, the bond of a lone pair of a nitrogen atom with a hydrogen of a hydroxyl group (N...HO) or a bond between a hydrogen atom of an amino group and a carbonyl oxygen atom (NH...O= B) and hydroxyl (NH...OH) in groups.

Figure 2 demonstrates the mass spectrum of valine with ionising electron energies Ue=70 eV and a molecular source temperature of 393 K, as can be seen, the highest intensity corresponds to ions with m/z = 28, 42, 56 and 72 Da. Next, in the mass spectrum, the peak corresponding to the mother ion (m/z=117) is practically absent, which is inherent in aliphatic amino acids with low stability of the molecular ion formed during ionisation [12]. Inherent in most α-amino acids is that the main dissociation channel upon electron impact is conditioned upon the breaking of the C-Cα bond, and therefore, in the case of valine, an ion with a mass of m/z=72 is formed as a result of the cleavage of the COOH carboxyl group.

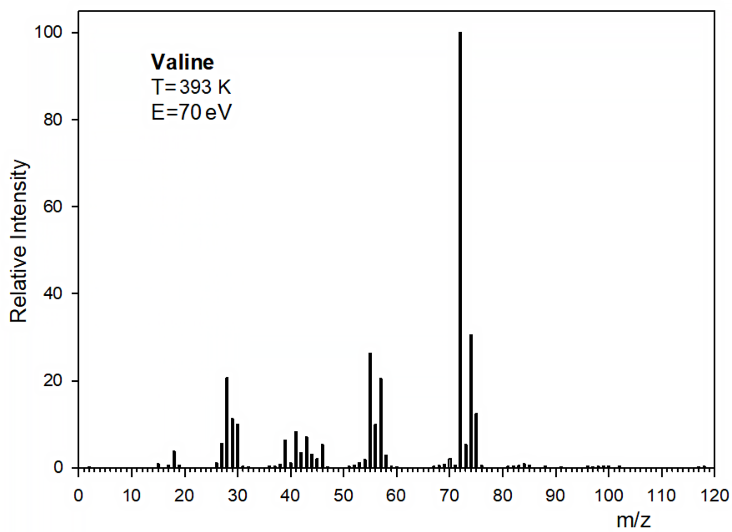

Figure 2. Mass spectrum of the valine molecule

Source: [2]

To analyse the mass spectra obtained by the authors, it was interesting to compare the relative intensities of the mass peaks of the valine molecule from various sources. This comparison is demonstrated in Table 1 from the NIST [13], SDBS [14] databases and studies [15; 16; 29].

Table 1. Comparison of relative intensities of valine peak masses

m/z	NIST [13]		SDBS [14]				V.Vukstich et al. [29]	P. Papp et al. [15]	W. Jochims, et al. [16]	OUR DATA
	DL-	D-	DL-	L-	DL-Nor	D-				
2			0.1	0.15						0.12
14	0.2		0.2	0.14	0.1	0.1				0.14
15	0.7		0.7	0.9	1.1	1.2				0.92
16				0.1				0.11		0.12
17	0.6		0.6	0.61	0.2	0.5				0.61
18	2.6		2.6	3.76	3.7	3.2		1.64		3.74
19	0.5		0.5	0.5	0.3	0.6		0.26		0.5
26	0.7	1.31	0.7	1.09	0.8	0.7		0.27		1.09
27	6.7	11.3	6.7	5.5	6.1	7.4	18.7	6.79	6	5.5
28	19.6	18.2	19.6	20.61	14.9	24.7	63.0	12.54	36	20.61
29	10.8	10.1	10.8	11.31	5.3	14.2	30.0	10.01	36	11.31
30	8.1	12.6	8.1	9.9	10.5	10.5	24.5	6.43	19	9.92
31	0.2	0.5	0.2	0.3	0.7	0.2		0.63		0.33
32	0.1		0.1	0.2	0.2	0.3		0.21		0.23
33	0.1		0.1	0.1	0.1					0.11
34				0.1		0.1				
36				0.4		0.4				0.43
37	0.2	0.5	0.2	0.25	0.2					0.25
38	0.8	1.2	0.8	0.71	0.6	0.5	17.7	0.71		0.71
39	6.7	8	6.7	6.35	3.5	7.2		4.69	3	6.35
40	0.7	3.3	0.7	1.05	0.6	0.9		0.74		1.05
41	8.4	12.6	8.4	8.21	3.7	8.7	13.5	6.43	9	8.21
42	2.8	5.9	2.8	3.49	4.9	3.1	6.8	2.54		3.49
43	7.2	10.5	7.2	7.04	4.7	6.7	8.3	4.98	13	7.03
44	1.2	7.7	1.2	2.97	7.8	1.6	5.2	2.43		2.97
45	1.5	5.1	1.5	2.1	1.6	2.1	9.4	1.38	6	2.1
46	5.4	5.1	5.4	5.3	3.1	6.4	13.5	3.6	13	5.3
47		0.2		0.2				0.22		0.2
49	0.1		0.1	0.1						0.1
50	0.1		0.1	0.14	0.2	0.2				0.14
51	0.4	0.5	0.4	0.36	0.2	0.4				0.36
52	0.6	0.7	0.6	0.52	0.2	0.6				0.52
53	1.1	1.5	1.1	1.1	0.6	1.2				1.1
54	2.1	2.5	2.1	1.84	0.8	1.9				1.84
55	28.7	24.9	28.7	26.33	6.1	31.4	33.9	28.91	64	26.33
56	9.8	12.2	9.8	9.86	3	12	21.9	5.46		9.86
57	19.1	26.7	19.1	20.48	3	24.5	30.7	26.08	60	20.48
58	3.2	3.9	3.2	2.9	0.1	3.3	6.2	1.96		2.9

Table 1, Continued

m/z	NIST [13]		SDBS [14]				V.Vukstich et al. [29]	P. Papp et al. [15]	W. Jochims, et al. [16]	OUR DATA
	DL-	D-	DL-	L-	DL-Nor	D-				
60	0.2	0.5	0.2	0.22		0.1				0.22
67	0.4	0.6	0.4	0.31		0.2				0.31
68	0.5	1	0.5	0.44	0.2	0.3				0.44
69	1	2.1	1	0.77	0.1	0.4				0.77
70	2.5	2.9	2.5	2.16	1.1	2.1		1.78		2.16
71	0.6	1	0.6	0.57	0.2	0.6				0.57
72	100	100	100	100	100	100	100	100	100	100
73	5.7	5.3	5.7	5.28	4.9	5		5.66		5.28
74	34.5	13.2	34.5	30.46	24	34	24	35.82	45	33.46
75	14	8.6	14	12.35	2.1	15.3	10.4	13.67	12	12.35
76	0.6	0.5	0.6	0.43	0.1			0.42		0.43
77				0.13		0.1				0.13
78	0.1		0.1	0.12		0.1				0.12
79	0.1		0.1	0.14						0.14
81	0.4		0.4	0.28		0.1				0.28
82	0.5	0.8	0.5	0.41	0.1	0.3		0.37		0.41
83	0.5	1	0.5	0.44		0.2				0.44
84	1	1	1	0.96		0.8				0.96
85	0.4	1.5	0.4	0.54		0.3		1.11		0.54
88		0.5		0.43	0.3					0.43
91	0.2		0.2	0.23						0.23
92	0.1		0.1	0.11						0.11
93	0.1		0.1	0.13						0.13
95	0.1		0.1	0.12						0.12
96	0.3		0.3	0.34						0.34
97	0.3		0.3	0.22		0.1				0.22
98	0.2	0.6	0.2	0.27		0.3				0.27
99	0.2	1	0.2	0.28						0.28
100	0.2	1.8	0.2	0.42		0.1				0.42
102	0.2	0.3	0.2	0.28		0.3				0.28
117		0.2		0.25					1	0.12
118		0.3		0.33						0.22

The results of studying the mass spectra of enantiomers of the L-, DL-, and D- forms of the valine molecule, obtained in various laboratories, presented in the table, give the most complete picture of the processes of formation of ion fragments. Comparison of the relative intensities demonstrated in the table shows a satisfactory agreement, but for some there are differences: not all ions with masses m/z=2, 16, 34, 36 are detected; the relative intensities of ion formation of fragments of enantiomers of L-, DL-, and D-forms with masses m/z=28, 29, 57, 58 differ (see Table 1).

Enantiomers must have the same mass spectra of ion fragments formed during dissociation of molecular ions [17]. However, analysis of the available data on the mass spectra of fragments formed upon ionisation of amino acids by electron shock reveals substantial differences for a number of D- and L-amino acids [16-18]. These differences can obviously only be related to the different probability of formation of any fragments according to the structural formula of enantiomers.

Thus, the results presented in the table allow considering the mechanisms of formation of the most intense ion fragments upon dissociative ionisation by electron shock. As mentioned above, ionisation and electron removal lead to a weakening of the bonds in the molecular ion compared to the neutral molecule. In all optimal structures of the parent amino acid cations, the positive charge is mainly localised on the carbon atom of the carboxyl group, and the dissociation process occurs due to charge transfer to the carbon chain. This is confirmed by the relatively low intensity (see Table 1) in the mass spectrum of the COOH ion peak$^+$ (m/z=45). Analysing the data of the most intense ion fragments presented in the table, the processes leading to their formation can be suggested as follows:

m/z=72. The main most intense ion fragment occurs as a result of effective dissociation of the parent ion of the valine molecule upon CC bond break [2] with the formation of a neutral fragment of the COOH carboxyl group according to reaction (2):

$$C_5H_{11}NO_2 + e^- \rightarrow NH_2(CH_3)_2(CH)_2 + (COOH) + 2e^- \quad (2)$$

m/z=74. The ion with this mass has a peak with an intensity of 33% of the main one and is associated with the dissociation of the side chain and the formation of the C_3H_7 propyl (3):

$$C_5H_{11}NO_2 + e^- \rightarrow NH_2CHOCOOH + (CH_3)_2CH + 2e^- \quad (3)$$

m/z=57. The appearance of a rather intense (20% of the main) peak of such a mass is associated with dissociation of the amino group and the formation of neutral water and propylene C_3H_6 molecules (4):

$$C_5H_{11}NO_2 + e^- \rightarrow NHCHC(OH)^+ + H_20 + CH_3CHCH_2 + 2e^- \quad (4)$$

m/z= 39, 41, 43. These peaks belong to hydrocarbon ions and amino and carboxyl groups (5-7) are not involved in the formation of these fragments:

$$C_5H_{11}NO_2 + e^- \rightarrow CHCHCH^+ + C_2H_6N0 + H_2O + 2e^- \quad (5)$$

$$C_5H_{11}NO_2 + e^- \rightarrow CH_2CCH_3{}^+ + C_2H_5NO_2 + H + 2e^- \quad (6)$$

$$C_5H_{11}NO_2 + e^- \rightarrow (CH_3)_2CH^+ + NH_2CH_2 + CO_2 + 2e^- \quad (7)$$

m/z= 27, 28, 29, 30. Unambiguous interpretation of peaks in this group is complicated by the alternativeness of the occurrence of certain neutral fragments, which is manifested in different intensities of peak masses obtained by interaction with electrons and photons (Table 1). For example, the appearance of the peak m/z=28 may correspond to isobar CO^+ and CH_2N^+ ions according to the following reactions (8):

$$C_5H_{11}NO_2 + e^- \rightarrow CO^+ + NH_2CH(OH)CH(CH_3)_2 + 2e^- \quad (8)$$

or (9)

$$C_5H_{11}NO_2 + e^- \rightarrow NHCH^+ + COOH + CH_3CH_2CH_3 + 2e^- \quad (9)$$

Preference should be given to reaction (9), since the formation of this HC-NH fragment dominates the processes of dissociation of amino acid molecules [19].

Analysis of the interaction processes of an electron with the valine molecule under study suggests that the carboxyl – COOH group – is initially separated due to a simple break in the bond between C_1-C_2 atoms.

The consequence is the formation of the main peak of the most intense in the mass spectrum with m/z=72. Energetically remarkably close to the process of separation of the entire carboxyl group is the separation of two neutral fragments H and CO_2, which is energetically more beneficial than the separation of two neutral OH and CO fragments [20].

Notably, in the mass range m/z=2-20, the interpretation of the appearance of peaks in the mass spectrum is quite difficult due to probable alternative channels of dissociative ionisation. This is especially true for the peak with m/z=2, which was also found in [14] for L- and DL-form enantiomers (Table 1).

The comparison of the relative intensities of mass peaks made in Table 1 with the data in NIST [13], SDBS [14], as well as in [15; 16] generally indicates a satisfactory agreement between them, and the evaporation temperature of valine molecules is given only in [14], which may make adjustments to the values of mass peaks. However, a more thorough analysis of the available mass spectra of fragments formed during electron shock ionisation of amino acids reveals substantial differences for a number of D- and L-amino acids [14; 16; 17]. Therewith, there are noticeable differences in the mass spectra of ions-fragments of compounds used by the authors [29] to identify 2,3-diaminopropanic acid. A more complete analysis of processes using theoretical calculations of the energies, lengths, and bond orders of mother, daughter fragment ions, and neutral molecules should be the result of a separate study, similar to the one conducted in [16] for photoionisation processes.

Undoubtedly, the influence of the temperature of the molecules under study on the dissociative ionisation process is essential [21-23]. This is also evidenced by the study [24]. Fig. 3 demonstrates the temperature dependences for the most intense ions of NH fragments$_2$(CH3)$_2$(CH)$^+$ (m/z=72), $NH_2CHCOOH^+$ (m/z=74), $NHCHC(OH)^+$ (m/z=57), $(CH_3)_2CH^+$ (m/z=43), $CH_2CCH_3{}^+$ (m/z=41) and CH_3 (m/z=15). Three segments are observed in Figure 3: a segment with an almost linear increase in intensity, a segment with exponential growth, with saturation in the temperature range of 400-418 K and a sharp decline, the cause of which is the beginning of decomposition of the substances under study [2]. Features on the measured dependences – the change in the slope of the curves at some temperatures, apparently, should be attributed to the passage of the processes described above (2-9).

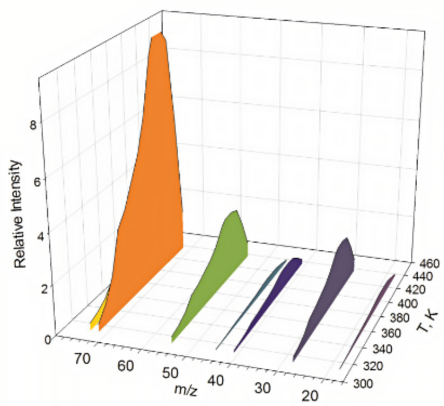

Figure 3. Dependence of the formation of positive ion fragments of the valine molecule on temperature. Electron energy 70 eV

Source: [2]

When the potentials on the deflecting electrodes of the mass spectrometer were turned off, the total (total) current of positive ions to the collector formed as a result of the interaction of the valine molecules under study with electrons was measured. By smoothly changing the energy of ionising electrons, it is possible to obtain the energy dependence of the total relative cross-section of the formation of positive ions in a given range of electron energies.

Figure 4 demonstrates the energy dependence of the total relative ionisation cross-section of the valine molecule in the energy range 5-60 eV, and also shows the threshold section of this dependence, which is approximated according to the least squares method [19; 22]. Evidently, the fitting results correlate well with the experimental curve, which allows determining the ionisation energies of the valine molecule, which turned out to be equal to: E_{IE}=8.66±0.22 eV.

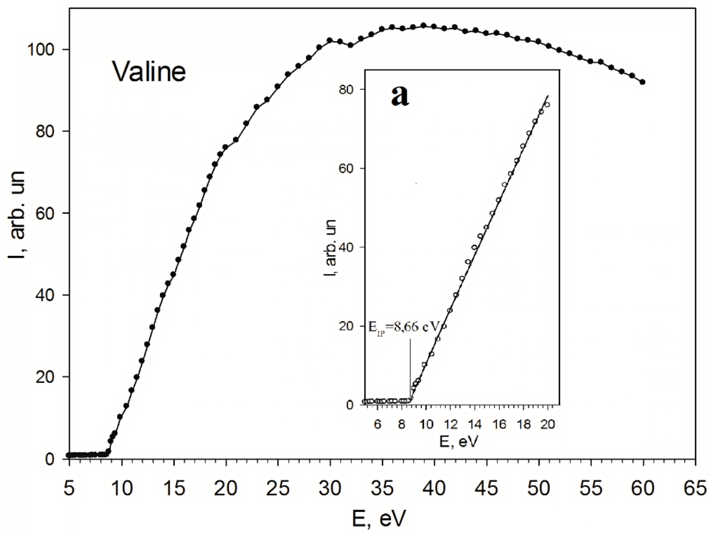

Figure 4. Energy dependence of the total ionisation cross-section of the valine molecule. On the tab: threshold section of the experiment point, solid approximation

The authors of this study compared it with the data of other authors [26-28] (see Table 2). In addition, the best agreement is observed with experimental data from the studies [15; 25] and with calculations according to the G3MP2 method [16].

Table 2. Value of the ionisation energy (eV) of the valine molecule

Experiment					Calculation		
Electronic shock				Photons	G3MP2	OVGF	OVGF
Our data	[25]	[26]	[15]	[16]	[16]	[27]	[28]
8.66± 0.20	8.71	9.86	8.91±0.05	8.9	8.89	9.54	9.50

Conclusions

Experimentally, the mass spectra of the valine molecule were investigated according to the mass spectrometry method in the range of mass numbers 0-120 Da within evaporation temperatures of the initial substance at 300-440 K. A detailed analysis of the processes of formation of ions-fragments of valine molecules by electron shock-was carried out. It was shown that the difference in the structural forms of valine enantiomers is reflected in the mass spectra as a redistribution of the relative intensity values of daughter ions. Information on the relative mass intensities of the L-, DL-, and D-form valine molecules obtained in various laboratories provides a more complete picture of the processes of ion fragment formation.

As a result of measurements of the total relative cross-section of the ionisation of the valine molecule by electrons in the energy range of 5-60 eV and the approximated threshold section of the energy dependence of the cross-section, the ionisation energy of the valine molecule was determined, which turned out to be equal to: $E_{IE}=8.66\pm0.22$ eV. This ionisation potential is compared with the available experimental and theoretical data, which showed a satisfactory agreement of the results obtained by the authors with the compared data. In conclusion, mass spectrometric studies of amino acids by electron shock in the gas phase provide rich information about their unique properties, allow determining the degree of fragmentation in the process of interaction with electrons, and evaluate the parameters of intermolecular bonds.

References

[1] Sonntag C. The chemical basis for radiation biology. London: Taylor & Francis press; 1987. 515 p.

[2] Ward JF. Advances in radiation biology. New York: Academic Press; 1977. Volume 5, Molecular Mechanisms of Radiation-Induced Damage to Nucleic Acids; p. 181-239.

[3] Golichenko BO, Naseka VM, Strelchuk VV, Kolomys OF. Raman study of L-Asparagine and L-Glutamine molecules adsorbed on aluminum films in a wide frequency range. *Semiconductor Physics, Quantum Electronics & Optoelectronics*. 2017;20(3):297-304. doi: 10.15407/spqeo203.297.

[4] Bulhakova AI, Zavilopulo AM. Mass spectrometric studies of the glutamine molecule. *Scientific Herald of Uzhhorod University. Series "Physics"*. 2018;(44):141-47. doi: 10.24144/2415-8038.2018.44.141-147.

[5] Inokuti M. Atomic and molecular data needed for radiotherapy and radiation research TECDOC-79. Vienna: IAEA Press; 1995. 754 p.

[6] Sanche L. (2006). Interaction of low energy electrons with DNA: Applications to cancer radiation therapy. *Radiation Physics and Chemistry*. 2006;(128):36-43. doi: 10.1016/j.radphyschem.2016.05.008.

[7] Erdevdi NM, Bulhakova AI, Shpenik, OB, Zavilopulo AN. (2020). Electron-impact-induced excitation of glutamine molecules. *Technical Physics Letters*. 2020;(46):815-18. doi: 10.1134/S1063785020080209.

[8] Monteiro WA. Radiation effects in materials. London: IntechOpen; 2016. 462 p.

[9] Fabrikant II, Eden S, Mason NJ, Fedor J. Chapter nine – recent progress in dissociative electron attachment: From diatomics to biomolecules. *Advances in Atomic, Molecular, and Optical Physics*. 2017;(66):546-641. doi: 10.1016/bs.aamop.2017.02.002.

[10] Hu Y, Bernstein ER. Vibrational and photoionization spectroscopy of biomolecules: Aliphatic amino acid structures. *Journal of Chemical Physics*. 2008;(128):164311. doi: 10.1063/1.2902980.

[11] Zavilopulo AN, Mironets EA, Agafonova AS. (2012). An upgraded ion source for a mass spectrometer. *Instruments and Experimental Techniques*. 2012;(55):65-71. doi: 10.1134/S0020441211060315.

[12] Zavilopulo AN, Shpenik OB. Electron-impact mass spectrometry of PTCDA molecules in the gas phase. *Ukrainian Journal of Physics*. 2019;64(1):3. doi: 10.15407/ujpe64.1.3.

[13] NIST standard reference database [Internet]. National Institute of Standards and Technology USA; n.d. [updated 2022; cited 2022 June 23]. Available from: http:// www.webbook.nist.gov.

[14] Spectral Database for Organic Compounds SDBS [Internet]. National Institute of Advanced Industrial Science and Technology. Japan; n.d. [updated 2022 March 31; cited 2022 June 23]. Available from: https: // sdbs.db.aist.go.jp.

[15] Papp P, Shchukin P, Kocisek J, Matejcik SJ. (2012). Electron ionization and dissociation of aliphatic amino acids. *The Journal of Chemical Physics*. 1012;(37):105101. https://doi.org/10.1063/1.4749244.

[16] Jochims, H-W, Schwell M, Chotin J-L, Clemino M, Dulieu F, Baumgärtel H, et al. (2004). Photoion mass spectrometry of five amino acids in the 6-22 eV photon energy range. *Chemical Physics*. 2004;298(1-3):279-97. doi: 10.1016/j.chemphys.2003.11.035.

[17] Smirnov OV, Basalaev AA, Boitsov VM, Vyaz'min SYu, Orbeli AL, Dubina MV. (2014). Fragmentation of D- and L-enantiomers of amino acids through interaction with 3He2+ ions. *Technical Physics*. 2014;(59):1698-704. doi: 10.1134/S1063784214110231.

[18] Meierhenrich U. Amino acids and the asymmetry of life. Berlin: Springer-Verlag; 2008. 264 p.

[19] Zavilopulo AN, Shpenik OB, Mylymko AN, Shpenik VYu. Mass spectrometry of d-ribose molecules. *International Journal of Mass Spectrometry*. 2019;(441):1-7. doi: 10.1016/j.ijms.2019.03.008.

[20] Song X, Li J, Hou H, Wang B. *Ab initio* study of the potential energy surface for the $OH+CO\rightarrow H+CO_2$ reaction. *Journal of Chemical Physics*. 2006;(125):094301. doi: 10.1063/1.2347711.

[21] Nuevo M, Meierhenrich UJ, Munoz Caro GM, Dartois E, d'Hendecourt L, Deboffle D, et al. The effects of circularly polarized light on amino acid enantiomers produced by the UV irradiation of interstellar ice analogs. *Astronomy & Astrophysics*. 2006;(457):741-51. doi: 10.1051/0004-6361:20042018.

[22] Ostroverkh A, Zavilopulo A, Shpenik O. Ionization of guanine, adenine and thymine molecules by electron impact. *The European Physical Journal D.* 2019;(73):38. doi: 10.1140/epjd/e2019-90532-3.

[23] Choi MY, Miller RE. Four tautomers of isolated guanine from infrared laser spectroscopy in Helium nanodroplets. *Journal of the American Chemical Society*. 2006;128(22):7320-8. doi: 10.1021/ja060741l.

[24] Zavilopulo AN, Shpenik OB, Markush PP, Kontrosh EE. Ionization of glycerin molecule by electron impact. *Technical Physics.* 2015;(60):957-63. doi: 10.1134/S1063784215070282.

[25] Klasinc L. Application of photoelectron spectroscopy to biologically active molecules and their constituent parts: III. Amino acids. *Journal of Electron Spectroscopy and Related Phenomena*. 1976;(8):161-4. doi: 10.1016/0368-2048(76)80018-7.

[26] Berry RS, Leach S. Elementary attachment and detachment processes. II. *Adv. Electron. Electron Phys.* 1981;(57):1.

[27] Close DM. (2011). Calculated vertical ionization energies of the common α-amino acids in the gas phase and in solution. *Journal of Physical Chemistry A.* 2011;115(13):2900-12. doi: 10.1021/jp200503z.

[28] Dehareng D, Dive G. (2004). Vertical ionization energies of α-l-amino acids as a function of their conformation: An Ab initio study. *International Journal of Molecular Sciences*. 2004;5(11):301-32. doi: 10.3390/i5110301.

[29] Vukstich VS, Romanova LG, Megela IG, Papp AV, Snegurskii AV. Fragmentation of a valine molecule by electron impact. *Technical Physics Letters*. 2017;(43):416-20.

Мас-спектрометричні дослідження молекул валіну електронним ударом в газовій фазі

Алла Ігорівна Булгакова

Інститут електронної фізики НАН України
88017, вул. Університетська, 21, м. Ужгород, Україна

Анотація

Актуальність. Валін є однією з восьми амінокислот несинтезованих людським організмом, необхідною для синтезу і росту тканин тіла, м›язової координації; регулювання нервових процесів, азотного обміну, стабілізації гормонального фону. Оскільки α-амінокислоти містять асиметричний атом вуглецю, то вони можуть існувати у вигляді оптичних ізомерів (дзеркальних антиподів), які відіграють важливу роль в процесах біосинтезу білка. Структуру речовини та фізичні процеси, які відбуваються в ній досліджують за допомогою методу мас-спектрометрії і спектрального аналізу. Що свідчить про актуальність задачі, яка досліджувалася у цій роботі.

Мета. Мас-спектрометричні дослідження утворення іонних продуктів однократної та дисоціативної іонізації молекули валіну ($C_5H_{11}NO_{2)}$ електронами методом пучків, що перетинаються в діапазоні енергій бомбардуючих електронів 6–70 eV. Розглянути механізми утворення найінтенсивніших іонів-фрагментів при дисоціативній іонізації електронним ударом.

Методи. Експеримент проводився на установці з монопольним мас-спектрометром типу МХ-7304А, який відноситься до класу динамічних аналізаторів мас з іонізацією електронним ударом у діапазоні масових чисел 0–120 Da. Мас-спектри молекул досліджено за різних температур джерела молекул в діапазоні 300–600 K.

Результати. Проведено порівняння отриманих результатів з мас-спектрами D-, L- та DL-енантіомерних форм молекули валіну з даними баз NIST та SDBS. Детально проаналізовано особливості процесів утворення іонів-фрагментів молекул валіну електронним ударом, а також досліджено динаміку виходу іонів-фрагментів в інтервалі температур випаровування вихідної речовини 300–440 K. Було проведено вимірювання повного відносного перерізу іонізації досліджуваної молекули мас-спектрометричним методом з енергією іонізуючих електронів 5–60 eV. За результатами експериментальних досліджень визначено та наведено в даній роботі порогову ділянку залежності повного відносного перерізу іонізації валіну.

Висновки. Детальний аналіз процесів утворення іонів-фрагментів у мас-спектрах дозволяє показати вплив структурних форм енантіомерів валіну на перерозподіл відносних інтенсивностей іонів-продуктів.

Ключові слова: електрон, мас-спектрометрія, іонізація, амінокислота

Scientific Herald of Uzhhorod University
Series "Physics"

Journal homepage: https://physics.uz.ua/en

Issue 51, 18-23

Received: 31.03.2022. Revised: 16.05.2022. Accepted: 03.06.2022

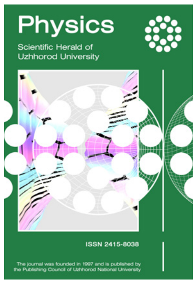

UDC 539.172.2
PACS 25.20.DC
DOI: 10.54919/2415-8038.2022.51.18-23

Study of the Cross-Section for the ^{122}Te(γ, n)^{121}Te Reaction by the Activation Method

Zoya Bigan, Petro Derechkey, Volodymyr Mazur, Oksana Pop*

Institute of Electron Physics of the NAS of Ukraine
88017, 21 Universytetska Str., Uzhhorod, Ukraine

Abstract

Relevance. The study of photonuclear reactions plays a defining role in the formation of modern ideas about high-localized collective excitations in nuclei of the giant resonance type. The giant dipole E1-resonance (GR) is the main feature in γ-quantum absorption cross-sections of nuclei. The presence of isotopes with multiple isotopes makes it possible to trace the evolution of GR characteristics from changes in the number of neutrons in the nuclei. One such element is tellurium.

Purpose. The purpose of this research is an experimental and theoretical study of the cross-section of ^{22}Te(γ, n)^{121}Te reaction in the region of giant E1-resonance energies.

Methods. The study of the cross-section of (γ, n) reaction on ^{122}Te isotope was performed on the bremsstrahlung γ-beam of the M-30 microtron of the Institute of Electronic Physics of the National Academy of Sciences of Ukraine. The yield curves were measured in the range of maximum gamma-quantum energies E_{max}=10-18 MeV. The reaction cross-section was calculated by the inverse matrix method. When registering the reaction products, an activation technique was used, while the gamma activity of the products was recorded by the spectrometric method. The theoretical calculations of the cross-section for the ^{122}Te(γ, n)^{121}Te reaction were performed using the TALYS-1.9 software package.

Results. The measured experimental yield ratios of the ^{122}Te(γ, n)^{121}Te and ^{130}Te(γ, n)^{129}Te $d = Y_n^{121} / Y_n^{129} = f(E_{max})$ reactions allowed the experimental cross-section for the ^{122}Te(γ, n)^{121}Te reaction to be calculated. The cross-section has a single hump shape with a maximum at an energy of ~ 15.3 MeV. It was approximated by the Lorentz curve with the parameters δ_0=(274.1±2.1) MB, E_0 (15.27±0.10) MeV, Γ_0=(4.76±0.08) MeV. The cross-section obtained was compared with similar cross-sections for ^{126}Te and ^{130}Te isotopes, as well as with theoretical calculations according to the TALYS-1.9 program.

Conclusions. The obtained cross-section for the ^{122}Te(γ, n)^{121}Te reaction is consistent with the evolution of the parameters of (γ, n) reaction cross-section on tellurium isotopes ^{130}Te(γ, n)^{129}Te with a change in the number of neutrons. The theoretical approaches used are satisfactorily consistent with the experimental data. This agreement indicates the main contribution of the statistical mechanism to the cross-section of the considered (γ, n) reaction and a relatively small contribution of semi-direct processes.

Keywords: microtron, bremsstrahlung gamma radiation, photonuclear reaction cross-section, ^{122}Te, gamma spectrometry

Suggested Citation:
Bigan Z, Derechkey P, Mazur V, Pop O. Study of the cross-section for the ^{122}Te(γ, n)^{121}Te reaction by the activation method. *Scientific Herald of Uzhhorod University. Series "Physics"*. 2022;(51):18-23.

*Corresponding author

Introduction

The main feature in the gamma-ray absorption cross-sections of atomic nuclei in the 10-20 MeV range is the giant E1 resonance (GR). The study of its characteristics has played an important role in the formation of modern understandings of nuclear collective perturbations. Therefore, an empirical study of the GR parameters was carried out as a direct measurement of the σ_{tot} cross-section both by the absorption method [1; 2] and by summing the cross-sections of the partial decay channels of the E1 resonance, i.e. by summing the (γ, n), (γ, 2n), (γ, 3N), etc. reaction cross-sections [3]. Recently, the focus of research on giant dipole resonance has largely shifted from the study of its gross characteristics and taxonomics to the study of partial channels of GR decay with fixation of specific isolated, isomeric states of daughter nuclei [4].

The growing interest in the study of photonuclear reactions in the region of 10-20 MeV, which is observed today, can be associated with several reasons, in particular, both with the need to obtain missing information about the cross-sections of photonuclear reactions, for example, for astrophysical calculations, for which there is a need [5], and with the creation of fundamentally new intensive sources of quasi-monochromatic gamma radiation [6; 7].

To date, cross-section for the ^{122}Te(γ, n)^{121} reaction has not been explored. A detailed study of the evolution of giant resonance characteristics from changes in nuclear mass for $^{124-130}$Te heavy isotopes was carried out in the work [8]. The work was performed on a beam of quasi-monochromatic photons from positron annihilation on the fly. The measurement was performed in the range of gamma-ray quantum energies of 8-26 MeV. By registering neutrons, was determined the complete cross-section of photoneutron reaction s At the same time, the possibility of 1n, 2n, and 3n neutrons escape was determined experimentally.

Natural tellurium samples are known to contain very few light isotopes ^{120}Te, ^{122}Te: ^{120}Te (0.09%), ^{122}Te (2.4%). That is why, until recently, photoneutron cross-sections on them have not been studied. Such studies began to be conducted only with the advent of highly enriched targets of light tellurium isotopes [8]. However, getting such targets is very difficult and expensive.

The purpose of this paper is to study the cross-section for the ^{122}Te(γ, n)^{121}Te reaction in the energy range 10-18 MeV, as well as to compare the results with theoretical calculations.

Materials and Methods

This study presents the results of studying targets in the form of disks of high-purity vitreous tellurium oxide TeO, with a diameter of 25 mm and a thickness of 2 mm. Natural tellurium was used. Despite the insignificant content of ^{122}Te in the studied samples, the present activity of ^{121}Te was accurately recorded and identified. Measurement of the ^{122}Te(γ,n)^{121}Te reaction yields was performed using the activation technique. Gamma radiation from the decay of reaction products (γ, n) was recorded.

Irradiation of the studied samples was carried out in the Department of Photonuclear Processes Institute of Electron Physics of the National Academy of Sciences of Ukraine on a braking gamma beam of the M-30 microtron, the parameters of which are given in [9]. The average current was 5 μa, monitoring was performed every 1.2 seconds and was recorded. The energy of accelerated electrons was changed by changing the number of orbits of the electron beam (within a wide range) and changing the magnitude of the conducting magnetic field strength (within one number of orbits). The value of the conducting magnetic field strength was controlled by the method of nuclear magnetic resonance. The irradiation was performed in the maximum energy range of the bremsstrahlung gamma-ray beam 10-18 MeV in increments of ΔE=0.5 MeV.

The irradiation time t_{irr} it was 20 minutes at high energies and 2 hours near the threshold (γ, n) reactions, irradiation time, and measurements were selected from the optimal conditions for recording gamma lines from the decay of daughter nuclei. The error of recording equipment was less than 5%. Measurements of the reduced gamma activity of the studied targets were performed on a 175 cm^3 HPGe detector (2 keV resolution for a 1332 keV ^{60}Co line). A typical instrumental gamma spectrum is shown in Figure 1.

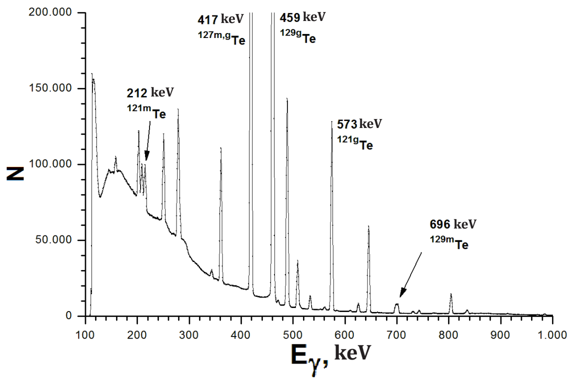

Figure 1. Instrumental gamma spectrum of an irradiated TeO_2 target

Results and Discussion

Along with the measurement of gamma lines from the decay of ^{121}Te obtained in $^{122}Te(\gamma, n)^{121m,g}Te$ reaction gamma lines were measured from ^{129}Te decay obtained in $^{130}Te(\gamma, n)^{129m,g}Te$ reaction, that were used to calibrate $^{122}Te(\gamma, n)^{121}Te$ reaction yield. The cross-sections for the $^{130}Te(\gamma, n)^{129}Te$ reaction were taken from [8]. Basic spectroscopic parameters from the decay of both the main and isomeric states of isotopes ^{121}Te and ^{129}Te is shown in Table 1 [10-13].

Table 1. Main spectroscopic parameters

No.	Isotope	B_n	J^π	E_{iso} (KeV)	E (KeV)	$T_{1/2}$	α (%)
1	^{121m}Te		$11/2^-$	294	212	154 days	81.4
2	^{121g}Te	9.834	$1/2^+$		573	19.16 hours	80.3%
3	^{129m}Te		$11/2^-$	105	696	33.6 days	2.6
4	^{129g}Te	8.419	$3/2^+$		456	69.6 min	7.7

The table shows the following values: B_n – thresholds of (γ, n) reactions, J^π – spin parity, E_{iso} – energy of the isomeric level, E_γ – energy of the analytical gamma line, $T_{1/2}$ – half-life, α – intensity. Experimentally obtained ratios of the ground state excitation yield of isotope ^{121}Te (Y_{g1}) to the ground state excitation yield of isotope ^{129}Te (Y_{g2}):

$$\eta_1 = Y_{g1}/Y_{g2} = c_{12} \cdot b_{12}(\lambda_1 \cdot \varphi_2 \cdot f_2/\lambda_2 \cdot \varphi_1 \cdot f_1) \cdot (N_1/N_2) \quad (1)$$

where c_{12} – coefficient that takes into account miscalculations and pulse overlays, b_{12} – the ratio of the content of the corresponding isotopes in the target ($b_{12}=b_2/b_1$), λ – decay coefficient, $\phi_{12}=\xi k\alpha$, where ξ – photoefficiency of analytical gamma-ray line registration during the decay of ground states, k – coefficient of self-absorption of these lines in the material of the target under study, α – the intensity of analytical gamma lines, f – time function: $f(t)=[1-exp(t_{itr})]\cdot exp(t_{cool})[1-exp(t_{meas})]\cdot(t_{itr}, t_{cool}, t_{meas}$ *–times of irradiation,cooling and measurement)*, N – the number of pulses under photo peak of analytical gamma lines.

Both ^{121}Te and ^{129}Te tellurium isotopes have isomeric states and thus in the reaction (γ, n) both their ground states and isomeric states are populated. At the same time, the total yield (γ, n) of the Y_n reactions, related to the excitation yields of the ground Y_g and the isomeric state Y_m is as follows:

$$Y_n = Y_g + Y_m = Y_g(1 + Y_m/Y_g) = Y_g(1 + d) \quad (2)$$

Experimentally obtained isomeric ratio of d yields for ^{121}Te and ^{129}Te isotopes is described in [14]. Studying the ratio of population yields in (γ, n) reactions of the ground states of tellurium isotopes can be determined by Y_n^{121}/Y_n^{129} – ratio of the total reaction yield (γ, n) on ^{122}Te isotope until the complete $^{130}Te(\gamma, n)^{129}Te$ reaction yield, (Fig. 2). The root-mean-square error is less than 1% and does not exceed the point size.

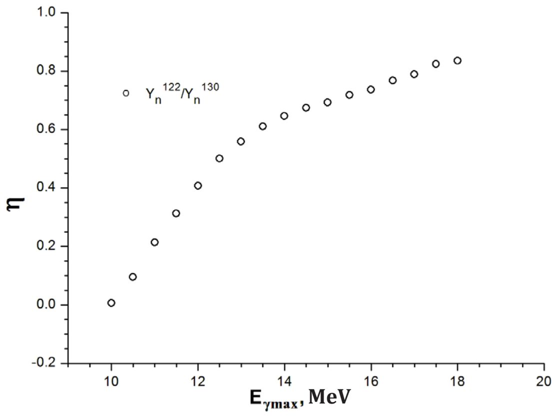

Figure 2. Dependence of the Y_n^{122}/Y_n^{130} yield ratio on the maximum energies of the braking beam spectrum

Using the cross-section for $^{130}Te(\gamma, n)^{129}Te$ reaction in [8] and the resulting experimental dependence $\eta=Y_n^{121}/Y_n^{129}$ from the energy of the inhibitory gamma spectrum, the cross-section for the $^{122}Te(\gamma, n)^{121}Te$ reaction can be calculated. The calculation was performed by the inverse matrix method [15] in increments of 1 MeV. The resulting reaction cross-section (γ, n) is shown in Figure 3.

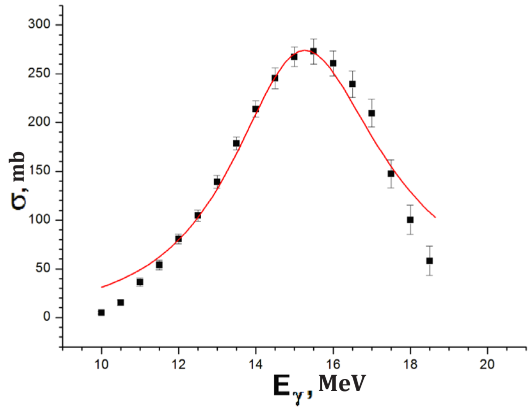

Figure 3. ^{122}Te(γ, n)^{121}Te reaction cross-section

As can be seen from Figure 3, the resulting cross-section has a single-humped shape with a maxim at an energy of ~15.3 MeV, the result of approximation of the cross-section by the Lorentz curve is shown as a solid curve:

$$\sigma(E) = \sigma_0 E^2 \Gamma_0^2 [(E^2 - E_0^2) + E^2 \Gamma_0^2] \qquad (3)$$

Here σ_0, E_0, G_0 are parameters. The approximation was carried out using the least squares method. The following parameter values are obtained: σ_0=(274.1±2.1) mb, E_0=(15.27±0.10) MeV, G_0=(4.76±0.08) MeV.

Figure 4 shows a comparison of the cross-sections for the ^{122}Te(γ, n)^{121}Te reaction with cross-sections for (γ, n) reactions on ^{126}Te and ^{130}Te heavier tellurium isotopes [8]. The evolution of cross-sections from light to heavy isotopes is observed. General trends can be noted: shift of the ^{122}Te cross-section threshold in the direction of higher energies and some growth of the ^{126}Te and ^{130}Te cross-sections is most likely due to an increase in the mass of these isotopes.

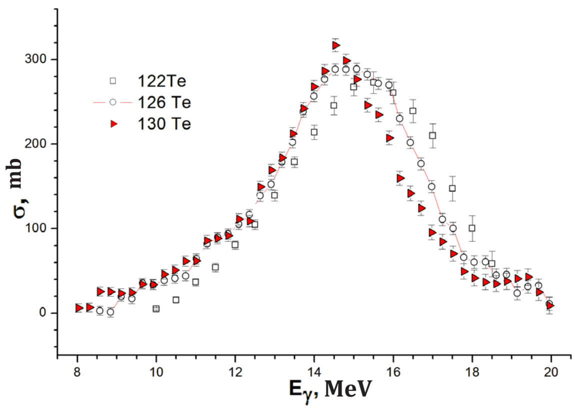

Figure 4. Comparison of (γ, n) reaction cross-sections on ^{122}Te, ^{126}Te, ^{130}Te isotopes

In order to compare the obtained experimental cross-sections with theoretical estimates, calculations of the cross-sections for the ^{122}Te(γ, n)^{121}Te reaction are performed using the TALYS-1.9 software package [16]. For theoretical evaluation, the following scheme is used: a target core with the following characteristics (Z_i, N_i) and spin parity (J_i, π_i) absorbs a dipole gamma quantum with E_γ energy and forms a compound nucleus with excitation energy E_c (E_c= E_γ) and the spectrum of possible spin and parity values (J_c, π_c). The total absorptions section σ_{tot} is calculated using the parameterized characteristics of the giant E1 resonance. The decay of the excited nucleus occurs in accordance with the Hauser-Feshbach statistical mechanism [17]. Additionally, the impurity of semi-direct processes is considered, which was a fraction of a percent at the energy E_γ=12 MeV and 8% at energy E_γ=18 Mev. Neutron emission at specific levels (zones) of the daughter nucleus was calculated using T_l permeability coefficients, which were based on the optical model. At the same time, specific discrete levels from the RIPL-3 base were taken to the excitation energy of the daughter nuclei E=3 MeV [18]. At higher excitation energies, the spectrum was considered continuous, described by the density of levels ρ(E, J, π) and was divided into a certain number of energy bands. In this case – 50. The effective permeability coefficient T^{ef}_l was determined for each band.

The density of ρ levels was described in two approaches: the constant temperature model and the energy-shifted Fermi-gas model [16; 19]. Results of calculating the cross-section for the ^{122}Te(γ, n)^{121}Te reaction and their comparison with the experiment are shown in Figure 5. Light circles indicate the result of calculations using the constant temperature model, triangles – the energy-shifted Fermi-gas model, dark dots – the experimental results.

The figure shows that both theoretical approaches used give very similar results and are in satisfactory agreement with the experimental data. This agreement indicates the main contribution of the statistical mechanism to the cross-section of the considered (γ, n) reactions and, accordingly, a relatively small contribution of semi-direct processes.

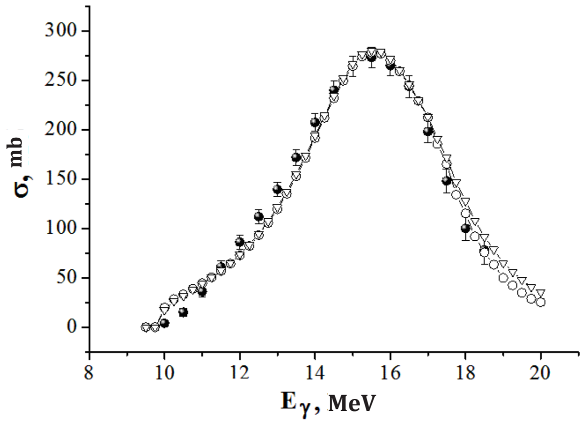

Figure 5. Comparison of (γ, n) reaction cross-sections on ^{122}Te, ^{126}Te, ^{130}Te isotopes

Conclusions

The presented experimental studies of the $^{122}Te(\gamma, n)^{121}Te$ reaction were carried out on the bremsstrahlung gamma-ray beam of the M-30 microtron of the Institute of Electronic Physics of the National Academy of Sciences of Ukraine in the maximum energy range of the bremsstrahlung spectrum $E_{\gamma max}$=10-18 MeV. The activation method was used in the measurements.

As a result of the measurements performed, the ratio of the $^{122}Te(\gamma, n)^{121}Te$ total reaction yield to $^{130}Te(\gamma, n)^{129}Te$ total reaction yield was determined, which allowed, using the cross-section for the $^{130}Te(\gamma,n)^{129}Te$ reaction [8], calculate both the absolute yield and the cross-section for the $^{122}Te(\gamma,n)^{121}Te$ reaction. Theoretical calculations of the (γ, n) reaction cross-section for ^{122}Te isotope have been performed. Calculations were performed using the TALYS-1.9 software package. In the process of comparing theoretical and experimental results, their satisfactory agreement was obtained.

References

[1] Gurevich GM, Lasareva LE, Mazur VM, Solodukhov GV, Tulupov BA. Giant resonance in the total photoabsorption cross-section of Z≈90 nuclei. *Nucl. Phys. A*. 1976;273(2):326-40.

[2] Gurevich GM, Lasareva LE, Mazur VM, Merkulov SYu, Solodukhov GV, Tyutin VA. Total nuclear photoabsorption cross-sections in the region 150<A<190. *Nucl. Phys. A*. 1981;351(2):257-65.

[3] Varlamov AV, Varlamov VV, Rudenko DS, Stepanov ME. Atlas of giant dipole resonances. Moscow: Lomonosov Moscow State University; 1999. 321 p.

[4] Mazur VM. [Excitation of isomeric states of nuclei in photoneutron reactions in the region of giant dipole resonance]. *PEPAN*. 2000;31(2):385-430. Russian.

[5] Nair C, Junghans AR, Erhard M, Bemmerer D, Beyer R, Grosse E, et al. Dipole strength in ^{144}Sm studied via (γ, n), (γ, p) and (γ, α) reactions. *Phys. Rev. C*. 2010;81(5):article number 055806.

[6] Weller HR, Ahmed MW. The HIγS facility: A free-electron laser generated gamma–ray beam for research in nuclear physics. *Mod. Phys. Lett. A*. 2003;18(23):1569-90.

[7] Horikawa K, Miyamoto S, Amano S, Mochizuki T. Measurement for the energy and flux of laser Compton scattering γ-ray photons generated in an electron storage ring. *Nucl. Instrum. Methods Phys. Res. A: Accel. Spectrom. Detect. Assoc. Equip.* 2010;618(1):209-15.

[8] Lepretre A, Beil H, Bergere R, Carlos P, Fagot J, De Miniac A, et al. A study of the giant dipole resonance in doubly even tellurium and cerium isotopes. *Nucl. Phys. A*. 1976;258(2):350-64.

[9] Kapica SP, Melekhin VN. The microtron. London: Harwood Academic; 1978. 204 p.

[10] Firestone RB. Table of isotopes. 8th ed. New York: J. Wiley and Sons; 1999. 224 p.

[11] Symochko D, Browne E, Tuli JK. Adopted levels gammas for ^{119}Te. *Nucl. Data Sheets*. 2009;(110):2945-51.

[12] Ohya S. Adopted levels gammas for ^{123}Te. *Nucl. Data Sheets*. 2004;(102):547-54.

[13] Tendow Y. Adopted levels gammas for ^{129}Te. *Nucl. Data Sheets*. 1996;(77):763-70.

[14] Mazur VM, Symochko DM, Bigan ZM, Poltorzhytska TV. Excitation of the $^{119}Te^{m}$, $^{121}Te^{m}$, $^{123}Te^{m}$, $^{127}Te^{m}$ and $^{129}Te^{m}$ isomer in (γ, n) reactions from 10 to 22 MeV. *Phys. Rev. C*. 2013;87(4):article number 044604.

[15] Bogdankevich OV, Nikolaev FA. Methods in bremsstrahlung research. New York: Academic Press; 1966. 217 p.

[16] Koning AJ, Hilaire S, Duijvestijn MC. TALYS-1.0: Comprehensive nuclear reaction modelling. *AIP Conference Proceedings*. 2005;769(1):1154-9.

[17] Hauserë W, Feshbach H. The inelastic scattering of neutrons. *Phys. Rev.* 1952;87(2):article number 336.
[18] Capote P, Herman M, Obloszinsky P, Young PG, Goriely S, Belgya T, et al. Reference input parameter library (RIPL-3). *Nucl. Data Sheets.* 2009;110(12):3107-3214.
[19] Dilg W, Schantl W, Vonach H, Uhl M. Level density parameters for the back-shifted fermi gas model in the mass range 40<A<250. *Nucl. Phys. A.* 1973;217(2): 269-98.

Вивчення перерізу реакції ^{122}Te(γ, n)^{121}Te активаційним методом

Зоя Михайлівна Біган, Петро Сергійович Деречкей,
Володимир Михайлович Мазур, Оксана Михайлівна Поп

Інститут електронної фізики НАН України
88017, вул. Університетська, 21, м. Ужгород, Україна

Анотація

Актуальність. Дослідження фотоядерних реакцій відіграє визначальну роль у формуванні сучасних уявлень про високорозташовані колективні збудження в ядрах типу гігантських резонансів. Гігантський дипольний Е1-резонанс (ГР) – головна особливість у перерізах поглинання γ-квантів ядрами. Наявність ізотопів із багаточисленими ізотопами дає змогу простежити еволюцію характеристик ГР від зміни числа нейтронів в ядрах. Одним з таких елементів являється телур

Мета. Метою роботи є експериментальне та теоретичне дослідження перерізу реакції ^{122}Te(γ, *n*)^{121}Te в області енергій гігантського Е1-резонансу.

Методи. Дослідження перерізу реакції (γ, *n*) на ізотопі ^{122}Te проводилося на гальмівному γ-пучку мікротрону М-30 Інституту електронної фізики НАН України. Криві виходу вимірювалися в інтервалі максимальних енергій гамма-квантів $E_{\gamma max}$=10–18 МеВ. Переріз реакції розраховувався методом оберненої матриці. У процесі реєстрації продуктів реакції використовувалася активаційна методика, водночас реєструвалася гамма-активність продуктів спектрометричним методом. Теоретичні розрахунки перерізу реакції ^{122}Te(γ, *n*)^{121}Te проводилися за допомогою програмного пакету TALYS-1.9.

Результати. Виміряні експериментальні відношення виходів реакцій ^{122}Te(γ, *n*)^{121}Te і ^{130}Te(γ, *n*)^{129}Te $d = Y_n^{121} / Y_n^{129} = f\,(E_{max})$ дали змогу розраховувати експериментальний переріз реакції ^{122}Te(γ, *n*)^{121}Te. Переріз має одногорбу форму з максимумом при енергії ~15,3 МеВ. Він апроксимувався кривою Лоренца з параметрами δ_0 = (274,1±2,1) мб, E_0 (15,27±0,10)МеВ, Γ_0=(4,76±0,08) МеВ. Проведено порівняння одержаного перерізу з аналогічними перерізами для ізотопів ^{126}Te і ^{130}Te, а також теоретичними розрахунками за програмою TALYS-1.9.

Висновки. Одержаний переріз реакції ^{122}Te(γ, *n*)^{121}Te узгоджується з еволюцією параметрів перерізів (γ, *n*) реакції на ізотопах телуру ^{130}Te(γ, *n*)^{129}Te зі зміною числа нейтронів. Використані теоретичні підходи задовільно узгоджуються з експериментальними даними. Таке узгодження свідчить про основний вклад статистичного механізму в переріз розглянутої (*γ*, *n*) реакції і порівняно малий вклад напівпрямих процесів

Ключові слова: мікротрон, гальмівне гамма-випромінювання, переріз фотоядерної реакції, ^{122}Te, гамма-спектрометрія

Scientific Herald of Uzhhorod University
Series “Physics”

Journal homepage: https://physics.uz.ua/en

Issue 51, 24-29

Received: 14.04.2022. Revised: 03.06.2022. Accepted: 17.06.2022

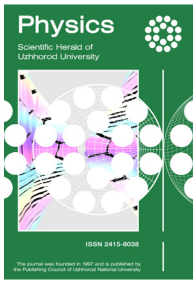

UDC 535.3
PACS 42.65.Wi, 42.70.Nq
DOI: 10.54919/2415-8038.2022.51.24-29

Nonlinear Surface Polaritons near the Interface between a Magneto-Optical Substance and a Nonlinear Metamaterial with a Permittivity Close to Zero

Andriy Groza[1], Nickolay Siddelev[2*]

[1]Open International University Human Development University “Ukraine”

54003, 22 2-nd Voyenna Str., Mykolaiv, Ukraine

[2]Petro Mohyla Black Sea National University

54003, 10 68 Desantnykiv Str., Mykolaiv, Ukraine

Abstract

Relevance. Considerable attention of researchers is drawn to nonlinear surface optical waves, as they are promising for application in optical information processing systems, ultra-sensitive sensors, and modern telecommunications components.

Purpose. To obtain an exact solution of the Maxwell equation system for TM-polarised nonlinear surface polaritons propagating along the interface between an optically linear magnetic medium and an optically nonlinear medium with saturated nonlinearity.

Methods. Analysis of the properties of nonlinear surface polaritons (NSP) and mathematical modelling of the dependence of the permittivity of a nonlinear medium on the intensity are used.

Results. TM-polarised nanoparticles propagating along the interface of a magneto-optical medium and a nonlinear optical metamaterial with a permittivity close to zero (ENZ-metamaterial) are studied. For NSP in such a structure, an exact solution of the Maxwell equation system is obtained, considering the saturation effect of optical nonlinearity. On this basis, the dependences of constant propagation on the total energy flux of NSP and energy fluxes in contact media in the structure were investigated: magneto-optical ENZ-metamaterial with negative permittivity/nonlinear self-focusing ENZ-metamaterial.

Conclusions. The NSP energy flow is positive in a nonlinear medium and negative in a linear one. As the saturation level decreases, the NSP energy fluxes in the contacting media increase modulo, if the value of the NSP propagation constant (NSPPC) is fixed. The lowest NSPPC value for guiding nonlinearity is obtained when the total energy flow of the NSP becomes zero. As the saturation level decreases, the NSP propagation variable (NSPPV) increases. At a fixed NSPPC, with a decrease in the magnetic permeability, the energy fluxes of NSP in the contacting media increase. When the magnetic permeability decreases to zero and the NSP energy flux is positive, the NSPPV change range narrows

Keywords: guiding nonlinearity, propagation constant, permittivity of a nonlinear medium, magneto-optical metamaterial, magnet, saturation

Suggested Citation:
Groza A, Siddelev N. Nonlinear surface polaritons near the interface between a magneto-optical substance and a nonlinear metamaterial with a permittivity close to zero. *Scientific Herald of Uzhhorod University. Series “Physics”*. 2022;(51):24-29.

*Corresponding author

Introduction

Nonlinear surface optical waves attract considerable attention of researchers due to the possibility of their application in modern telecommunications components, optical information processing systems and ultra-sensitive sensors.

The properties of such waves are determined by the dielectric and magnetic properties of the contacting media at the corresponding frequency. Studies of TM-polarised nonlinear surface polaritons (NSP) propagating along a single interface, as well as nonlinear waves in multilayer structures, which were conducted earlier [1-3], were limited by the values of parameters of natural materials at optical frequencies, e.g., the magnetic permeability of the medium was considered equal to one.

Metamaterials are artificially created composite media, and the proper formation of their nanostructure allows obtaining any desired values of material parameters [4-6]. This creates wide possibilities for controlling the properties of electromagnetic waves [7]. For example, surface polaritons can propagate along the surface of an ENZ-metamaterial with an extremely high phase velocity [8]; in metal-ferromagnetic structures, the wave vector of a surface polariton can be controlled using a weak external magnetic field [9]; metamaterials with both near-zero permittivity and magnetic permeability (epsilon-and-mu-near-zero (EMNZ)), which are also called zero-index materials (ZIM), allow adjusting the phase delay surface polaritons [10] and implement waveguides with exotic properties [11]. The use of materials in which the transition between phase-changed materials occurs under external influence [12-14] is of particular interest for creating switching components of integrated optical devices.

The resulting ENZ-metamaterial for the optical range [15] has a multilayer Ag/SiN structure. The real and imaginary parts of its permittivity are simultaneously close to zero in a wide spectral range. The ENZ-metamaterial for near-infrared radiation was manufactured as a multilayer Ag/Ge structure [16]. Magneto-optical metamaterials were created as AU-core-Co-shell structured arrays of metal microparticles [17], periodic arrays of Au/Ni bimetallic plasmon ring resonators [18], and Ni nanowire arrays embedded in an anodised aluminium oxide base [19]. Energy losses can be considerable in such metallic nanostructures, which encourages the development of fully dielectric magneto-optical metamaterials. The first fully dielectric NIZ-metamaterial for infrared frequencies has a structure comprising stackable silicon rods separated by layers of silicon oxide [20]. The first NIZ-metamaterial suitable for placement on an electronic chip for optical frequencies was manufactured as an array of silicon columns based on an insulator-silicon base [21]. Therefore, a monolithic CMOS NIZ-metamaterial comprising a square array of air holes in an insulator silicon wafer, which is more suitable for standard planar technological processes, was created [22].

Nonlinear ENZ-metamaterials are produced mainly as structures consisting of layers of metal and nonlinear matter located between them, or as a nonlinear medium doped with metal particles [23-25]. The effect of local field amplification in such structures [26] can lead to an increase in their nonlinearity [27]. For example, the nonlinear refractive index of a nonlinear multilayer ENZ-structure Ag/TO_2 is six orders of magnitude greater than the nonlinear refractive index of the voluminous TO_2 [23]. High local field values in such metamaterials can lead to saturation of their nonlinear permittivity. The effects caused by saturation of the nonlinear permittivity of metamaterials can be studied for NSP based on the exact solution of the Maxwell equation system for a nonlinear medium [1].

In this paper, the authors present an exact solution of the Maxwell equation system for TM-polarised NPCs propagating along the interface between an optically linear magnetic medium and an optically nonlinear medium with nonlinear saturation. Using the obtained solution, the authors investigated the dependence of the stable propagation of NSP on the total energy flux of NSP and energy fluxes in contacting media for the structure: magnetic ENZ-metamaterial/nonlinear self-focusing ENZ-metamaterial. The results for the case of saturating nonlinearity are compared with the case of guiding nonlinearity.

The purpose of this study was to obtain an exact solution of the Maxwell equation system for TM-polarised NPCs propagating along the interface between an optically linear magnetic medium and an optically nonlinear medium with saturated nonlinearity.

Materials and Methods

The authors considered a TM-polarised electromagnetic wave propagating along the interface (plane z=0) of an optically nonlinear medium with permittivity saturation (region z>0) and an optically linear magnetic medium (region z<0). The magnetic permeability of a nonlinear medium is equal to one, and the permittivity is denoted as ε. The magnetic permeability and permittivity of a linear medium are denoted by μ_1 and ε_1, respectively. Both environments are non-dissipative. The problem is considered homogeneous towards y. The electric and magnetic fields of the NSP are written as (1-2):

$$\vec{E}(\vec{r},t)=\frac{1}{2}\left(\vec{E}(z)\exp i(kx-\omega t)+c.c.\right),\vec{E}(z)=(E_x,0,E_z) \quad (1)$$

$$\vec{H}(\vec{r},t)=\frac{1}{2}\left(\vec{H}(z)\exp i(kx-\omega t)+c.c.\right),\vec{H}(z)=(0,H,0) \quad (2)$$

The dependence of the permittivity of a nonlinear medium on the intensity is modelled according to the following formula (3):

$$\varepsilon=\varepsilon_{xx}=\varepsilon_{zz}=\varepsilon_0+\varepsilon_2\left(\left|\vec{E}\right|^2\right)=\varepsilon_0+\frac{a(|E_x|^2+|E_z|^2)}{1+b(|E_x|^2+|E_z|^2)} \quad (3)$$

where ε_0 and are the linear and nonlinear parts of the permittivity.

The authors believe that ε_0, a, b, ε_1, μ_1 are valid. Value b is considered integral. Signs ε_0, a, ε_1, μ_1 are arbitrary. The permittivity (3) is a guide for weak fields and tends to the saturation level $\varepsilon_s=\varepsilon_0+a/b$ at high intensities.

The problem is to determine the relationship between the steady-state propagation and the energy flux of the NSP based on the exact solution of the Maxwell equation system for the NSP in the structure under study.

NSP at the interface between magneto-optical matter and nonlinear metamaterial

Components of the NSP field. The components of the NSP field correspond to the following system of equations (4a-4c):

$$\frac{dH}{d\zeta} = i\varepsilon E_x \quad (4a)$$

$$nH = -\varepsilon E_z \quad (4b)$$

$$\frac{dE_x}{d\zeta} - inE_z = i\mu H \quad (4c)$$

where $n \equiv k/q$ is the dimensionless steel distribution $\zeta \equiv zq$ is the dimensionless coordinate; $q = \omega/c$. Magnetic field H is considered valid and integral.

For a linear medium, the solution of system (4a-4c) gives components of the NSP field that decrease exponentially as one distances from the interface. For example, the magnetic field distribution of the NSP has the following form (5):

$$H(\zeta) = \widetilde{H}\exp\,(k_1\zeta) \quad (5)$$

where (6):

$$k_1 \equiv +(n^2 - \varepsilon_1\mu_1)^{1/2} \quad (6)$$

$\tilde{H}$ there is a value of the magnetic field at the interface z=0.

For a nonlinear medium, the solution of system (4a-4c) is based on the general solution obtained by Leung [28] for an arbitrary function $\varepsilon_2(|E|^2)$, which allows expressing the components of the NSP field in terms of ε and determine the dimensionless coordinate ζ as an integral by ε within the range of $\tilde{\varepsilon}$ K ε, where is the permittivity on the surface of a nonlinear medium. Later, this general solution was developed [1] for the permeability expressed by Equation (3). Using the solution [1] and boundary conditions for the tangential components of the field, the constant propagation of NSP can be expressed in terms $\tilde{\varepsilon}$ (7):

$$n^2 = \frac{\varepsilon_1\tilde{\varepsilon}^2((\mu_1\tilde{\varepsilon} - \varepsilon_1)I(\tilde{\varepsilon} - \varepsilon_0) - \mu_1 J(\tilde{\varepsilon} - \varepsilon_0))}{\tilde{\varepsilon}(\tilde{\varepsilon}^2 - \varepsilon_1^2)I(\tilde{\varepsilon} - \varepsilon_0) - (\tilde{\varepsilon}^2 + \varepsilon_1^2)J(\tilde{\varepsilon} - \varepsilon_0)} \quad (7)$$

where $I(\varepsilon-\varepsilon_0)$ and $J(\varepsilon-\varepsilon_0)$ are determined by equations (9) and (10) from [1].

NSP energy flow Q per unit length towards y consists of the flow of energy in a linear medium QL and energy flow in a nonlinear medium QN. Both flows can be obtained by using the expression for constant propagation (7) in equations (21) and (22) from [1].

Results and Discussion

Relationship between energy flow and steady-state NSP propagation

Next, the authors consider the relationship between the steady spread of NSP n and the energy flow of the NSP q (per unit length towards yNSP energy fluxes in linear and nonlinear media for NSP propagating along the interface of an optically linear magnetic ENZ-metamaterial with negative permittivity and an optically nonlinear self-focusing ENZ-metamaterial.

Calculations are performed for the following parameter values: $\lambda = \dfrac{2\pi c}{\omega} = 1.06\mu m$, linear permittivity of the medium ε_1=-0.2; linear part of the permeability of a nonlinear substance ε_0=-0.04, Kerr coefficient $a = 1.76\times10^{-17}$ m²/V² (typical value for a nonlinear optical material multiplied by a gain factor of 400, as in Argyropoulos et al. [27]).

The relationship between the steady-state NSP propagation and the total NSP energy flow per unit length towards y is presented in Figures 1-3.

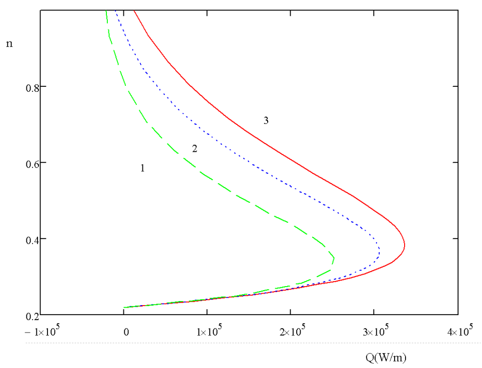

Figure 1. Constant distribution dependence n from the total energy flow of the NSP Q for magnetic permeability μ_1=0.8 at the following saturation levels: 1) ε_s=0.26; 2) ε_s=0.34; 3) $\varepsilon_s = +\infty$

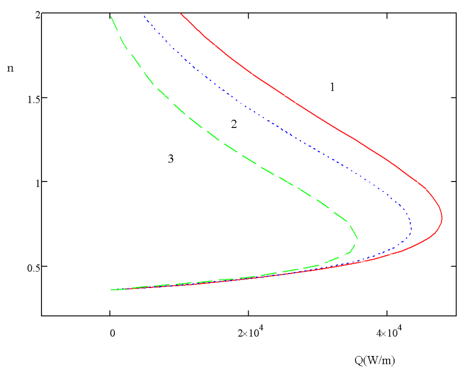

Figure 2. Constant distribution dependence n from the total energy flow of the NSP Q for magnetic permeability μ_1=10 at the following saturation levels: 1) ε_s=0.26; 2) ε_s=0.34; 3) $\varepsilon_s = +\infty$

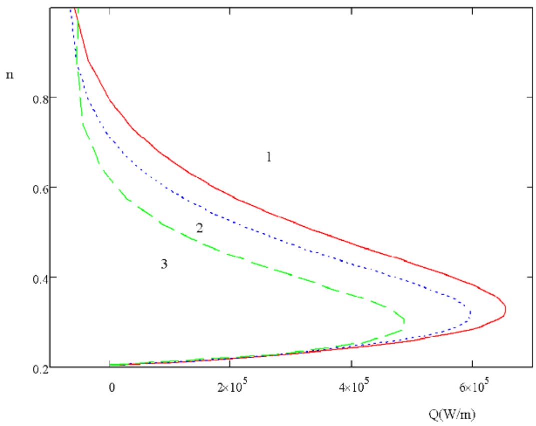

Figure 3.Constant distribution dependence n from the total energy flow of the NSP Q for magnetic permeability μ_1=0.01 at the following saturation levels: 1) ε_s=0.26; 2) ε_s=0.34; 3) ε_s=+∞

Dependency graphs $n=n(Q)$ are S-shaped. For high nonlinearity, the total energy flux of the NSP is negative. The results shown in Figure 1 correspond to the value of the magnetic permeability of a linear medium μ_1=0.8; these graphs are remarkably similar to the graphs for the non-magnetic case given in paper by A.D. Groza [29] (Fig. 3). The fractions of the energy flux in a nonlinear medium and in a linear medium are presented in Figures 4-6.

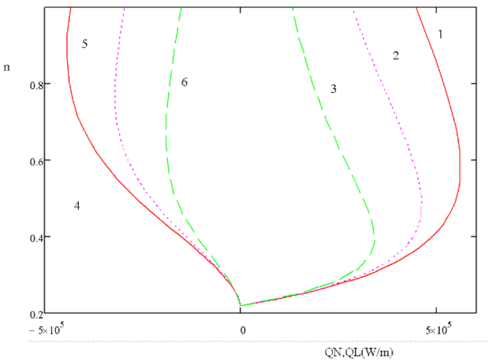

Figure 4. Fraction of the NSP energy flow in a nonlinear medium *QN* (1,2,3) and in a linear environment *QL* (4,5,6) for magnetic permeability μ_1=0.8 at the following saturation levels: 1) ε_s=0.26; 2) ε_s=0.34; 3) ε_s=+∞

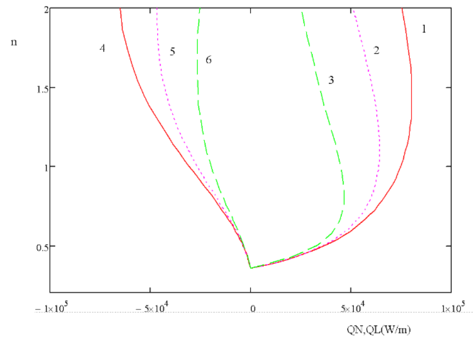

Figure 5. Fraction of the NSP energy flow in a nonlinear medium *QN* (1,2,3) and in a linear environment *QL* (4,5,6) for magnetic permeability μ_1=10 at the following saturation levels: 1) ε_s=0.26; 2) ε_s=0.34; 3) ε_s=+∞

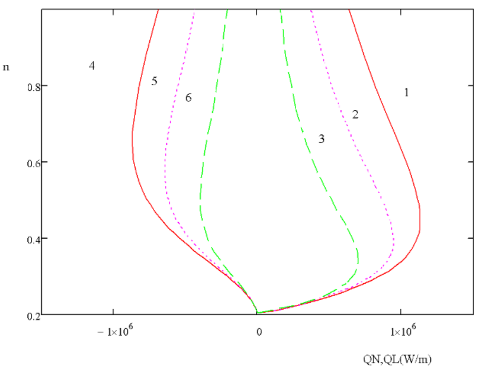

Figure 6. Fraction of the NSP energy flow in a nonlinear medium *QN* (1,2,3) and in a linear medium *QL* (4,5,6) for magnetic permeability μ_1=0.01 at the following saturation levels: 1) ε_s=0.26; 2) ε_s=0.34; 3) ε_s=+∞

The energy flow is always negative in a linear medium and always positive in a nonlinear medium. The modules of these energy fluxes are of the same order of magnitude. Figure 2 and Figure 5 demonstrate the magnetic permeability of a linear medium and the graphs are shifted to lower values of the NSP energy flow.

In Figure 3 and Figure 6, the magnetic permeability has a value close to zero , in this case, the graphs are shifted to higher values of NSP energy fluxes.

In all cases, for the selected value of the steady-state propagation of the NSP, the value of the share of the NSP energy flux in the contacting media increases modulo when the saturation level decreases.

Charts $n=n(Q)$ intersect the axis n if the total energy flow of the NSP is zero. The value of the steady-state propagation, which corresponds to the zero value of the total energy flux of the NSP, is the smallest for the control nonlinearity and increases with decreasing saturation level.

Conclusions

The paper presents an exact solution of the Maxwell equation system for TM-polarised nonlinear surface polaritons propagating along the interface of an optically linear magnetic medium and an optically nonlinear medium with nonlinear saturation. The solution allows calculating the NSP parameters for any signs and values of material parameters of contacting media. Its application to the analysis of NSP properties in the ENZ structure of a magnetic metamaterial with negative permittivity/nonlinear self-focusing ENZ metamaterial allows drawing the following conclusions:

1. The energy flow of NSP is positive in a nonlinear medium and negative in a linear medium. For low levels of nonlinearity, the NSP energy flow in a nonlinear medium dominates. For high levels of nonlinearity, the relative part of the NSP energy flow decreases in a nonlinear medium, the total NSP energy flow tends to zero, and then becomes negative.
2. For a fixed value of the steady-state propagation of NSP, the NSP energy fluxes in contacting media increase modulo when the saturation level decreases. The value of the NSP propagation constant, for which the total NSP energy flux becomes zero, is the smallest for the control nonlinearity and increases with decreasing saturation level.
3. According to the selected value of the steady-state propagation, the energy fluxes of NSP in contacting media increase when the magnetic permeability decreases. The range of changes in steady-state propagation for a positive NSP energy flux narrows when the magnetic permeability tends to zero.

References

[1] Groza AD, Strizhevskii VL. Properties of p-polarized nonlinear surface polaritons. *Physica Status Solidi*. 1991;(163):381.

[2] Huang J-H, Chang R, Leung PT, et al. Nonlinear dispersion relation for surface plasmon at a metal-Kerr medium interface. *Journal of Optics*. 2010;282(7):1412-15.

[3] Pusch A, Shadrivov IV, Hess O, Tsai DP. Self-focusing of femtosecond surface plasmon polaritons. *Optics Express*. 2013;(21):1121.

[4] Giovampaola CD, Engheta N. Digital metamaterials. Nature Materials. 2014;13:1115-21.

[5] Lapine M, Shadrivov IV, Y.S. Kivshar YS. Colloquium: Nonlinear metamaterials. *Review of Modern Physics*. 2014;(86):1093-123.

[6] Urbas AM, Jacob Z, Negro LD, Engheta N, Boardman AD, Egan P., et al. Roadmap on optical metamaterials. *Journal of Optics*. 2016;18:093005-1–093005-53.

[7] Veselago VG. The electrodynamics of substances with simultaneously negative values of ε and μ. *Soviet Physics Uspekhi*. 1968;10(4):509.

[8] Feng S, Halterman K. Perfect absorption in ultrathin epsilon-near-zero metamaterials induced by fast-wave non-radiative modes. *Physical Review B*. 2011;86(16):165103. doi: 10.1103/PhysRevB.86.165103.

[9] Temnov VV, Armelles G, Woggon U, Guzatov D, Cebollada A, Garcia-Martin A, et al. Active magneto-plasmonics in hybrid metal-ferromagnet structures. *Nature Photonics*. 2010;(4):107-11.

[10] Zhu W, Rukhlenko ID, Premaratne M. Graphene-enabled tenability of optical fishnet metamaterials. *Applied Physics Letters*. 2013;(102):011910-1–011910-4.

[11] Mahmoud AM, Engheta N. Wave-matter interactions in epsilon-and-mu-near-zero structures. *Nature Communications*. 2014;(5):5638-1– 5638-7.

[12] Wang Q, Rogers ETF, Gholipour B, Wang C-M, Yuan G, Teng J, et al. Optically reconfigurable metasurfaces and photonic devices based on phase change materials. *Nature Photonics*. 2016;(10):03818-1–03818-12.

[13] Karvounis A, Gholipour B, MacDonald KF, Zheludev NI. All-dielectric phase-change reconfigurable metasurface. *Appl. Phys. Lett*. 2016;(109):051103-1–051103-5.

[14] Amemiya T, Ishikawa A, Kanazawa T, Kang JH. Permeability-controlled optical modulator with Tri-gate metamaterial: Control of permeability on InP-based photonic integration platform. *Scientific Reports*. 2014;(5):8985-1–8985-8.

[15] Maas R, Parsons J, Engheta N, Polman A. Experimental realization of an epsilon-near-zero metamaterial at visible wavelengths. *Nat. Photonics*. 2013;(7):907-12.

[16] Yang X, Hu Ch, Deng H, Rosenmann D, Czaplewski DA, Gao J. Experimental demonstration of near-infrared epsilon-near-zero multilayer metamaterial slabs. *Optics Express*. 2013;21(20):23631-39.

[17] Toal B, McMillen M, Murphy A, Hendren W, Arredondo M, Pollard R. Optical and magneto-optical properties of gold core cobalt shell magnetoplasmonic nanowire arrays. *Nanoscale*. 2014;(6):12905-11.

[18] Atmatzakis E, Papasimakis N, Fedotov V, Zheludev NI. Giant Kerr rotation enhancement in magneto-plasmonic metamaterials. *Proceedings of CLEO: Science and Innovations 2014; 2014; San Jose. San Jose, US: Optica Publishing Group*; 2014. doi: 10.1364/CLEO_SI.2014.STu1H.6.

[19] Toal B, McMillen M, Murphy A, Hendren W, Atkinson R, Pollard R. Tuneable magneto-optical metamaterials based on photonic resonances in nickel nanorod arrays. *Materials Research Express.* 2014;(1):015801-1–015801-11.

[20] Moitra P, Yang Y, Anderson Z, Kravchenko II, Briggs DP, Valentine J. Realization of an all-dielectric zero-index optical metamaterial. *Nature Photonics*. 2013;(7):791-95.

[21] Li Y, Kita S, Munoz Ph, Vulis DI, Yin M, Lončar M, et al. On-chip zero-index metamaterials. *Nature Photonics.* 2015;9(11):738-42.

[22] Vulis DI, Li Y, Reshef O, Yin M, Camayd-Muñoz Ph, Kita S, et al. CMOS-compatible zero-index metamaterial. *Proceedings of CLEO: Science and Innovations 2016*; 2016; San Jose. San Jose, US: Optica Publishing Group; 2016. doi: 10.1364/CLEO_SI.2016.STh3E.8.

[23] Rishad KPM, Li C, Roger T, Hu H, Kallos T, Palikaras G, et al. Z-scan characterization of epsilon-near-zero metamaterial. In *Proc. Conf. PHOTON14*, Session 1, London, UK, 1-4 September 2014.

[24] Pietrzyk M, Kaipurath R, Faccio D, Di Falco A. Epsilon near zero metamaterials for ultra-low power nonlinear applications. *Proceedings of SPIE OPTO; 2015; San Francisco.* San Franciso, US: SPIE Digital Library, 2015. p. 1-11. doi: 10.1117/12.2078884.

[25] Kaipurath RM, Pietrzyk M, Caspani L, Roger T, Clerici M, Rizza C, et al. Optically induced metal-to-dielectric transition in Epsilon-Near-Zero metamaterials. *Scientific Reports*. 2016;(6):27700. doi: 10.1038/srep27700.

[26] Boyd RW, Sipe JE. Nonlinear optical susceptibilities of layered composite materials. *The Journal of the Optical Society of America B.* 1994;11(2):297-303.

[27] Argyropoulos C, Chen P-Y, Alù A. Enhanced nonlinear effects in metamaterials and plasmonics. *Advanced Electromagnetics*. 2012;(1):46.

[28] Leung KM. P-polarized nonlinear surface polaritons in materials with intensity-dependent dielectric functions. *Physical Review B.* 1985;32(8):5093.

[29] Groza AD. Above-light-line nonlinear surface polaritons near the surface of an epsilon-near-zero metamaterial. *Journal of Modern Optics.* 2016;63(2):1-5.

Нелінійні поверхневі поляритони біля межі поділу магніто-оптичної речовини та нелінійного метаматеріалу з близькою до нуля діелектричною проникністю

Андрій Дмитрович Гроза[1], Микола Іванович Сідєлєв[2]

[1]Відкритий міжнародний університет розвитку людини ВНЗ Університет «Україна»
54003, вул., 2-а Воєнна, 22, м. Миколаїв, Україна

[2]Чорноморський національний університет імені Петра Могили
54003, вул. 68 Десантників, 10, м. Миколаїв, Україна

Анотація

Актуальність. Значна увага дослідників привертається до нелінійних поверхневих оптичних хвиль, оскільки вони мають хороші перспективи у застосуванні в системах оптичної обробки інформації, надчутливих сенсорах і сучасних телекомунікаційних компонентах

Мета. Отримати точне рішення системи рівнянь Максвелла для ТМ-поляризованих нелінійних поверхневих поляритонів, що поширюються вздовж межі розділу між оптично лінійним магнітним середовищем і оптично нелінійним середовищем з насиченою нелінійністю.

Методи. Використано аналіз властивостей нелінійних поверхневих поляритонів (НПП) та математичне моделювання залежності діелектричної проникності нелінійного середовища від інтенсивності.

Результати. Досліджено ТМ-поляризовані НПП, що поширюються уздовж межі поділу магніто-оптичного середовища та нелінійно-оптичного метаматеріалу з близькою до нуля діелектричною проникністю (ENZ-метаматеріал). Для НПП в такій структурі отримане точне рішення системи рівнянь Максвелла з урахуванням ефекту насичення оптичної нелінійності. На цій основі досліджено залежності постійного поширення від сумарного потоку енергії НПП та потоків енергії в контактних середовищах у структурі: магнітооптичний ENZ-метаматеріал з негативною діелектричною проникністю / нелінійний самофокусуючий ENZ-метаматеріал.

Висновки. Потік енергії НПП є позитивним в нелінійному середовищі та негативним у лінійному. При зменшенні рівня насиченості потоки енергії НПП у контактуючих середовищах зростають за модулями, якщо значення сталої розповсюдження НПП (СРНПП) фіксоване. Найменше значення СРНПП для керівської нелінійності отримуємо, коли загальний енергетичний потік НПП стає нулевим. Із зменшенням рівня насичення ПРНПП збільшується. При фіксованій СРНПП при зменшенні магнітної проникності потоки енергії НПП у середовищах, що контактують, зростають. Коли магнітна проникність зменшується до нуля і потік енергії НПП позитивний, діапазон зміни СРНПП звужується

Ключові слова: керівська нелінійність, стала розповсюдження, діелектрична проникність нелінійного середовища, магніто-оптичний метаматеріал, магнетик, насичення

Scientific Herald of Uzhhorod University
Series “Physics”

Journal homepage: https://physics.uz.ua/en

Issue 51, 30-38

Received: 07.04.2022. Revised: 22.05.2022. Accepted: 10.06.2022

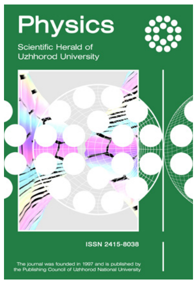

UDC 539.125
PACS 29
DOI: 10.54919/2415-8038.2022.51.30-38

A Simple Model for Describing the Minimum Differential Cross-Section of Elastic Proton Scattering on Protons at High Energies

Norbert Bence[1], Alexander Lengyel[2], Zoltán Tarics[2*]

[1]Uzhhorod National University

88000, 14 Universitetska Str., Uzhhorod, Ukraine

[2]Institute of Electron Physics of the NAS of Ukraine

88017, 21 Universytetska Str., Uzhhorod, Ukraine

Abstract

Relevance. The most modern and widely applied phenomenological theory, which well describes an entire range of physical characteristics of such processes as elastic and inelastic proton-proton and antiproton-proton scattering at high energies, is the Regge poles method in relativistic theory. Based on a simple amplitude, such as the dipole pomeron, where the pomeron is the Regge pole, the researchers add different terms to it. Using such more complex amplitudes, it is possible to explain well or satisfactorily together not only the experimental data for these reactions obtained at the end of the last century, but also the latest ones obtained at the Large Hadron Collider.

Purpose. The purpose of this study is to find numerical values of the amplitude parameters at which the vicinity of minimum of the differential cross-sections of elastic proton scattering on protons at high energies are satisfactorily described, and to answer whether the parameters satisfy the obtained constraints.

Methods. To find the amplitude parameters, the least squares method is used and minima equations are obtained for the squares of differences between the experimental and theoretical values of these cross-sections. These equations are transcendental, and therefore, they are solved by approximation. Within the framework of successive approximations, a method is selected that ensures fast convergence of the process, namely: the faster descent method or the gradient method. Parameter errors are calculated using a covariance matrix. The statistical acceptability of the model is determined according to the Fischer criterion.

Results. Numerical calculations from experimental data of differential cross-sections of elastic *pp*-scattering were used to find the values of the parameters and the scale multiplier of the amplitude. Differential cross-sections are calculated from the amplitude near the minima. The corresponding graphs of these cross-sections are presented. The coincidence with the experiment is satisfactory in most cases, and in some cases, it is of high quality. A covariance matrix is obtained, from which the errors of the model parameters are found. Under general conditions, restrictions on the found approximate values of parameters are derived. It is shown that they satisfy the constraint. According to the Fischer criterion, the statistical acceptability of the model was verified, which turned out to be positive.

Conclusions. The proposed simple amplitude ensures that the Froissart constraint and unitarity are met. It will serve as a seed for constructing more complex amplitudes that will describe a wide range of experiments on proton-proton and antiproton-proton scattering at high energies

Keywords: amplitude, parameter, dipole pomeron, covariance matrix

Suggested Citation:
Bence N, Lengyel A, Tarics Z. A simple model for describing the minimum differential cross-section of elastic proton scattering on protons at high energies. *Scientific Herald of Uzhhorod University. Series “Physics”*. 2022;(51):30-38.

*Corresponding author

Introduction

Regge's theory of complex angular moments in quantum mechanics, which is generalised to relativistic S-matrix in terms of Mandelstam variables, which has been developed for more than 50 years and is used to explain experimental results obtained in processes implemented in high-energy collisions of elementary particles. This primarily concerns pp- and $\bar{p}\,p$-scattering both elastic and inelastic. Over the past 10 years, on the Large Hadron Collider has been obtained data on differential cross-sections (and not only) of the elastic pp-scattering at several energies [1-3]. Measurements at the Collider when two protons collide with a total energy of 7 TeV [2] in the centre of mass system turned out to be decisive, since they were the first experiment after launching the accelerator and showed the potential of the detector.

Phenomenological models of Regge require complex amplitudes containing many terms and even more parameters to describe a large database of experimental data on the total and differential sections, the slope, and curvature parameter of the last section, and the ratio of the real part of the amplitude to its imaginary one at zero transferred momentum. For example, to describe the total cross-section of scatterings in a wide energy region, socalled reggeones are introduced, i.e., f- and ω-mesons, nonlinear trajectories with the intersept larger than 1 [4]. Adding such terms to the amplitude means that 6 added parameters appear. To explain more physical quantities in wide areas of variables, one needs to add other terms: introduce a tripole pomeron, odderon [5-7]. Even more parameters need to be considered if the spin structure of the amplitude is factored [5; 8; 9].

Most models that simultaneously explain the physical quantities listed above necessarily contain in the amplitude the pomeron [4; 10] (and possibly odderon), its trajectory, i.e., they take such a primitive amplitude as a basis. The simplest one includes a dipole pomeron, and it corresponds to the first degree $\ln s$, where s is the square of the energy of protons in the system of their centre of mass. The tripole pomeron corresponds to $\ln^2 s$, etc.

Keeping in mind the optical theorem that relates the amplitude to the total cross-section, instead of the amplitude as a sum in degrees of logarithm, an expression for the total cross-section of the process can be written. However, the already tripole pomeron violates the unitarity of the theory, which is often ignored in numerical calculations, considering that the current high energies are far from asymptotically large, where this violation becomes noticeable. To restore unitarity, as a rule, the amplitude over which the so-called eikonal transformation is performed is used [11; 12].

In this paper, the authors investigate the simple dipole pomeron amplitude proposed in [13] and containing two exponents with a dependence on the square of the transferred impulse, i.e., the diffraction cone of the differential cross-section is described by a combination of two exponents. To determine the model parameters within the framework of regression (numerical calculations), the least squares method will be used, which leads to equations whose solutions are these parameters. Using them, differential cross-sections in the vicinity of their minimum will also be calculated in comparison with experimental values. Parameter errors will be determined. Constraints on parameters will also be obtained, the implementation of which will be directly checked. The statistical acceptability of the model will also be determined.

Materials and Methods

In [13], it was shown that the amplitude of a dipole pomeron with two exponential dependences on the square of the transferred momentum in the centre of mass system for pp-scattering at high energies leads to the expression of a differential cross-section of the process that has extrema, including a minimum, as well as an experimental curve for each energy of available experiments. The trajectory of the pomeron is chosen so as not to break the unitarity, i.e., its intersept (t=0) equals 1: $\alpha(t)=1+\alpha' t$, where $\alpha'=0.266$ GeV^2, t is the square of the transferred impulse is specified. The amplitude has terms with independent parameters a, b, c, which also affect the shape of the theoretical curve. It also has a common multiplier that sets its scale. The specified amplitude has the following form:

$$P(s,t) = isg_0[e^{at} + ce^{bt}\ln(-i\frac{s}{s_0})](-i\frac{s}{s_0})^{\alpha(t)\text{-}1} \quad (1)$$

where the Mandelstam variables are $s=(p_1+p_2)^2$ and $t=(p_1-p_3)^2$, p_1, p_2 are the proton initial four-impulses, p_3 is the four-impulse of a scattered proton, $s_0=1$ GeV^2, g_0 is the scale multiplier, a, b, c are the mentioned parameters.

In amplitude (1), unknown parameters are found using numerical calculations. To calculate the amplitude parameters from experimental data of differential cross-sections, the least squares method, which is widely used in statistics, is used, which searches for the minimum square of the difference between the theoretical and experimental values of a physical quantity. The system of three equations obtained using this method is solved by the rapid descent method [14], or otherwise by the gradient method. It was chosen because upon performing calculations in consecutive approximations, i.e., iterations, it quickly converges to a solution. This method reduces the amount of machine time upon calculations.

For compactness and convenience of solving a system of equations, it is written in matrix form. This allows creating simple and transparent programmes for finding approximate parameter values.

The equations themselves are transcendental, so they are solved approximately. This way, the parameters will have errors. To determine these errors, a covariance matrix is calculated, on the diagonal of which there are squares of standard deviation, i.e., squares of errors.

For day, experimental data for the differential cross-section of elastic pp-scattering at high energies exist at eight energies from 23.5 GeV to 13 TeV. The limitation of the model is that the proposed simple amplitude with three parameters is only an initial one for constructing more complex amplitudes. It is important that this initial amplitude describes the minima of the specified cross-sections and their vicinity. However, this description for each energy can only be made with its own set of parameters.

As noted above, with a single set of parameter values, such description is possible with more complex amplitudes, which contain considerably more terms and, accordingly, many more parameters.

The complete set of parameters, which is an approximate set, is subject to added verification. It lies in obtaining an answer to whether the parameters satisfy the resulting general constraints, which are written as inequalities. If the result is positive, one can be sure that the accuracy of calculations is sufficient. Substituting parameters in the inequality showed that all of them are fulfilled, and the obtained values are quite far from the limit values of the constraints. Furthermore, the inequalities obtained earlier in [13] are also satisfied.

However, to find out the adequacy of the model, it is necessary to verify its statistical acceptability, which was done using the Fischer criterion [15]. This simple statistical method is widely used in the regressive analysis of experimental data by models, i.e., upon their theoretical explanation. All values of the Fischer quantile turned out to be less than the critical one, i.e., the model is statistically acceptable.

Results and Discussion

According to the least squares method, wherein the square of the difference between the experimental and theoretical values of a physical quantity reaches a minimum, the amplitude parameters *a, b* and *c* are found (1).

After differentiating the specified square by these parameters and equating the results with zero, a system of three equations (2.1-2.3) is obtained as follows:

$$\sum_{i=1}^{21}\left[(f_i)_{\exp} - f_i\right]\frac{\partial f_i}{\partial a} = 0 \tag{2.1}$$

$$\sum_{i=1}^{21}\left[(f_i)_{\exp} - f_i\right]\frac{\partial f_i}{\partial b} = 0 \tag{2.2}$$

$$\sum_{i=1}^{21}\left[(f_i)_{\exp} - f_i\right]\frac{\partial f_i}{\partial c} = 0 \tag{2.3}$$

In equations (2.1-2.3) $(f_i)_{\exp}$ – experimental values of these cross-sections at energies of 2.76, 7, 13 TeV [1-3], 23.5, 30.7, 44.7, 52.8 TV 62.5 GeV (for references to experimental data at these energies, see [5]) for the squared of transferred impulse t_i (10 on both sides of the minimum, except for the energy of 2.76 TeV, for which it was impossible to do this from the data available), f_i – their theoretical values (3). In Equation (3) $g=g_0 s_0$, w=0.3894 $mb{\cdot}GeV^2$ – transfer coefficient from units where $\hbar$=c=1, to mb/GeV^2.

$$f_i = f(s,t_i) = \frac{d\sigma(s,t=t_i)}{dt} = \frac{\pi g^2}{s^2} w\left[(e^{at_i} + ce^{bt_i}\ln\frac{s}{s_0})^2 + \left(\frac{\pi c}{2}\right)^2 e^{2bt_i}\right]\left(\frac{s}{s_0}\right)^{2\alpha(t_i)} \tag{3}$$

Expanded form of Equation (2.1-2.3) for real functions F_i, they will be written as follows (4-9):

$$F_1 = \sum_{i=1}^{21}\left[(f_i)_{\exp} - f_i\right]\frac{\partial \tilde{f}_i}{\partial a} = 0 \tag{4}$$

$$F_2 = \sum_{i=1}^{21}\left[(f_i)_{\exp} - f_i\right]\frac{\partial \tilde{f}_i}{\partial b} = 0 \tag{5}$$

$$F_3 = \sum_{i=1}^{21}\left[(f_i)_{\exp} - f_i\right]\frac{\partial \tilde{f}_i}{\partial c} = 0 \tag{6}$$

where:

$$\frac{\partial \tilde{f}_i}{\partial a} = t_i e^{at_i}(e^{at_i} + ce^{bt_i}\ln s)s^{2\alpha' t_i} \tag{7}$$

$$\frac{\partial \tilde{f}_i}{\partial b} = t_i\left[ce^{bt_i}\ln s(e^{at_i} + ce^{bt_i}\ln s) + \left(\frac{\pi c}{2}\right)^2 e^{2bt_i}\right]s^{2\alpha' t_i} \tag{8}$$

$$\frac{\partial \tilde{f}_i}{\partial c} = \left[2\ln s(e^{at_i} + ce^{bt_i}\ln s)e^{bt_i} + \frac{\pi^2 c}{2}e^{2bt_i}\right]s^{2\alpha' t_i} \tag{9}$$

Functions F_i can be considered the elements of the matrix $\boldsymbol{F}$ (10):

$$F = \begin{pmatrix} F_1 \\ F_2 \\ F_3 \end{pmatrix} \tag{10}$$

To solve the system of Equations (4-6) according to the rapid descent method, as in [14], an auxiliary function is introduced as follows:

$$\Phi = F^T F = F_1^2 + F_2^2 + F_3^2 \tag{11}$$

where in expression (11) *T* is the matrix transposition sign. Values of parameters that are the solution of the equation $\Phi=0$, are also solutions of the system of Equations (4-6).

On l^{th} step of successive approximations, solutions for parameters are obtained according to Formula (12):

$$A_{l+1} = A_l - \frac{F_l^T W_l W_l^T F_l}{(W_l W_l^T F_l)^T (W_l W_l^T F_l)} W F_l \tag{12}$$

where (13):

$$A = \begin{pmatrix} a \\ b \\ c \end{pmatrix} \tag{13}$$

while the Jacobi matrix (14)

$$W = \begin{pmatrix} \frac{\partial F_1}{\partial a} & \frac{\partial F_1}{\partial b} & \frac{\partial F_1}{\partial c} \\ \frac{\partial F_2}{\partial a} & \frac{\partial F_2}{\partial b} & \frac{\partial F_2}{\partial c} \\ \frac{\partial F_3}{\partial a} & \frac{\partial F_3}{\partial b} & \frac{\partial F_3}{\partial c} \end{pmatrix} \tag{14}$$

The elements of matrix (14) have the form (15-23):

$$\frac{\partial F_1}{\partial a} = \sum_{i=1}^{21}\left[-\frac{\partial f_i}{\partial a}\frac{\partial \tilde{f}_i}{\partial a} + \left((f_i)_{\exp} - f_i\right)\frac{\partial^2 \tilde{f}_i}{\partial a^2}\right] \tag{15}$$

$$\frac{\partial F_1}{\partial b} = \sum_{i=1}^{21}\left[-\frac{\partial f_i}{\partial b}\frac{\partial \tilde{f}_i}{\partial a} + \left((f_i)_{\exp} - f_i\right)\frac{\partial^2 \tilde{f}_i}{\partial a \partial b}\right] \quad (16)$$

$$\frac{\partial F_1}{\partial c} = \sum_{i=1}^{21}\left[-\frac{\partial f_i}{\partial c}\frac{\partial \tilde{f}_i}{\partial a} + \left((f_i)_{\exp} - f_i\right)\frac{\partial^2 \tilde{f}_i}{\partial a \partial c}\right] \quad (17)$$

$$\frac{\partial F_2}{\partial a} = \sum_{i=1}^{21}\left[-\frac{\partial f_i}{\partial a}\frac{\partial \tilde{f}_i}{\partial b} + \left((f_i)_{\exp} - f_i\right)\frac{\partial^2 \tilde{f}_i}{\partial a \partial b}\right] \quad (18)$$

$$\frac{\partial F_2}{\partial b} = \sum_{i=1}^{21}\left[-\frac{\partial f_i}{\partial b}\frac{\partial \tilde{f}_i}{\partial b} + \left((f_i)_{\exp} - f_i\right)\frac{\partial^2 \tilde{f}_i}{\partial b^2}\right] \quad (19)$$

$$\frac{\partial F_2}{\partial c} = \sum_{i=1}^{21}\left[-\frac{\partial f_i}{\partial c}\frac{\partial \tilde{f}_i}{\partial b} + \left((f_i)_{\exp} - f_i\right)\frac{\partial^2 \tilde{f}_i}{\partial b \partial c}\right] \quad (20)$$

$$\frac{\partial F_3}{\partial a} = \sum_{i=1}^{21}\left[-\frac{\partial f_i}{\partial a}\frac{\partial \tilde{f}_i}{\partial c} + \left((f_i)_{\exp} - f_i\right)\frac{\partial^2 \tilde{f}_i}{\partial a \partial c}\right] \quad (21)$$

$$\frac{\partial F_3}{\partial b} = \sum_{i=1}^{21}\left[-\frac{\partial f_i}{\partial b}\frac{\partial \tilde{f}_i}{\partial c} + \left((f_i)_{\exp} - f_i\right)\frac{\partial^2 \tilde{f}_i}{\partial b \partial c}\right] \quad (22)$$

$$\frac{\partial F_3}{\partial c} = \sum_{i=1}^{21}\left[-\frac{\partial f_i}{\partial c}\frac{\partial \tilde{f}_i}{\partial c} + \left((f_i)_{\exp} - f_i\right)\frac{\partial^2 \tilde{f}_i}{\partial c^2}\right] \quad (23)$$

Errors in the values of parameters (13) that occur when solving equations (4-6) are obtained from the diagonal elements of the covariance matrix [15]. This matrix has the following form (24):

$$B = S^2 R^{-1}, \quad R^{-1} = -\mu W^T \quad (24)$$

where S^2 is the estimated value of the square of the standard deviation σ^2, μ is the multiplier before $\boldsymbol{WF}_l$ in Formula (12).

This is the estimated value of [15] (25):

$$S^2 = \frac{Q_{min}}{n - m} \quad (25)$$

where n is the number of experimental data used in calculations, m is the number of parameters. Value Q_{min} by definition (26):

$$Q_{min} = \sum_{i=1}^{21}(\xi_i - \tilde{y}_i)^2 = (\xi - \tilde{y})^T(\xi - \tilde{y}) \quad (26)$$

where $\boldsymbol{\xi}$ is the column of experimental values of differential cross-sections, $\tilde{y}$ is the column of theoretical values (3) of these cross-sections when found g, a, b, c.

By entering a matrix-column $\boldsymbol{\Delta\xi}$, elements of which are $\boldsymbol{\Delta}\xi_i = x_i - f_i$, and using the decomposition by parameters at a fixed energy, the following expression (27) is obtained:

$$\xi_i - f\left(t_i, \tilde{A}\right) = \xi_i - y_i - \sum_{k'=1}^{m}\frac{\partial f(t_i, A)}{\partial A_{k'}}\left(\tilde{A}_{k'} - A_{k'}\right) + \dots = \Delta\xi_i - \sum_{k'=1}^{m} D_{ik'}\,\Delta A_{k'} + \dots \quad (27)$$

where $y_i = \xi_i - f(t_i, \boldsymbol{A})$; $D_{ik} = \partial f(t_i, \boldsymbol{A})/\partial A_k$; $\Delta A_{k'} = \tilde{A}_{k'} - A_{k'}$; m – number of parameters.

After performing some transformations in (27), the following equation is obtained (28):

$$Q_{min} = \Delta\xi^T(E - WDR^{-1}D^T)W(E - DR^{-1}D^TW)\Delta\xi \quad (28)$$

where E is the unit matrix.

Together with experimental ones, Figures (1-8) demonstrate theoretical cross-sections in the vicinity of minima, which are calculated for the found values of parameters and the scale multiplier.

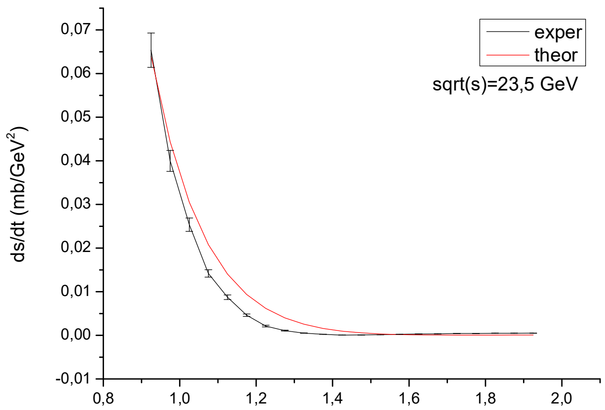

Figure 1. Differential cross-section elastic pp-scattering at $\sqrt{s}$= 23.5 GeV

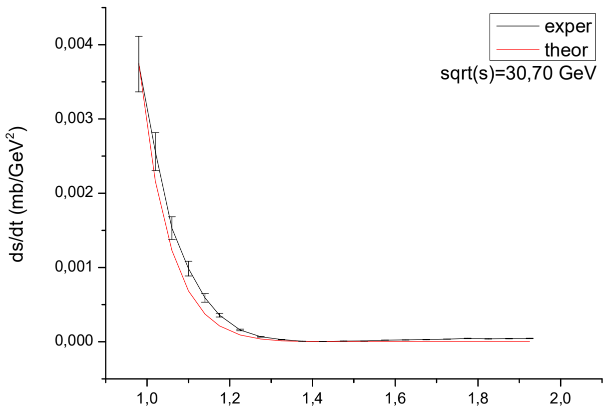

Figure 2. Differential cross-section of elastic pp-scattering at $\sqrt{s}$=30.7 GeV

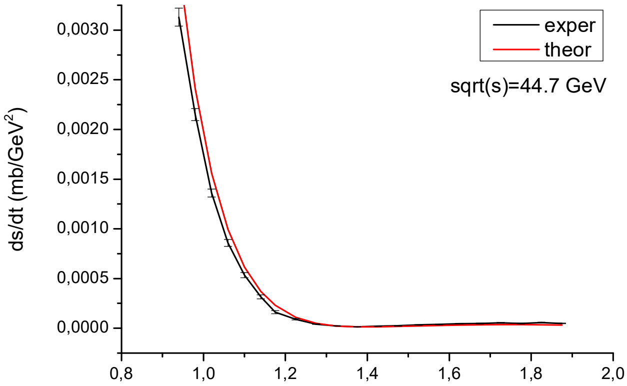

Figure 3. Differential cross-section elastic pp-scattering at √s= 44.7 GeV

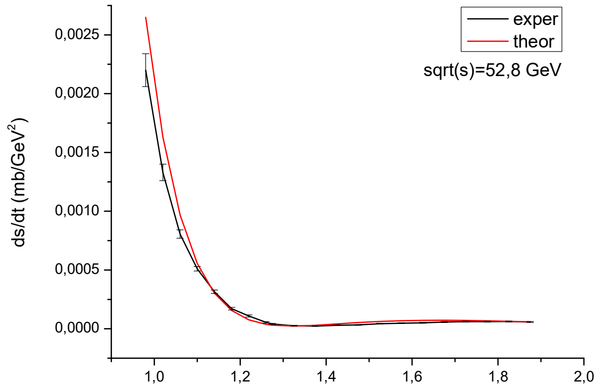

Figure 4. Differential cross-section of elastic pp-scattering at √s= 52.8 GeV

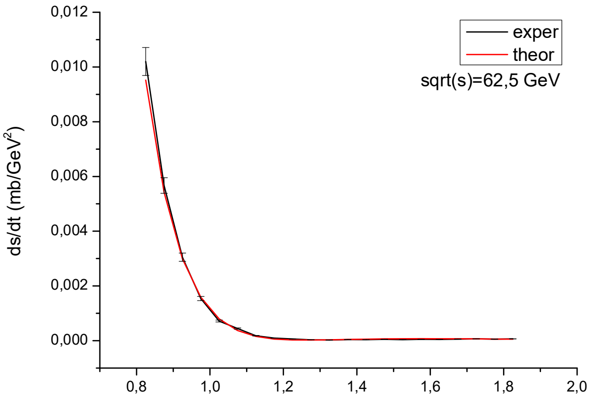

Figure 5. Differential cross-section elastic pp-scattering at √s= 62.5 GeV

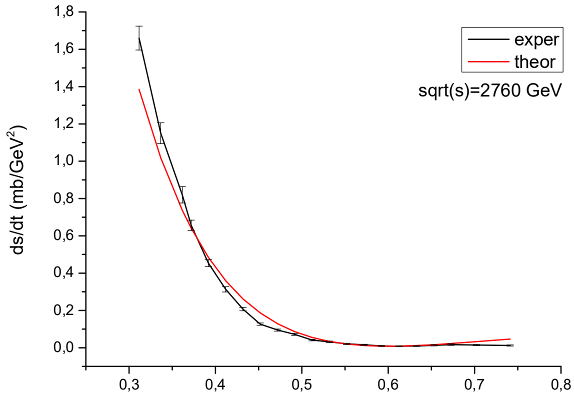

Figure 6. Differential cross-section of elastic pp-scattering at √s=2.76 GeV

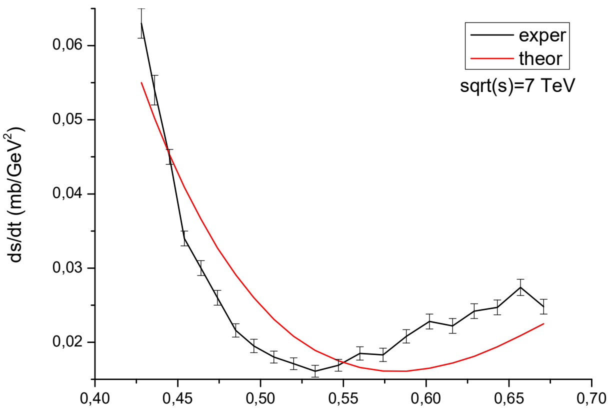

Figure 7. Differential cross-section elastic pp-scattering at √s=7 TeV

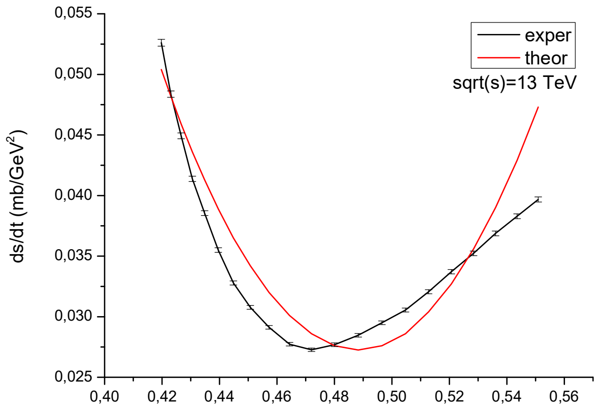

Figure 8. Differential cross-section of elastic pp-scattering at √s=13 TeV

As can be seen from the figures, the graphs of differential cross-sections of the model up to an energy of 2.76 TeV are in satisfactory agreement with the experimental data. Notably, the shapes of the theoretical curves for all energies are similar to the experimental ones, but Figures 6-8 demonstrate noticeable shifts between them, but not in all sections of the curves. This means that in these cases, the parameters found were farther from their exact values, which exist only theoretically. The cross-sections in Figures 1-5 turned out to be the closest to the experimental ones, i.e., better parameters were found here than in earlier cases. The quality of parameters depends on the choice of their zero approximation upon solving equations. While this initial choice is quite arbitrary. The worst agreement with the experiment is observed at 7 TeV. But in this case, the experimental errors are also much larger than at other energies. The need to improve the statistics of this experiment is drawn in the study [16]. However, the experiment for *pp*-scattering at 7 TeV has not yet been repeated. In models with a larger number of parameters, a better match with the experiment can be achieved.

The values of the scale multiplier and model parameters obtained from equations (2-4) are shown in Table 1. Table 1 also demonstrates the parameter errors calculated using the covariance matrix (24). They are insignificant, except for the parameter ***c*** at energies of 2.76, 7, and 13 TeV, for which they are 8.5%, 7.0%, and 4.4%, respectively.

Table 1. Values of the scale multiplier and parameters at different energies

No.	$\sqrt{s}$, GeV	g	a, GeV^{-2}	b, GeV^{-2}	c
1.	23.5	0.254	-0.3739±0.001	1.3990±0.004	-3.148±0.001
2.	30.7	0.3004	0.9523±0.002	3.95±0.005	-10.10±0.005
3.	44.7	1.138	0.645±0.00001	-0.562±0.000004	-0.01927±0.0003
4.	52.8	0.1823	-0.512±0.001	1.9365±0.002	-2.981±0.0007
5.	62.5	0.1763	-0.5436±0.0004	2.0406±0.001	-2.9406±0.0005
6.	2760	1.930	-2.8607±0.0010	-0.6804±0.0017	-0.2354±0.020
7.	7000	2.3825	-3.65±0.0002	-2.901±0.0002	-0.08563±0.006
8.	13000	1.536	-5.3738±0.0002	-4.2338±0.0002	-0.0912±0.004

In [13], a constraint on the parameters a, b, c was obtained provided that $a>0$, $b<0$, which is not common. The following is a constraint for arbitrary valid values a and b. Recall that the solution $x=e^{(a-b)t}$ (expression (9) for equation (10) in [13]) is a positive number, i.e., only positive solutions of the quadratic equation are considered. General view of such equation (29):

$$px^2+qx+r=0 \tag{29}$$

Positive solutions are obtained in the following cases (30):

$$\begin{gathered} p>0,\ -q+\sqrt{q^2\text{-}4pr}>0, \\ p>0,\ -q-\sqrt{q^2-4pr}>0, \\ p<0,\ -q+\sqrt{q^2-4pr}<0, \\ p<0,\ -q-\sqrt{q^2-4pr}<0 \end{gathered}$$

For equation (10) in [13] $p=a+\alpha'L$, $q=-|c|L(a+b+2\alpha'L)$, $r=c^2(b+\alpha'L)(L^2+\pi^2/4)$, $L=\ln(s/s_0)$]. Thus, for the parameters a, b, c four groups of constraints are obtained (31.1-31.4):

1) $p>0,\ q>0,\ r<0;\ a>0,\ b<-(a+2\alpha'L);\ -\alpha'L<a<0,\ b<-\alpha'L,\ b<|a|-2\alpha'L;$
2) $p>0,\ q<0,\ r<q^2/4p;\ a>0,\ b>-(a+2\alpha'L),\ (b+\alpha'L)(L^2+\pi^2/4)<L^2(a+b+2\alpha'L)^2/4(a+\alpha'L);\ -\alpha'L<a<0,\ b>|a|-2\alpha'L,\ (b+\alpha'L)(L^2+\pi^2/4)<L^2(a+b+2\alpha'L)^2/4(a+\alpha'L)$ (31.1)

$$p>0,\ q<0,\ r>0;\ -\alpha'L<a<0,\ b>-\alpha'L,\ b>|a|-2\alpha'L; \tag{31.2}$$

$$p<0,\ q>0,\ -\alpha'L<a<0,\ b<-\alpha'L,\ b<|a|-2\alpha'L); \tag{31.3}$$

$$p<0,\ q<0,\ r>0;\ -\alpha'L<a<0,\ b>-\alpha'L,\ b>|a|-2\alpha'L \tag{31.4}$$

Table 2 demonstrates the calculated coefficients of quadratic equation (29).

Table 2. Values of the coefficients of equation (29) and its discriminant factor

1.	$\sqrt{s}$, GeV	$\ln(s/s_0)$	p, GeV^{-2}	q, GeV^{-2}	r, GeV^{-2}	($p>0$), ($r<$) $q^2/4p$, GeV^{-2}
2.	23.5	6.3140	1.3056	-87.1414	1,291.52	1,454.05
3.	30.70	6.8485	2.7740	-591.1049	29,067.25	31,489.28
4.	44.7	7.5999	2.6666	-0.6043	0.0326	0.0342
5.	52.8	7.9330	1.5982	-133.4911	2,351.80	2,787.49
6.	62.5	8.2703	1.6563	-143.4081	2,598.50	3,104.19
7.	2,760	15.8460	1.3543	-18.2366	49.66	61.39
8.	7,000	17.7073	1.0601	-4.3508	4.19	4.46
9.	13,000	18.9454	-0.3343	-0.8144	2.42	–

In this table, for the collision energies at the found values of the parameters, the coefficients of equation (29) are given and for $p>0$ factor that is included in the discriminant. Since all r are positive, then for (unique) $p<0$, the discriminant is always positive, i.e., it does not give any restriction on the coefficients. For the complete set of parameter values, the coefficient q turned out to be negative, this reduces the number of resulting irregularities that need to be verified. This also applies to inequalities for which $r<0$.

Further, Table 3 demonstrates the calculated corresponding parts of the inequalities, which include the model parameters.

Table 3. Calculated values of the expressions from inequalities (31.1, 31.2, 31.4) and inequality (23) from the study [13] for the corresponding values of parameters *a, b* and *c*

, GeV	(p>0) a>0	b	(b>) -(a+2α'L)	(b+α'L)(L²+π²/4)<L² (a+b+2'L)²/4(a+'L), GeV⁻²	
	(31.1), 2)				
30.70	0.9523	3.95	-4.5957	284.9<308.8	
44.7	0.645	-0.562	-4.6881	87.9<92.2	
	(p>0) a<0	b5	(b>) |a|-2α'L	(b+α'L)(L²+π²/4)<L²(a+ +b+2α'L)²/4(a+α'L)	
23.5	-0.3739	1.3990	-2.9851	130.33<146.72	
52.8	-0.512	1.9365	-3.7084	264.65<313.69	
62.5	-0.5436	2.0406	-3.8562	300.50<358.98	
2760	-2.8607	-0.6804	-5.5694	896.25<1107.88	
7000	-3.65	-2.901	-5.7703	571.72<608.73	
	(31.2)				
	(p>0) a<0	*b12*	-α'L (<a<0)	(b>) |a|-2α'L	
23.5	-0.3739	1.3990	-1.6785	-2.9830	
52.8	-0.512	1.9365	-2.1094	-3.7068	
62.5	-0.5436	2.0406	-2.1998	-3.8060	
2760	-2.8607	-0.6804	-4.2161	-5.5715	
7000	-3.65	-2.901	-4.7109	-5.7715	
	(31.4)				
	(p<0), a (<0)	b19	(a<) -α'L	(b>) -α'L	(b>) |a|-2α'L
13000	-5.3738	-4.2338	-5.0395	-5.0395	-4.7052
	a	*b*	*c*	*(πα'/2√a)²*	*4a/(πc)²*
44.7	0.645	-0.562	-0.01927	0.2707	703.97

Table 3 shows numerical calculations of inequalities (31.1, 31.2) and (31.4), and from (31.1) only the second part was to be calculated. This is marked in the second line. The reason is related to the signs of the coefficients of the quadratic equation, as already explained in the previous paragraph. The same reason for the lack of inequality analysis (31.3).

The first column of the table contains the values of the collision energies, and the second and third columns contain the values of the parameters a and b. In the fourth column up to end including the twentieth row, the calculated values of the left or right parts of the corresponding inequalities are given, and in parentheses — the parameters that relate to the constraint. Similarly, the fifth column shows the values of the left and right sides of the corresponding inequalities.

The last two rows of the table represent the results of calculations of inequality (23) obtained in [13] with parameter constraints not under general conditions.

Table 3 demonstrates that for the entire set of parameters *a, b* and *c* the inequalities are met. Notably, for the corresponding a and b, the inequality (21) from [13] is also performed: a | b |>$(\pi\alpha'/2)^2$=0.15.

The possibility of using the model for further generalisations is determined according to the Fischer criterion [15]. It is characterised by the correlation of the remaining amount to the recovery amount. The first sum considers the errors of calculations based on the theoretical model, where there are both experimental errors and errors from an approximate solution of equations, and the second – only experimental errors. The Fischer quantile is calculated according to the formula (32):

$$F = \frac{\sum_{i=1}^{21}\left[(f_i)_{\text{exp}} - f(s,t_i)\right]^2}{\sum_{i=1}^{21}\left[(f_i)_{\text{exp}} - \bar{f}_{\text{exp}}\right]^2}\frac{n}{m} \tag{32}$$

where f_{exp} is the average value of the experimental data sample, m is the number of parameters, n is the number of selected experimental points. The resulting quantiles are presented in Table 4.

Table 4. Value of Fischer quantiles for collision energies

	$\sqrt{s}$, GeV	F	Tabular value of F for m=3, n=21 with a probability of 95% [15]
1	23.5	0.030	3.07
2	30.70	0.020	
3	44.7	0.068	
4	52.8	0.049	
5	62.5	0.0043	
6	2,760	0.37	
7	7,000	0.036	
8	13,000	0.0072	

In Table 4 for high energies at which there are experimental data of differential cross-sections of elastic *pp*-scattering represented is calculated according to the Fischer quantile formula (31). The sample average for each energy is the arithmetic mean of 21 experimental points, which was used in calculating the parameters. The third column shows that with the most used 95% confidence in practice, Fischer quantiles are less than the critical value. Thus, the model is statistically acceptable.

Conclusions

In the amplitude of elastic *pp*-scattering, which contains a dipole pomeron with a linear trajectory and its intersept equals 1, and the diffraction cone of the differential cross-section is described by two exponents, the values of the parameters and the scaling factor were found by the regression method involving the least squares method. With these values, the differential cross-sections around their minima were calculated for eight energies. They coincide better with the experiment at energies from 23.5 to 62.5 GeV than for energies of 2.76, 7, and 13 TeV. The difference between the experiment and the theory at an energy of 7 TeV is quite noticeable. This is primarily due to considerably larger experimental errors than in other experiments. The proximity of the theory to the experiment characterises the quality of the found parameters, which in numerical calculations largely depends on the successful choice of their initial values upon iteration. On the other hand, such a simple amplitude, which is only primitive for constructing a complex one containing more than 20 parameters, cannot give such a qualitative description as a complex one.

The errors of the parameters were calculated, which turned out to be small. This indicates a sufficient number of consecutive approximations upon performing calculations.

The constraints that the parameters must meet are found. Substituting them into constraint expressions showed that the inequalities hold. This also indicates sufficient accuracy of calculations.

As a result of verifying the statistical acceptability of the model using the Fischer method, it turned out to be positive. Thus, the amplitude considered in the article with the found parameters can be basic in the construction of complex amplitudes for describing a wider range of physical quantities in *pp*-scattering.

References

[1] Antchev G, Aspell P, Atanassov I, Avati V, Baechler J, Berard V, et al. Elastic differential cross-section dσ/dt at $\sqrt{s}$=2.76 TeV and implications on the existence of a colourless C-odd three-gluon compound state. *European Physical Journal C*. 2020;(80):91-1–91-10.

[2] Antchev G, Aspell P, Atanassov I, Avati V, Baechler J, Berard V, et al. Measurement of proton-proton elastic scattering and total cross-section at $\sqrt{s}$=7 TeV. *Europhys. Lett.* 2013;101:21002-1–21002-8.

[3] Antchev G, Aspell P, Ciesielski R, Avati V, Baechler J, Baldenegro C, et al. Elastic differential cross-section measurement at $\sqrt{s}$=13 TeV by TOTEM. *European Physical Journal C*. 2019;(79): 861-1–861-20.

[4] Jenkovszky L, Schicker R, Szanyi I. Elastic and diffractive scatterings in the LHC era. *International Journal of Modern Physics E*. 2018;(27):1830005-1–1830005-44.

[5] Bence N, Lengyel A, Tarics Z, Martynov E, Tersimonov G. Froissaron and Maximal Odderon with spin-flip in pp and high energy elastic scattering. *European Physical Journal A*. 2021;(57):265-1–265-11.

[6] Shabelski YuM, Shuvaev AG. Unified description of LHC data on elastic pp scattering. *Modern Physics Letters A*. 2019;(33):1950305-1–19530507.

[7] Martynov E, Nicolescu B. Odderon effects in the differential cross-sections at Tevatron and LHC energies. *European Physical Journal C*. 2019;(79);461-1–461-14.

[8] Hagiwara Y, Hatta Y, Pasechnik R, Zhou J. Spin-dependent Pomeron and Odderon in elastic proton-proton scattering. *European Physical Journal C*. 2020;(80):427-1–427-19.

[9] Kopeliovich BZ, Krelina M, Potashnikova IK. Probing the Pomeron spin structure with Coulomb-nuclear interference. *Physical Letters B*. 2021;(816):136262-1–136262-6.

[10] Campos SD. An approach to the leading Regge pole. *Physica Scripta.* 2020;(95):065302-1–065302-10.
[11] Broilo M, Fagundes DA, Luna EGS, Peláez M. Soft Pomeron in light of the LHC correlated data. *Physical Review D.* 2021;(103):014019-1–014019-15.
[12] Godizov AA. High-energy elastic diffractive scattering of nucleons in the framework of the two-Reggeon eikonal approximation (from U-70 to LHC). *European Physical Journal C.* 2022;(82):56-1–56-13.
[13] Tarics ZZ. On the question of minima and maxima in differential sections of elastic proton-proton scattering at high energies. *Scientific Herald of Uzhhorod University. Series "Physics".* 2006;(19):176-80.
[14] Demidovich BP, Maron IA. Fundamentals of computational mathematics. Third edition, cor. Moscow: Science; 1966. 664 p.
[15] Lavrenchik VN. Setting up a physical experiment and statistical processing of its results. Kyiv: Publishing House Energoatom; 1986. 272 p.
[16] Jenkovszky L, Szanyi I. Structures in the diffraction cone: The "break" and "dip" in high-energy proton-proton scattering. *Mod. Phys. Lett.* 2017;(32):1750116.

Проста модель для опису околу мінімуму диференціального перерізу пружного розсіяння протонів на протонах за високих енергій

Норберт Йосипович Бенце[1], Олександр Іванович Лендєл[2], Золтан Золтанович Торич[2]

[1]Ужгородський національний університет
88000, вул. Університетська, 14, м. Ужгород, Україна

[2]Інститут електронної фізики НАН України
88017, вул. Університетська, 21, м. Ужгород, Україна

Анотація

Актуальність. Найсучаснішою і широко застосованою феноменологічною теорією, яка добре описує цілий спектр фізичних характеристик таких процесів як пружне і непружне протон-протонне та антипротон-протонне розсіяння за високих енергій, є метод полюсів Редже в релятивістській теорії. Виходячи з простої амплітуди, наприклад дипольної померонної, де померон є полюсом Редже, дослідники додають до неї різні члени. За допомогою таких складніших амплітуд вдається добре або задовільно пояснити разом не тільки експериментальні дані для згаданих реакцій, отримані в кінці минулого століття, але й останні, одержані на Великому адронному колайдері.

Мета. Метою статті є знаходження чисельних значень параметрів амплітуди, при яких задовільно описуються околи мвнімумів диференціальних перерізів пружного розсіяння протонів на протонах за високих енергій, а також відповіль на питання, чи задовольняють параметри отриманим обмеженням.

Методи. Для знаходження параметрів амплітуди використано метод найменших квадратів і отримано рівняння мінімумів для квадратів різниць між експериментальними та теоретичними значеннями зазначених перерізів. Ці рівняння трансцентдентні, тому розв'язуються наближенню. В рамках послідовних наближень вибрано метод, який забезпечує швидку збіжність процесу, а саме: метод скорішого спуску або градієнтний метод. Похибки параметрів обчислено за допомогою коваріаційної матриці. Статистична прийнятність моделі визначено за критерієм Фішера.

Результати. Чисельними розрахунками з експериментальних даних диференціальних перерізів пружного *pp*-розсіяння знайдено значення параметрів і масштабного множника амплітуди. За амплітудою в околі мінімумів обчислено диференціальні перерізи. Представлено відповідні графіки цих перерізів. Збіг з експериментом в більшості випадків задовільний, в окремих – якісний. Отримано коваріаційну матрицю, з якої знайдено похибки параметрів моделі. При загальних умовах виведено обмеження на знайдені наближені значення параметрів. Показано, що вони обмеженням задовольняють. За критерієм Фішера виконано перевірку статистичної прийнятності моделі, що виявилася позитивною

Висновки. Запропонована проста амплітуда забезпечує виконання обмеження Фруассара та унітарності. Вона служитиме як затравальна для побудови більш складних амплітуд, що описуватимуть широке коло експериментів протон-протонного й антипротон-протонного розсіянь за високих енергій

Ключові слова: амплітуда, параметр, дипольний померон, коваріаційна матриця

Scientific Herald of Uzhhorod University
Series “Physics”

Journal homepage: https://physics.uz.ua/en
Issue 51, 39-47
Received: 11.04.2022. Revised: 25.05.2022. Accepted: 15.06.2022

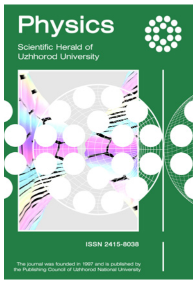

UDC 53.043, 532.5, 533.6.01, 533.16, 533.17
PACS 47.10.-g, 47.32.-y
DOI: 10.54919/2415-8038.2022.51.39-47

Effects of Repulsion and Attraction between Rotating Cylinders in Fluids

Vadym Ostanin*

Abstract

Relevance. From the theory of hydrodynamics, it is known about the interaction of a pair of vortices in inviscid fluids. The relevance of the study is conditioned upon the presence of many studies of numerical simulations of the interactions of two vortices or two cylinders, but the lack of research of practical installations for observing the effects of attraction and repulsion in fluid media may slow down research in this area for practical application.

Purpose. The purpose of this study is a practical demonstration of the possibility of the effect of double interaction in the air, with the calculation of the approximate magnitude of the force tending to attract or repel each of the cylinders.

Methods. In a practical experiment, a pair of plastic cylinders are used, which are driven by engines and rotate next to each other in the air at atmospheric pressure. Numerical simulation of the effect shows the nature of the effect and allows predicting the magnitude of the force generated by rotating cylinders on each other. The relationship between the directions of rotation of the cylinders and the observed effects was verified by numerical simulation using numerical simulation of finite volumes of OpenFOAM version 9.

Results. In a practical experiment, a pair of rotating cylinders started interacting at 5-7 cm in the experiment, which at a smaller distance of 2-3 cm created sufficient force to stabilise the vibrations of one of the cylinders around the thread for which it is suspended. Numerical simulation shows that a zone of high or low pressure is formed in the space between the cylinders, depending on the direction of rotation. The rotation of adjacent disks with opposite directions of rotation helps the circulation of the other cylinder to maintain the flow velocity in the gap, which reduces the fluid pressure between the rotating disks and attracts them. Conversely, rotating disks with the same direction extinguish and compress fluid flows in the gap, which increases the air pressure between rotating objects above the stationary pressure and repels them.

Conclusions. The results of the study provide a better understanding of the processes of fluid interaction, link the dependence of the interaction force on the parameters of the medium and cylinders, and demonstrate the practical possibility of applying the effects of interaction in fluid media

Keywords: interaction of circulations, fluid vortices, cylinder rotation, numerical simulation

Suggested Citation:
Ostanin V. Effects of repulsion and attraction between rotating cylinders in fluids. *Scientific Herald of Uzhhorod University. Series “Physics”*. 2022;(51):39-47.

*Corresponding author

Introduction

Inspired by the similarity of the effects of electromagnetism and rotating vortices [1; 2], and the presence of studies of vortices for water and air environments in the 19-20 centuries [3; 4], the author found most studies using only numerical simulations to describe vortices [5-7]. This paper describes a practical experiment of controlled attraction and repulsion of rotating objects in the air, shows the possibility of practical use of these interactions, and applies numerical simulation to determine the interaction forces using kinetic pressure values. The practical experiment was performed in an air stationary environment at atmospheric pressure. This effect can be a solution for the engineering problem of contactless interaction between objects, when electric or magnetic fields can adversely affect the engineering mission.

Materials and Methods

The equipment for the experiment (Fig. 1) involved two smooth plastic cylinders with a diameter of 50 mm and a length of 100 mm. They were driven by two independent motors from used hard drives, powered by a 12-volt DC source via controllers for brushless motors designed to consume no more than 1.5 amperes. One of the cylinders was suspended on a thin wire to the frame, and the second was in a free position for manipulating it with a hand. The suspended position of one of the cylinders was chosen to capture a weak effect. The wire was used instead of a thread to reduce the unwinding of the cylinder due to the properties of the thread to unwinding under tension. The air around the installation played the role of a viscous medium through which the cylinders interacted. The air was stationary with an atmospheric pressure of 769 mmHg and a temperature of 25°C. The geometric dimensions of the cylinders, the rotation speed, and the air conditions were used to calculate the Reynolds number (1) for practical experiment. When both engines were turned on, the cylinders were unwound to a stable speed of approximately revolutions per minute, which is equal to 26.2 m/s. The rotation speed was measured by a digital tachometer with an accuracy of 0.05%.

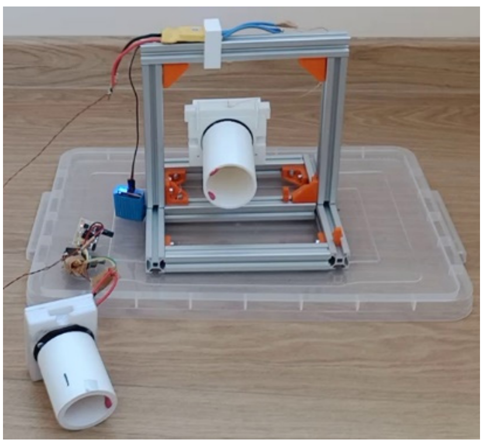

Figure 1. Experimental equipment

$$Re_{air_\varnothing} = \frac{\rho_{air}\Omega\mathcal{R}^2}{\eta_{air}} = \frac{1.185\times 1047\times 0.025^2}{15.6\times 10^{-6}} = 49{,}707 \quad (1)$$

where R_{cyl} is the radius of the cylinder = 0.025 m; L_{cyl} is the cylinder length = 0.1 m; Ω is the cylinder rotation speed = = 10^4 *RPM*=167 *RPS*= 1,047 rad/s; ρ_{air} is the air density at 25°C = 1.185 kg/m^3; μ_{air} is the kinematic viscosity [8] of air at 25°C =15.6×10^{-6} m^2/s; η_{air} is the dynamic viscosity of air = = $\rho_{air}\times\mu_{air}=18.3\times10^{-6}$ kg/(m×s).

Having put each cylinder into rotation (Fig. 2), a boundary layer of air would form on the rotating body of rotation due to the condition of adhesion to the surface of the body with the effect of "no slip condition", which means that at the boundary of a solid object, a viscous liquid flows at zero velocity relative to this boundary (Fig. 3). When each cylinder rotates, this creates a very thin "boundary layer" around the cylinder, the air next to the cylinder simply rotates with it at the same speed (Fig. 4). The cylinder literally drags air with it. And in the next layers, rotation in a viscous medium creates a vortex-free circulation of the flow in a circle around the cylinder.

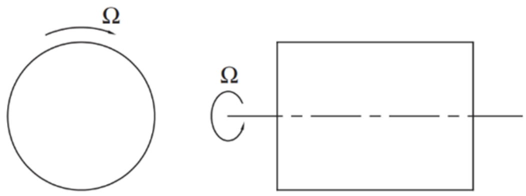

Figure 2. Geometry of the rotating cylinder
Source: [9]

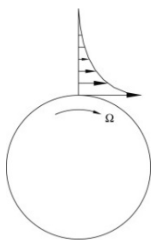

Figure 3. Boundary layer above the rotating disk
Source: [9]

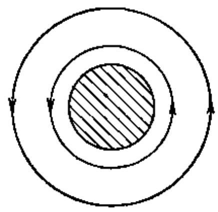

Figure 4. Circulation around the cylinder
Source: [9]

To confirm the causes of the observed effects, OpenFOAM version 9 numerical simulation software with the PISO algorithm was used. The results of calculations and graphs were obtained after a simulation lasting 40 seconds. The results of 4 simulations are presented in this paper. The difference between simulations is presented in Table 1.

Table 1. Boundary layer and environment parameters for different simulations in OpenFOAM9

Name	Boundary layer conditions in simulation of one of two cylinders (file 0.orig/U)	Parameters of kinematic viscosity and medium pressure (transportProperties file)
Attraction in the air	code #{ const fvPatch& boundaryPatch = patch(); const vectorField& Cf = boundaryPatch.Cf(); vectorField rot(Cf.size(), vector(0,0,0)); rot = -10000.0/60*6.28*vector(0,0,1)^(Cf-vector(0.075,0.0, 0.0)); operator==(rot); #};	transportModel Newtonian; nu nu [0 2 -1 0 0 0 0] 1.56e-05; rho rho [1 -3 0 0 0 0 0] 1.185;
Repulsion in the air	code #{ const fvPatch& boundaryPatch = patch(); const vectorField& Cf = boundaryPatch.Cf(); vectorField rot(Cf.size(), vector(0,0,0)); rot = 10000.0/60*6.28*vector(0,0,1)^(Cf-vector(0.075,0.0, 0.0)); operator==(rot); #};	transportModel Newtonian; nu nu [0 2 -1 0 0 0 0] 1.56e-05; rho rho [1 -3 0 0 0 0 0] 1.185;
Attraction in water	code #{ const fvPatch& boundaryPatch = patch(); const vectorField& Cf = boundaryPatch.Cf(); vectorField rot(Cf.size(), vector(0,0,0)); rot = -10000.0/60*6.28*vector(0,0,1)^(Cf-vector(0.075,0.0, 0.0)); operator==(rot); #};	transportModel Newtonian; nu nu [0 2 -1 0 0 0 0] 0.903e-06; rho rho [1 -3 0 0 0 0 0] 997.3;
Repulsion in water	code #{ const fvPatch& boundaryPatch = patch(); const vectorField& Cf = boundaryPatch.Cf(); vectorField rot(Cf.size(), vector(0,0,0)); rot = 10000.0/60*6.28*vector(0,0,1)^(Cf-vector(0.075,0.0, 0.0)); operator==(rot); #};	transportModel Newtonian; nu nu [0 2 -1 0 0 0 0] 0.903e-06; rho rho [1 -3 0 0 0 0 0] 997.3;

Results and Discussion

At the first start, the cylinder motors rotated in one direction, the manual cylinder was brought to the hanging cylinder and at about 7 cm or less, the hanging cylinder was repelled from the manual cylinder. The closer the hand cylinder approached, the more the hanging cylinder was repelled, and the force generated by the flows was sufficient to keep the hanging cylinder from meeting the hand cylinder, and not allow the hanging one to return to the equilibrium position of the stretched wire (Fig. 5).

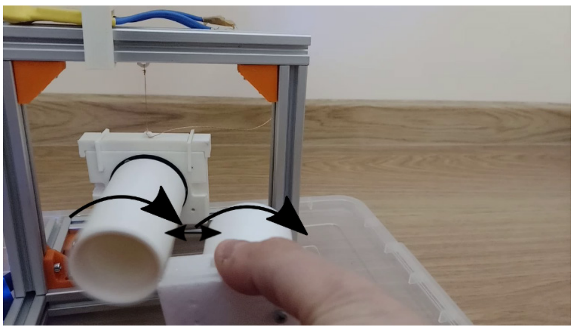

Figure 5. Demonstration of repulsion

Source: [9]

Changing the experimental conditions and rotating the cylinders in opposite directions, the manual cylinder was also brought to the hanging cylinder. Therewith, the attraction of the hanging cylinder to the manual cylinder was observed at a distance of 5 cm or less (Fig. 6). Not removing the manual cylinder in time often led to contact and unbalancing of the hanging cylinder.

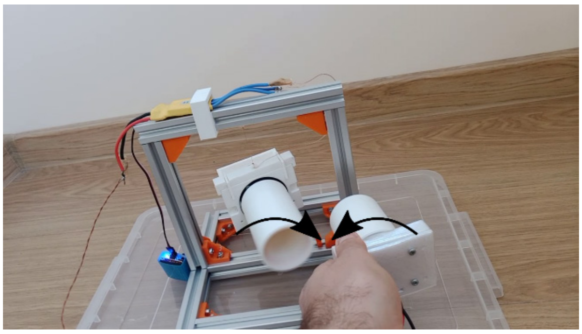

Figure 6. Demonstration of attraction

When the hanging cylinder was unbalanced, to perform several experiments in a row, it was necessary either to stop the hanging cylinder to balance it and start it slowly, or to slow down its rotation on the thread by repulsion or attraction in the air. This was achieved faster with mutual repulsion than with mutual attraction. The force of mutual attraction increased with the approaching, and without prompt removal of the manual cylinder, their collision led to an imbalance of the hanging cylinder. The high speed of rotation and the lack of support points did not allow reducing the distance between the cylinders less than 3 mm.

The vortices created by the cylinders are similar to vortices generated under the water column in streams with a negative longitudinal velocity gradient near the solid boundary [10]. A pair of natural vortices were unstable [11] and tended to unite with unidirectional rotation [12], and with the opposite rotation, destruction caused the development of the Crow instability, which leads to multiple curvatures of the vortices [13]. Similar processes and results were demonstrated by E. Dormy and H.K. Moffatt [14]. They describe the behaviour of medium flows in conditions of short distance, contact, and negative distance between two cylinders. At the point of contact, the total interaction force F, comprising viscosity forces, pressure forces and contact forces, is F_c zero.

Simulation of a single cylinder

As the velocity of the boundary layers increased, the viscous airflow flowed around the cylinder, forming separate vortex-free airflow circulations in the form of concentric circles [15; 16] (Fig. 7). With a sharp start of rotation of the cylinder, vortex flows may be observed at first, but after a few seconds the circulation became vortex-free. Viscous friction considerably affects the behaviour of the medium. Due to the forces of viscous friction, the circulation of fluid flows occurred around a rotating cylinder. In the boundary zone of the air and the cylinder, the pressure was the lowest due to the high flow velocity (2), which is consistent with the Bernoulli equation for viscous fluids:

$$P_1 + \rho g h_1 + \frac{\rho {v_1}^2}{2} = P_2 + \rho g h_2 + \frac{\rho v_2^2}{2} + h_L \qquad (2)$$

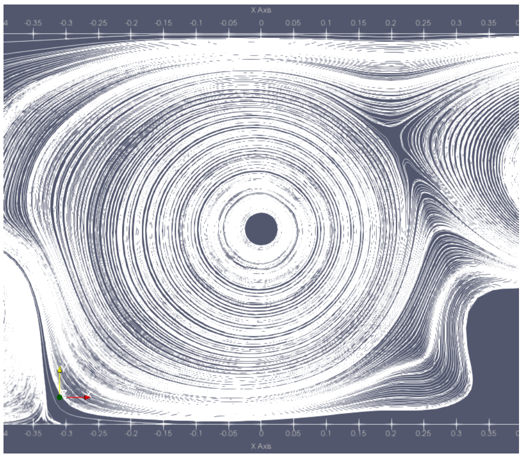

Figure 7. Circulation of one cylinder in a simulation with a rotation speed of 10^4 rpm

The velocity of fluid circulation around the cylinder is inversely proportional to the distance from the cylinder r^2 (3) (Fig. 8).

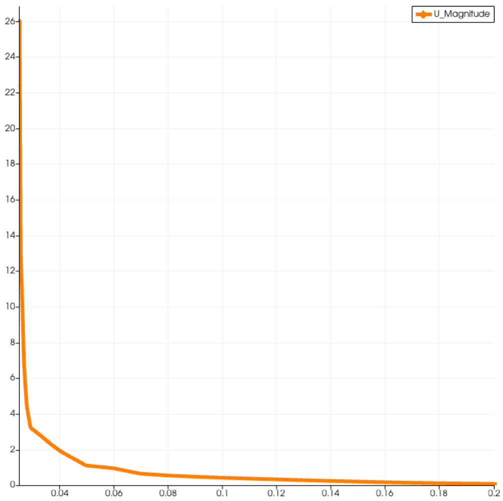

Figure 8. Distribution of the circulation velocity around one cylinder in the simulation at a speed of 10^4 rpm

$$U \sim \frac{1}{r^2} \qquad (3)$$

When rotating, the cylinder carries away the adjacent layers of air, causing its circulation. Vortex-free circulations of a viscous medium cover the entire space outside the cylinder, provided that the space around is boundless. But if the space is limited, e.g., by walls, then swirls occur near the walls. But the flow velocity in these vortices was much less than the main flow near the cylinder, so they were not considered in the observations of effects. The greater the viscous friction, the more stable the circulation, and the slower the circulation rate decreases, moving away from the cylinder. The velocity of the fluid flow was different at the walls and away from them. If one enters the transverse (perpendicular to the velocity vector) coordinate of the distance from the cylinder surface r, then the fluid velocity is a function of this distance v(r) (Fig. 6). This dependence is determined by the transmission of momentum in the transverse direction or otherwise by the velocity gradient, as in the case of a viscous gas (4):

$$J_p = -\eta \times \frac{dv}{dr} \quad (4)$$

The interaction force of adjacent layers touching on the surface S is equal to (5):

$$F = \eta \times \frac{dv}{dx} \times S \quad (5)$$

Moving away from the cylinders, the circulation rate decreases, keeping the pressure close to stationary, which is higher relative to the cylinder (Fig. 9).

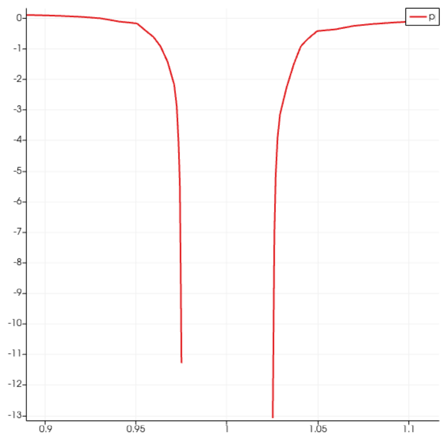

Figure 9. Distribution of kinematic pressure of one cylinder in the simulation

Preparation of the grid for simulation

In the area near the cylinder surface where higher accuracy is required, a fine mesh is used. Moving away from the surface, the mesh becomes rougher (Fig. 10).

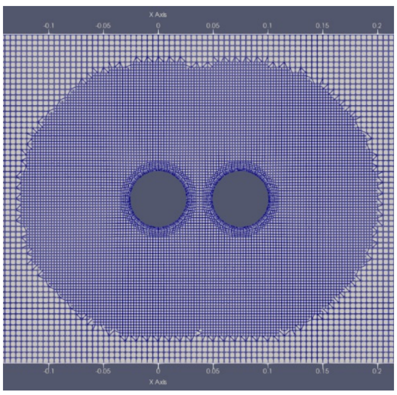

Figure 10. Computational grid

The effect of fluid attraction in the simulation

Two cylinders with a diameter of 0.05 meters at 0.025 meters from each other were configured to rotate in opposite directions, e.g., one cylinder was configured to rotate counterclockwise and the other one – clockwise. The flows converged between the cylinders, maintaining a circulation velocity greater than zero, and lowering the pressure between them (Fig. 11). The circulation rate of the fluid flow between the cylinders did not decrease to zero, it was maintained by the circulation of the adjacent cylinder (Fig. 12). The pressure difference $P_{outer}=P_1$ outside the cylinders and $P_{inner}=P_2$ between the cylinders created an attractive force acting on each cylinder separately, directed from the outside of each cylinder into the interior of the space between the cylinders (Fig. 13).

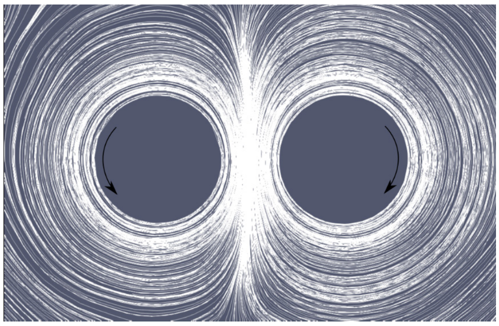

Figure 11. Tracing of airflow circulation in simulation with multidirectional rotation of the boundary layer of air

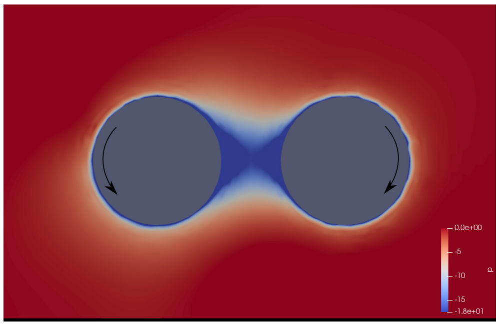

Figure 12. Distribution of airflow velocities in simulation with multidirectional rotation of the boundary layer of air

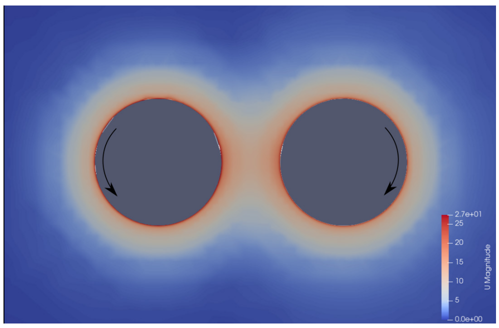

Figure 13. Distribution of air pressure in simulation with multidirectional rotation of the boundary layer of air

The force arising from the difference between external P_1 and internal pressure P_2 was calculated using the formula from the definition of pressure (6), and the pressure difference as (7) [12]:

$$P = \frac{F}{A} \quad (6)$$

$$\text{where } P = P_1 - P_2 = \triangle P_{12} \quad (7)$$

Then the force *F* is equal to the product of the pressure difference by the area of the surface experiencing pressure (8):

$$F = \triangle P_{12} A \quad (8)$$

The simulation results (Fig. 14b) demonstrate that the minimum pressure between the cylinders is (9):

$$\frac{P_2}{\rho} = -17\ {m^2}/{s^2} \rightarrow P_2 = -17\,{m^2}/{s^2} \times 1.185\ kg/m^3 = -\ 20.145\ Pa \quad (9)$$

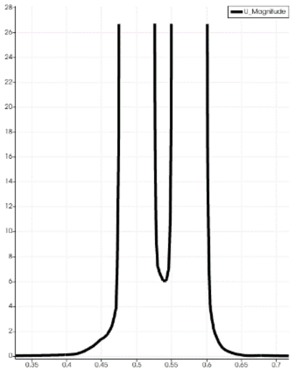

Figure 14a. Graph of airflow parameters near and between cylinders with multidirectional rotation of the boundary layer of air: Flow velocity

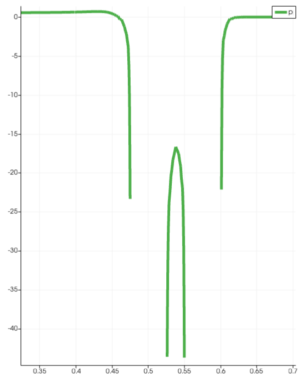

Figure 14b. Graph of airflow parameters near and between cylinders with multidirectional rotation of the boundary layer of air: Kinematic pressure

If one sets the pressure outside the cylinders to atmospheric stationary as P_1=0 Pa because numerical simulation sets the stationary pressure as 0 m²/s², where the velocity of the fluids is minuscule compared to the velocity of the cylinder itself, then the pressure difference (7) relative to atmospheric is (10):

$$\triangle P_{12} = 0 - (-20.145) = 20.145\ Pa \quad (10)$$

The contact area A of the external pressure towards the space between the cylinders is equal to half of the surface of the cylinder (11-12):

$$A = \frac{2\pi R_{cyl}}{2} * L_{cyl} \quad (11)$$

$$A = \frac{2 \times 3.1415 \times 0.025}{2} \times 0.1 = 0.00785375\ m^2 \quad (12)$$

Using the pressure difference $\triangle P_{12}$ (10) and the contact area *A* (12), the force $F_{air\_attract}$ is calculated as (13):

$$F_{air\_attract} = 20.145 \times 0.00785375 = 0.158\ H \quad (13)$$

Using the values (12; 18), the force F_{water} is calculated. For this, the authors of this study set P_1=0 Pa for water as well as for air, and the main characteristics of water at 25 as (14; 15; 16):

$$\rho_{water} = 997.3\ kg/m^3 \quad (14)$$

$$\mu_{water} = 0.903 \times 10^{-6}\ m^2/s \quad (15)$$

$$\eta_{water} = \rho_{water} \times \mu_{water} = 0.901 \times 10^{-3}\ kg/(m \times s) \quad (16)$$

The kinematic pressure between the cylinders was given from the graph (Fig. 15) and was reduced to a change in dynamic pressure (17; 18; 19).

$$\frac{P_2}{\rho} = -9.5\ {m^2}/{s^2} \quad (17)$$

$$P_2 = -9.5\,{m^2}/{s^2} \times 997.3\ {kg}/{m^3} = -9{,}474.4\ Pa \quad (18)$$

$$\triangle P_{12} = 0 - (-9{,}474.4) = 9{,}474.4\ Pa \quad (19)$$

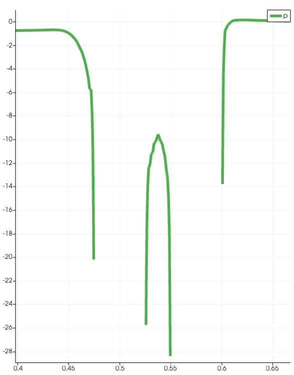

Figure 15. A graph of the kinematic pressure of the water flow near and between the cylinders in a simulation with a multidirectional rotation of the boundary layer of air

Using the dynamic pressure difference $\triangle P_{12}$ and the contact A area, the force $F_{water\_attract}$ is calculated as (20):

$$F_{water\_attract} = 9{,}474.4 \times 0.00785375 = 74.4\ H \quad (20)$$

A graph is given for a visual analysis of the difference in the rate of change of kinematic pressure for water and air in the interval between the cylinders with multidirectional rotation, from 0 to 3 seconds (Fig. 16).

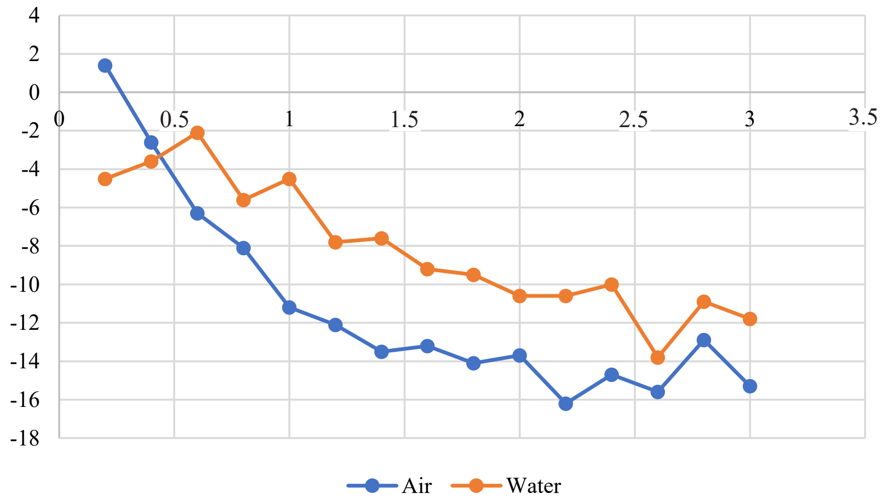

Figure 16. A graph of the pressure drop between the cylinders over time in a simulation with a multidirectional rotation of the boundary layer of air and water

The effect of fluid repulsion in the simulation

Both cylinders are configured to rotate in the same directions, e.g., one cylinder was configured to rotate counterclockwise, and the other one – clockwise. As the velocity increased, their boundary layers accelerated the airflow around each of them, forming separate airflows in the form of concentric circles. Bringing the cylinders closer as the velocity of the boundary layer increases, the airflows around the cylinders combine to form a single flow (Fig. 17). But not all the flow moved in a laminar fashion around the cylinders. The airflows at the boundary layer of the cylinder, pressed down by the external atmospheric pressure, were still trying to move around each of the cylinders. But trying to move between the cylinders, they met an oncoming flow from the neighbouring cylinder. This collision of flows stopped circulation in the centre and created excess pressure between the cylinders (Fig. 18). This excess pressure was greater than atmospheric pressure, and it enabled both cylinders to tend to push off from the zone between the cylinders. In addition, due to the collision of oncoming circulation flows, the flow velocity between the cylinder tended to zero (Fig. 19).

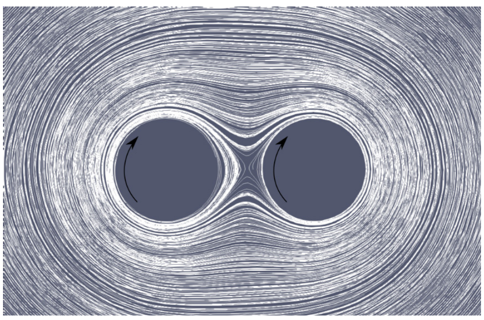

Figure 17. Tracing of airflow circulation in simulation with unidirectional rotation of the boundary layer of air

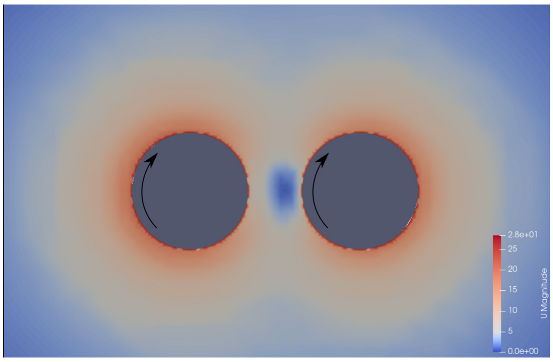

Figure 18. Distribution of airflow velocities in simulation with unidirectional rotation of the boundary layer of air

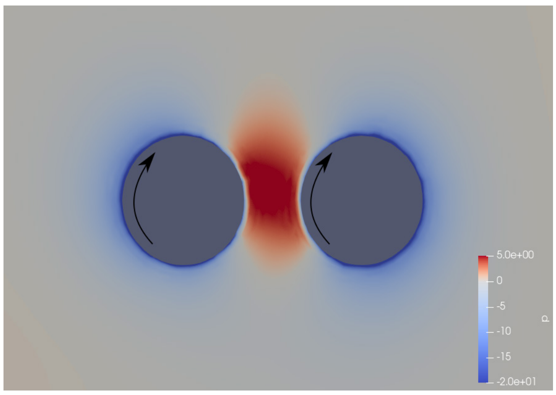

Figure 19. Distribution of air pressure in the simulation with unidirectional rotation of the boundary layer of air

Using formulas (7; 8; 11) and data from the graph (Fig. 20a, 20b), the dynamic pressure difference $\triangle P_{12air}$ $\triangle P_{12water}$ was calculated as (21; 22; 24; 25), and the repulsive forces were F_{air_repel} F_{water_repel} calculated as (23; 26):

$$\frac{P_{2\_air}}{\rho} = -5.5\ {m^2}/{s^2} \rightarrow P_{2\_air} = -5.5\,{m^2}/{s^2} \times 1.185\ kg/m^3 = -\ 6.5\ Pa \tag{21}$$

$$\triangle\, P_{12\_air} = 0 - (-6.5) = 6.5\ Pa \tag{22}$$

$$F_{air\_repel} = 6.5 \times 0.00785375 = 0.051\ H \tag{23}$$

$$\frac{P_{2\_water}}{\rho} = -6.5\ {m^2}/{s^2} \rightarrow P_{2_{water}} = -6.5\,{m^2}/{s^2} \times 997.3\ kg/m^3 = -\ 6{,}482.5\ Pa \tag{24}$$

$$\triangle\, P_{12_{water}} = 0 - (-6{,}482.5) = 6{,}482.5\ Pa \tag{25}$$

$$F_{water\_repel} = 6{,}482.5 \times 0.00785375 = 51\ H \tag{26}$$

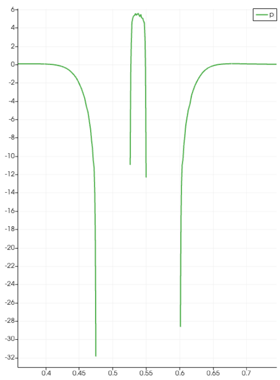

Figure 20a. A graph of the kinematic pressure of the flow near and between the cylinders in a simulation with unidirectional rotation of the boundary layer for air

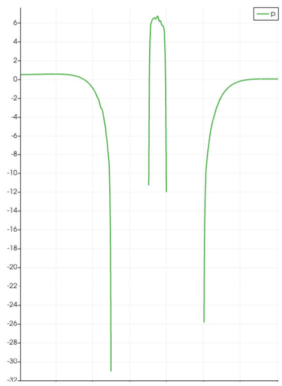

Figure 20b. A graph of the kinematic pressure of the flow near and between the cylinders in a simulation with unidirectional rotation of the boundary layer for water

Conclusions

The results obtained using numerical methods confirmed the presence of a pressure difference that causes the effects of attraction and repulsion in a fluid medium of two or more rotating cylinders. This study has proven that the effects are more pronounced in water compared to air. There is also a direct dependence of the force of interaction on the density of the medium, on the speed of rotation of the cylinders and the distance between the cylinders, which directly affect the difference between the pressure generated outside and inside between the cylinders. Kinetic viscosity affects the speed of pressure change. The lower the kinetic viscosity, the slower the molecules of the medium transmit momentum further away from the cylinders, and it will take longer to achieve the greatest pressure difference. Air has a higher kinematic viscosity, so it reaches its greatest pressure difference faster, and water is slower. But in water, due to the high density, a large force of interaction is achieved. Upon solving technical problems of contactless and non-magnetic interaction, an aqueous medium or an environment with a higher density is more suitable, which causes a greater force of effects.

The author of this paper sees the continuation of research in creating a model of magnet configurations, e.g., the Halbach array, in simulation, as well as a physical experiment with micromotors and cylinders to analyse the difference in the behaviour of magnetic field lines in the Halbach array and the cylinder assembly in the air.

References

[1] Hussain KTI, Jothi TJS. Vortex ring propagation and interactions studies. *S dhan* . 2018;(43):9. doi: 10.1007/s12046-018-0843-9.

[2] Watson EJ. The rotation of two circular cylinders in a viscous fluid. *Mathematika*. 1995;(42):105-26.

[3] Tanasheva TN, Nussupbekov BR, Dyusembaeva AN, Shuyushbayeva NN. (2019). Analysis of aerodynamic characteristics of two parallel rotating cylinders. *Technical Physics*. 2019;(64):947-9. doi: 10.1134/S1063784219070247.

[4] Hills CP. Flow patterns in a two-roll mill. *The Quarterly Journal of Mechanics and Applied Mathematics.* 2002;55(2):273-96. doi: 10.1093/qjmam/55.2.273.

[5] Price TJ, Mullin T, Kobine JJ. Numerical and experimental characterization of a family of two-roll-mill flows. *Proc Roy Soc.* 2002;459:117-35. doi: 10.1098/rspa.2002.1022.

[6] Ren H, Zhang GX, Guan HS. Three-dimensional numerical simulation of a vortex ring impinging on a circular cylinder. *Fluid Dyn. Res.* 2015;(47):025507. doi: 10.1088/0169-5983/47/2/025507.

[7] Dritschel DG. A general theory for two-dimensional vortex interactions. *J. Fluid Mech.* 1995;(293):269-303.

[8] Speight J. Rules of thumb for petroleum engineers. Kinematic Viscosity. Beverly: Scrivener Publishing; 2017. 755 p. doi: 10.1002/9781119403647.ch209.

[9] Childs PRN. Rotating Flow. Philadelphia: Elsevier Inc; 2011. 389 p.

[10] Melnykova ON. Channel flow dynamics. Moscow: Max Press; 2006. 133 p.

[11] Leweke T, Le Dizes S, Williamson CHK. Dynamics and instabilities of vortex pairs. *Annual Review of Fluid Mechanics*. 2016;(48):507-41. doi: 10.1146/annurev-fluid-122414-034558.

[12] Le Dizès S, Verga, A. Viscous interactions of two co-rotating vortices before merging. *Journal of Fluid Mechanics*. 2002;(467):389-410. doi: 10.1017/S0022112002001532.

[13] Johnson HG, Brion V, Jacquin L. Crow instability: Nonlinear response to the linear optimal perturbation. *Journal of Fluid Mechanics*. 2016;(795):652-70.

[14] Dormy E, Moffatt HK. Flow induced by the rotation of two circular cylinders in a viscous fluid. *Fluid Dynamics;* 2020. doi: 10.48550/arXiv.2008.04432.

[15] Gadzhiev DA, Gaifullin AM, Zubtsov AV. On vortex generation by a rotating cylinder. *Fluid Dynamics*. 2020;(55):965-81. doi: 10.1134/S0015462820080042.

[16] Armengol J, Calbó J, Pujol T, Roura P. Bernoulli correction to viscous losses. Radial flow between two parallel discs. *American Journal of Physics*. 2008;76(8):730.

Ефекти відштовхування і притягнення між обертовими циліндрами у флюїдах

Вадим Олексійович Останін

Анотація

Актуальність. З теорії гідродинаміки відомо про взаємодію пари вихорів у нев›язких флюїдах. Актуальність дослідження обумовлена наявністю досліджень численних симуляцій взаємодій двох вихорів або двох циліндрів, які не досліджують практичні установки для спостереження ефектів притягнення та відштовхування у флюїдних середовищах, що може гальмуати дослідження в цій області для практичного застосування.

Мета. Метою цього дослідження є практична демонстрація можливості ефекту подвійної взаємодії в повітрі з вирахуванням приблизної величини сили, яка намагається притягнути або відштовхнути циліндри.

Методи. У практичному експерименті використовується пара пластикових циліндрів, які приводяться в рух двигунами і обертаються один поруч з іншим у повітрі при атмосферному тиску. Числове моделювання ефекту показує природу ефекту і дозволяє передбачити величину сили, створюваної циліндрами, що обертаються один до одного. Зв’язок між напрямками обертання циліндрів і спостережуваними ефектами було перевірено численним розрахунком за допомогою численного моделювання конечних об›ємів у OpenFOAM версії 9.

Результати. У практичному експерименті пара циліндрів, що обертаються починала взаємодію на відстані 5–7 см, та за відстані 2–3 см створювало достатню силу, аби стабілізувати коливання одного з циліндрів навколо нитки, за яку він підвішений. Численна симуляція показує, що в просторі циліндрами утворюється зона високого або низького тиску в залежності від напрямку обертання. Обертання сусідніх дисків з протилежними напрямками руху допомагає циркуляції іншого циліндра підтримувати швидкість потоку в зазорі, що знижує тиск рідини між циліндрами і притягує їх. І навпаки, циліндри, що обертаються в одному напрямку гасять і стискають рідинні потоки в шпарині, що збільшує тиск повітря між циліндрами, що обертаються, вище стаціонарного тиску і відштовхує їх.

Висновки. Результати дають можливість детальніше розуміти процеси флюїдної взаємодії, досліджувати залежність сили від впливу середовища та циліндрів і показують параметри практичної можливості застосування ефектів взаємодії в рідинних середовищах

Ключові слова: взаємодія циркуляції, флюїдні вихори, обертання циліндрів, численна симуляція

Scientific Herald of Uzhhorod University
Series “Physics”

Journal homepage: https://physics.uz.ua/en
Issue 51, 48-58
Received: 21.03.2022. Revised: 05.05.2022. Accepted: 26.05.2022

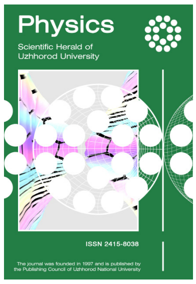

UDC 535.3
PACS 42.65.Wi
DOI: 10.54919/2415-8038.2022.51.48-58

Isothermal Transformations in High-Strength Cast Iron

Ramiz Hasanli*, **Ilham Aliyev, Nizami Poladov, Lala Azimova, Taleh Tagiyev**

Azerbaijan Technical University
AZ1073, 25 H. Javid Ave., Baku, Republic of Azerbaijan

Abstract

Relevance. The technological process of manufacturing parts from high-strength cast irons is simpler and more economical than the process of manufacturing parts from steel. Cast irons are less sensitive to stress concentrators and strike loads. Spheroidal graphite cast irons can achieve DI 70 grades even in the cast state. Through hardening heat treatment or additional alloying, it is possible to produce cast irons of higher strength (grades DI 80 and above). As the strength properties of cast irons increase, disadvantages in the form of low ductility and plasticity become increasingly apparent. These problems can be compensated by providing an ausferritic, bainite or bainite-austenitic structure of the metal matrix of cast irons. A good solution is to obtain cast irons with a complex structure of the bainite-ausferrite type. In this regard, the relevance of this work is due to the fact that, in the practice of modern mechanical engineering, high-strength cast irons are increasingly used.

Purpose. The purpose of this work is to study and obtain the bainite structure due to isothermal hardening. To achieve which specific features of isothermal transformation in high-strength cast iron with spheroidal graphite have been considered.

Methods. This research was based on a theoretical method (analysis, synthesis, concretization, generalization, modeling), and empirical methods (study of research experimental works of scientists and their experience in this or similar field with the application of similar designs and study by experienced specialists).

Results. The possibility and efficiency of obtaining the bainite structure in economically alloyed nickel, copper and molybdenum, in the amounts, respectively, of 1.0; 0.5 and 0.5%, of cast irons using continuous cooling in air has been established.

Conclusions. The results and conclusions formulated on their basis can be used in the future as an effective scientific basis for studying the prospects of application of isothermal hardening of alloyed and unalloyed high-strength spheroidal graphite cast irons

Keywords: ausferritic cast iron, isothermal hardening, spheroidal graphite cast iron, bainite, austenitization

Suggested Citation:
Hasanli R, Aliyev I, Poladov N, Azimova L, Tagiyev T. Isothermal transformations in high-strength cast iron. *Scientific Herald of Uzhhorod University. Series “Physics”.* 2022;(51):48-58.

*Corresponding author

Introduction

With the creation of eco-friendly technologies, including resource-saving technologies, the development of mechanical engineering is gaining a rapid pace. Such technologies make it possible to significantly increase the performance as well as the mechanical properties of castings, thereby reducing their metal consumption and dimensional accuracy. After high-strength cast iron with spheroidal graphite shape isothermal hardening, it becomes the optimal material for manufacturing parts used in abrasive and shock-abrasive wear conditions. In alloyed cast irons the processes of structure formation are characterized by increased sensitivity to kinetic factors. Castings from high quality cast irons, form a cast structure. This is primarily due to the crystallization process and the occurrence of conditions that determine the nature of the primary phases formed. After all, the nature of distribution, shape and number of phases depends on the chemical composition, factors of iron production in metallurgy. In the melt, under conditions of deep supercooling and oversaturation with carbon, the "nucleation" (i.e. inclusion) of graphite occurs. In turn, during eutectic crystallization of high-strength cast iron, the graphite phase develops around austenite and produces an equiaxed form of eutectic graphite inclusions. This is mainly due to the course of diffusion processes. Stress concentrators to some extent accelerate the nucleation and development of cracks, which is fraught with the destruction of the part. Such inclusions can occur in castings made of alloyed high-strength cast irons, due to the high chemical activity of the alloying elements. Casting defects or any other nonmetallic inclusions other than concentrators can also occur.

In order to obtain homogeneous austenite, the castings are heated to the critical region and held to form homogenization, which is the first stage of heat treatment. Considering the initial structure of the iron base and its chemical composition, the austenitizing temperature and holding time are selected. Ferrit, which is in large quantities in the initial matrix structure, does not allow at hardening temperatures to achieve the desired saturation (at 0.6-0.7% carbon, C) of austenite, as reported in two papers by J. Hernando et al. [1; 2], where the microstructure of austenite was investigated. As a result, the austenite is less resistant and the start of its decomposition in isothermal conditions decreases in the data of the incubation period. In order to dissolve carbides and homogenize austenite, provided there are free carbides or cementite at least in small amounts, it is necessary to increase the dwell time and quenching temperature. H. Hu et al. [3] reported that the decomposition of austenite during isothermal hardening accelerates with complete dissolution of carbides, other particles and stabilization of austenite, which can be achieved with prolonged holding time in the range of 950°C and above. However, significant heating during austenitization can lead to an increase in the austenitic grain, which implies a decrease in ductile properties. But at the same time, there is an enrichment of residual austenite and a decrease in the diffusion time. For example, in the work of S. Hasan et al. [4] reported that the amount of spherical graphite and the degree of spherules, affect the properties of bainite cast iron, the increase in the number of inclusions as a result gives a uniform fine-grained structure of the input iron, and consequently an increase in its mechanical abilities.

The size of graphite inclusions directly affects the rate of reaching the equilibrium state of cast iron, the larger they are, the longer it takes to reach this state, and, in turn, the rate of dissolution of these inclusions, is a diffusion process. Using the diagrams of isothermal transformation of supercooled austenite, and taking into account the chemical composition of cast iron, determine the holding time and the choice of cooling rate to the temperature of isothermal transformation. The duration of isothermal soaking and temperature, have the greatest influence on the structure of the metal base and, in particular, on its formation. Isothermal soaking determines the dispersity of the matrix as well as the completeness of the decomposition of austenite. The structure and phase composition of austenite decomposition products are quite complex. The shape of bainite changes with decreasing temperature, from porous (upper bainite), to needle-like (lower bainite). Always when quenching to bainite, the structure contains residual austenite. As the isothermal holding temperature increases, the residual austenite content will increase. The impact toughness and ductility have a fairly wide range of changes depending on the duration of holding during isothermal processing, but the strength properties are not greatly affected. Austenite cannot turn into bainite if there is insufficient holding time and upon further cooling, it turns into martensite, which has low ductility but high strength. Generally, because of the high silica content, carbide formation usually does not occur. In the work of M. Soliman & H. Palkowski [5] investigated the properties of martensitic-ferritic steels, where the results show that the ideal combination of ductility and strength characteristics, it is considered the complete transformation of austenite into bainite and the absence of martensite in the base.

Materials and Methods

This research, fundamentally studied work was based on a qualitative, reliable combination of proven theoretical methods (analysis, synthesis, concretization, generalization, modeling), and empirical methods (study of research experimental works of scientists and their experience in this or similar field with the application of similar designs and study by experienced specialists). The theoretical basis of this scientific work is mainly thematic studies consisting of scientific, research and review scientific articles, which include experimental methods and descriptions of experiments. Analyses, statistics and other types of works of researchers, taken from official sources with reliable information, aimed at the study of a large number of problematic issues that may appear during the application of the highlighted methods related to isothermal hardening of cast iron with spheroidal graphite.

At the first stage of scientific research its basic theoretical basis was prepared, on the analysis of which the basis for further conclusions is built. At this stage of scientific research the search and analysis of various reliable sources of information was performed. A large number of information resources devoted to increasing the strength of cast iron with spheroidal graphite using isothermal processes were reviewed and filtered. The collected data were reviewed and systematized for a simplified, quick and qualitative understanding of the information. A systematic analysis of the work and evaluation of tmethods of obtaining bainite structure in cast irons with spheroidal graphite was made and other ways of increasing the strength grade of cast irons were investigated. The main questions that can be effectively and qualitatively solved with the help of practical use of modern methods and technologies are outlined.

At the second stage, authors solved the problem of determining the possibility of obtaining the bainite structure in nickel, copper, and molybdenum-alloyed ductile cast irons using continuous cooling in air. Heating temperatures from 870 to 930°C were chosen. The results also show microphotographs for each temperature interval.

At the next stage of scientific research, an analytical comparison and in-depth study of the materials of the studied works was performed. Most of them included analyses, theoretical information and descriptions of the experience of various methods of improving the quality of cast irons and steels. Experiments by scientists on the topics of austenitization and martensitization of metals, as well as the production of nanobainite steels, their advantages and peculiarities, were analyzed in detail. The peculiarities of bainite transformation in graphitized cast irons, study of structure, mechanical and operational properties of cast irons were studied. The conclusions obtained as a result of research works were analyzed, specified and verified.

At the last stage, materials were completed, theoretical and practical conclusions were specified, and the data obtained were generalized, checked, and systematized. The results and conclusions formulated on their basis can be used in the future as an effective scientific basis for studying the prospects of application of isothermal hardening of alloyed and unalloyed high-strength cast irons with spheroidal graphite.

Results

This study considers the peculiarities of isothermal transformation in high-strength cast iron with spheroidal graphite. The possibility and efficiency of obtaining bainite structure in economically – alloyed with nickel, copper and molybdenum high-strength cast irons with spheroidal graphite cast in a metal mold by continuous cooling in air has been established. According to the standard technology, some parts of shut-off devices, including the slide valve, made of 40X steel, should be subjected to extensive hardening or normalization followed by nitriding to ensure high wear resistance and durability. This treatment is not suitable for cast iron. It is dangerous to subject cast iron parts to bulk hardening because of the possibility of cracking. Nitriding is also inadvisable because of the considerable duration of the process and the brittleness of the resulting layer. High durability of parts made of economically alloyed cast iron can be ensured by obtaining bainite structure in it by means of isothermal treatment or by some other method. It is known that a material with such a structure is not inferior to nitrided cast iron in terms of wear resistance, because the highest wear resistance belongs to cast irons with a bottom bainite structure, while the strength of isothermally hardened cast irons is at a high level.

Many works are currently devoted to the study of methods for obtaining bainite iron. For example, one of them is the creation of a bainite matrix in cast iron. However, this method is complicated, requires the use of significant complex alloying additives and does not guarantee a homogeneous structure due to liquation and micro-liquation of the elements in the cast iron that develop during crystallization. For ductile cast irons, this method is even more unacceptable, since they must necessarily undergo graphitizing annealing. Therefore, isothermal hardening is a more expedient method for these conditions for obtaining the bainite structure in cast iron. It makes it possible to form bainite without pearlite inclusions and structurally free ferrite. It makes it possible to form bainite without pearlite inclusions and structurally free ferrite. At the same time this method requires special equipment and additional production area for placing hardening tubs, the use of scarce alkalis as hardening media. The complexity of the method also consists in the difficulty of ensuring the temperature constancy of the tubs, which is associated with high energy costs.

For cast irons, especially those alloyed with nickel, copper and molybdenum, in amounts of 1.0; 0.5 and 0.5%, respectively, it seems possible to obtain a bainite metal base during continuous cooling. The alloying additives should help to increase the stability of austenite in the pearlitic area. It is necessary to check whether it is possible to obtain the bainite structure in cast iron alloyed with nickel, copper and molybdenum under conditions of continuous cooling, what sizes of additives are required in this case, how homogeneous is the resulting structure and what level of properties can be ensured as a result of such treatment. After all, the presence of structural heterogeneity, as well as differences in the ratio of phases in the matrix can significantly affect the mechanical properties of the alloys under study. It is necessary to assess the degree of influence of these factors on the level of guaranteed properties of cast irons. Therefore, this work solved the problem of establishing the possibility of obtaining the bainite structure in nickel-, copper-, and molybdenum-doped ductile cast irons using continuous cooling in air.

Such a treatment can be performed with heating above and beyond. It does not seem to make sense to conduct heating in the intercritical region, since this can lead to strengthening the already strongly developed heterogeneity in the iron matrix. In addition, it is important to ensure the stability of pre-cooled austenite in the area of pearlitic decomposition, and this will be more fully achieved after heating higher. For this reason, heating temperatures from 870 to 930°C were chosen for the study. The heat treatment uses tightly controlled temperature modulation to improve certain wanted characteristics of the metals, such as performance and durability. Isothermal hardening is a heat treatment process designed for the treatment of metals with medium to high carbon content. The main purpose of isothermal hardening is to reduce deformation while increasing the strength and toughness of the metal. This is done by heating the product until the metal becomes austenitic and then hardening to precise temperatures and leaving it there for intervals of time.

Alloyed and, for comparison, unalloyed spheroidal graphite high-strength cast irons were subjected to isothermal hardening. The structure of bainite depending on the temperature of isothermal aging was studied on unalloyed cast iron samples. At the same time, the aim was to establish the connection between the initial structure of the matrix and the rate and completeness of the bainite transformation. The last is important in the development of production technology. The austenitizing temperature was 910°C, which is 50°C higher for the alloy under study. The holding time was 15 min, isotherm temperatures: 350, 400 and 450°C. During hardening, ferritic and pearlitic iron samples were subjected to the same heating in the furnace and simultaneously transferred to the tub. Exposures in the tub ranged from 30 s to 20 h. After isothermal soaking the samples were cooled in water. At low dwellings in the tub the cast iron acquired high hardness. This was due to the presence of a significant amount of martensite formed during precooling of the samples from the isothermal temperature in water. The bainite transformation in ferrite cast iron develops slower in the beginning than in pearlitic cast iron, as evidenced by their high hardness. The results obtained are shown in Table 1.

Table 1. Hardness of ductile iron with nodular graphite after isothermal quenching

Isothermal hardening temperature, ⁰C														
450					400					350				
Cooling time of cast iron ($\tau_{isot.}$)														
30s	50s	100s	16m	2h	60s	90s	10m	16m	2h	90s	120s	10m	16m	2h
Initial structure of cast iron (hardness, HB):														
pearlitic														
512	444	340	321	–	–	387	375	321	–	425	402	364	351	351
ferritic														
512	512	512	–	248	496	496	283	241	187	532	512	340	283	–

Source: [6]

The bainite transformation starts to develop intensively in cast irons with a ferritic initial structure after more than 10 minutes of holding. At temperatures of 400 and 350°C it practically ends in 15-16 minutes, the obtained microphotographs are shown in Figure 1. Cooling in the tub at 350°C leads to the formation of the lower bainite (Figs. 1; 2), at 400 and 450°C to the upper bainite. In the structure of the samples treated at 450°C, with dwell times of more than 16 min. In Figures 3-5 it can be clearly seaw the small isolations of carbides.

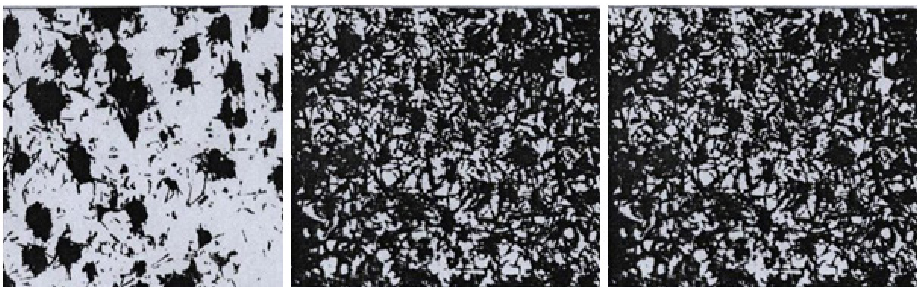

Figure 1. Microphotographs of bainite formation

Source: [6]

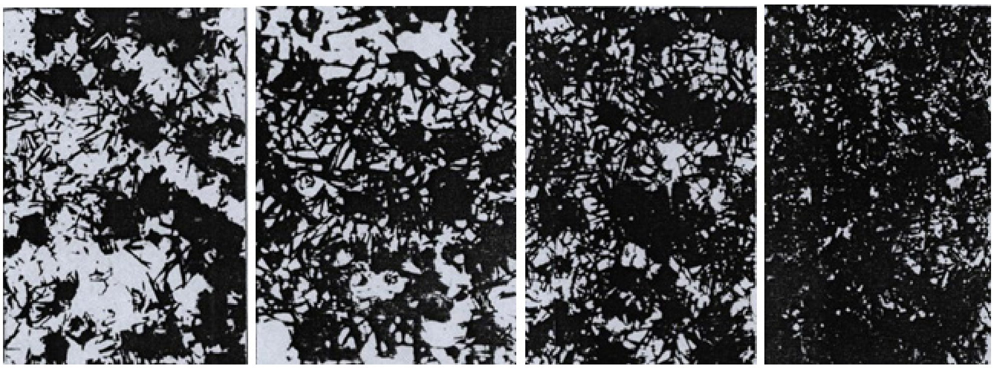

Figure 2. Micrographs of bainite formation

Source: [6]

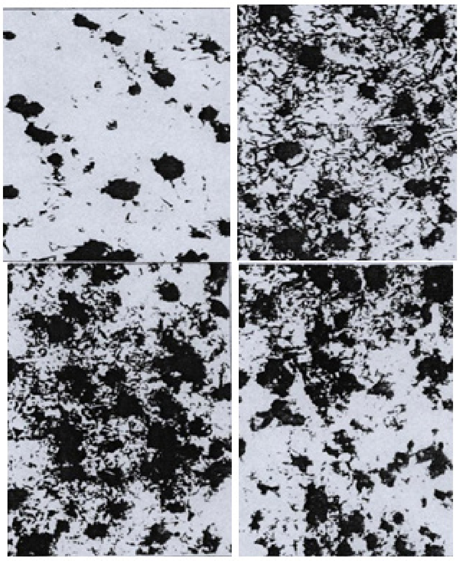

Figure 3. Microphotographs of carbide isolation

Source: [6]

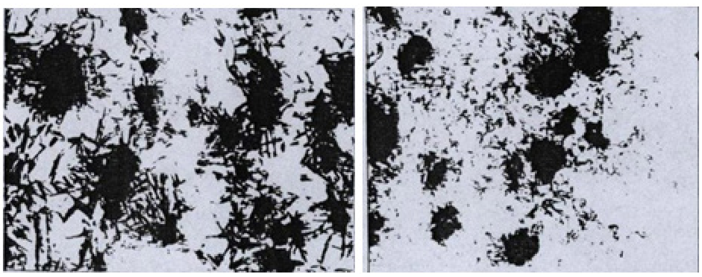

Figure 4. Microphotographs of carbide isolation

Source: [6]

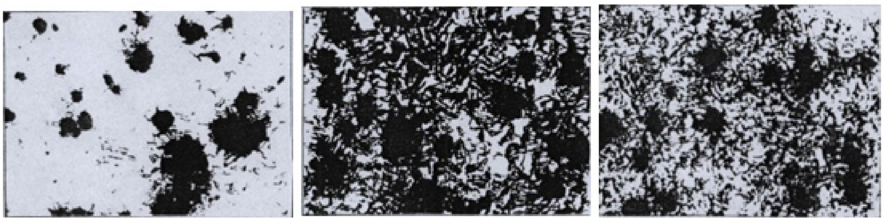

Figure 5. Microphotographs of carbide isolation

Source: [6]

The isothermal hardening process hardens medium- and high-carbon iron alloys, as well as carbon steel, by heating the metal to a temperature that breaks down its crystal structure until it becomes austenitic. Once the work becomes austenitic, the processes of martensitization or austenitization diverge into martensitization and austenitization.

Martensitization:

– to prevent austenite from turning into bainite or pearlite, this piece is quickly and successively hardened;

– having reached a homogeneous temperature of the material in front of the initial temperature of formation of martenite, the transition to the last step follows;

– air cooling to room temperature.

Austenitizing:

– having converted to austenite, the next step is to harden this piece to a temperature just above the temperature at which bainite begins to form;

– to turn austenite into bainite, the part must be kept at the required temperature for a while;

– finally, the piece is air-cooled or hardened in water.

Austenitizing and martensitizing have a wide range of advantages for many industries. The main ones are:

– increased strength. The crystalline structure of martensite or bainite, after isothermal hardening significantly hardens the metals, unlike untreated metals.

– impact strength. Where untreated metals can tear or crack, austenitic components are likely to withstand impact while retaining their shape. Hardened metals have this property because of their exceptionally strong crystalline structure.

– reductionn of distortion. They show less deformation compared to untreated steel because of the ductility acquired during the hardening process. For thin components, which need to maintain their dimensions during and after treatment in this way, this is a particularly useful property.

The main differences between austenitic and martensitic hardening:

1. Achievable hardness:

– martensitization – Rockwell hardness up to c65;

– austenitizing – Rockwell hardness up to c35-54.

2. Physical properties:

– martensitization – high strength, good impact toughness;

– austenitization – high strength, highest impact toughness.

3. Distortion control:

– martensitization – very good;

– austenitizing – excellent.

For example, a carburized gear wheel with a required Rockwell hardness of c 61-62 that is outside the austenitic tempering range should be subjected to martensitic tempering. A lawn mower blade requiring a Rockwell hardness of 46-48 should be austenitized to give it greater hardness to resist dents in use. Austempering is a special type of heat treatment in which austenite is converted to lower bainite. Generally, in conventional heat treatment, the austenitic structure turns into pearlitic or martensitic structure during continuous cooling methods. The process proceeds as follows: Heating the steel above the austenitizing temperature, hardening in a tub (usually a salt tank) at a constant temperature above the temperature of the particular steel (200-400°C), waiting in the tub until the bainite transformation is complete and finally cooling the steel part to room temperature with air or any other preferred method. In the literature, the austenitizing process is sometimes referred to as isothermal hardening or because of the isothermal heating mode of the process.

Tempering tubs play a crucial role in the austenitic tempering process, since maintaining the same temperature for a period of time is the basis of this heat treatment. However, because of the relatively high tub temperatures, oils are not a suitable hardening medium for this process. Instead, various molten salts are used in these tubs. Salt tub furnaces are pot-type furnaces that contain mixtures of salts with low melting points that are heated/melted by a pair of electrodes. They can also be used for numerous heat treatment processes such as liquid carburizing, cyaniding, liquid nitriding, martensitic tempering and austenitic tempering. It is not as eco-friendly due to the formation of gaseous products in the process, but it provides efficient and consistent heating of metal parts.

There are many variations in the chemical composition of the salt tub. In general, the use of molten salt tubs with nitrate/nitrite is common practice for the austenitic tempering heat treatment process. If we heat steel or cast iron until its constituents are converted to solution, then harden to 1200°F and hold at that temperature long enough, we will cause that microstructure to turn into the softest microstructure, perlite. If instead we had cooled this austenite to 600°F before aging, we would have avoided the pearlite transformation and instead created a much harder microstructure, bainite. Finally, if we cool this metal billet quickly and sufficiently, the formation of both pearlite and bainite would be eliminated, turning into the hardest structure, martensite. The studies conducted and the results obtained have established that the initial structure of the metallic base of ductile cast irons has a significant influence on the kinetic parameters of the bainite transformation. In the ferritic initial matrix the transformation proceeds faster and more completely than in the pearlitic one. However, the incubation period in ferritic cast iron is longer.

Discussion

With its good tribological properties and low cost, cast iron is a fairly current material, but the lack of the required mechanical properties leads to the fact that its main areas of application have become those in which the combination of heat and material wear plays a key role, for example in piston ring and liner cylinder systems. To reduce weight and save energy, it is necessary to improve the tribological and mechanical properties of cast iron, which, in turn, can be achieved by improving its microstructure, for which many studies have been conducted to improve its microstructure. With excellent thermal conductivity and an excellent endurance limit, compacted graphite cast iron is an excellent substitute for gray cast iron, for example in piston rings or cylinder liners. Thanks to the coral-like morphology of the graphite particles between ductile and nodular forms, such an excellent combination of tribological, physical and mechanical properties has been achieved in compacted graphite cast iron.

Laser hardening techniques by V. Writzl et al. [7], addition of stabilizing pearlitic elements Y. Lyu [8], surface alloying by J.J. Feng et al. [9] and induction hardening by T. Slatter et al. [10], have become an excellent solution for improving the wear resistance of cast iron with compacted graphite. Another way to improve mechanical properties is through austenitic tempering heat treatment. Several studies have shown a significant effect of the microstructure on improving the wear resistance of compacted graphite iron (CGI) after hardening, especially felt differences in comparison with pearlitic metal matrix under dry sliding conditions A.R. Ghaderi et al. [11], R. Ghasemi et al. [12] studied the austenitic tempering parameters of CGI ferritic cast iron and noticed a strong influence of temperature on the microstructure: at 275°C less ausferrite transformation was observed, in turn, when austenitizing was performed at 375°C, the final ausferrite was large due to higher carbon diffusion rate. Also in these studies, the authors showed little effect of processing time, summarizing that only at times up to 120 minutes did hardness increase slightly due to the emergence of carbides.

Isothermal ductile iron is produced by heat treatment of ferritic ductile iron without the addition of costly alloying elements. In terms of efficiency and economy, isothermal ductile iron is an extremely suitable solution for the production of very large parts requiring a high level of static and fatigue strength, such as pump heads for hydraulic systems, knuckles and axle center housings. isothermal ductile iron has higher performance than nodular cast iron and is more affordable than austenitic ductile iron, the benefits of which we will be discussd next. As reported in Dg. Eiken et al. [13], the matrix structure of isothermal ductile iron consists mainly of ferrite and pearlite, two elements which, due to a different distribution compared to conventional ductile cast irons, increase the mechanical characteristics of the finished castings. Therefore, isothermal ductile iron is a worthy alternative. With machinability comparable to that of perlitic ductile irons commonly used in machine shops, isothermal ductile iron is also suitable for machining. It has a mixed ferrite-pearlite structure, which means that it can also be surface hardened only where necessary, thus increasing the wear resistance of the parts. The advantages of isothermal ductile iron include:

– lightness: the specific weight of isothermal ductile iron is 10% lower than that of steel, which allows vehicles to either increase their maximum load or reduce fuel consumption;

– complex shapes: thanks to the melting technology and excellent casting ability the material can be applied only where it is necessary;

– fatigue strength: comparable in characteristics to pearlitic ductile cast irons;

– economical: no alloying elements are required

– elasticity: even at temperatures below 0°C (down to -40°C) the material guarantees stable mechanical characteristics in very thick castings or parts with variable thicknesses.

Two well-known tempering methods use isothermal hardening and martensitization. These two processes have much in common, their main differences being in the temperatures to which they are hardened, the time they remain at those temperatures, and the end result. To fully understand these processes, it is worth using the C-shape curve. During heat treating, the microstructure of the workpiece is transformed to produce the desired properties. C-curves are important for the metallurgist to understand when certain transformations occur in the metal and at what temperatures. The austenitic metal is stronger, more ductile, more impact resistant, and less prone to deformation. As reported in M. Rahaman et al. [14], martensitization quickly and effectively quenches austenite to avoid the formation of pearlite or bainite, resulting in the hardest microstructure, martensite. Examples of the major benefits of the austenitizing process are higher ductility and toughness at high hardness values, lower internal stresses and improved fatigue properties. For example, in A.I. Belyakov et al. [15] the authors show a number of advantages that it has in comparison with conventional hardened and tempered steels. Austenitizing also cools quickly, but not as low as martensitic hardening, because perlite formation is avoided and the temperature is maintained in the hardening until the billet becomes completely bainite. Typically, this process is used to create thin, yet strong ductile iron or carbon steel components. Common austenitized components include:

– agricultural machinery components;
– automotive transmission gears;
– construction machinery components;
– cutting blades;
– weapon parts;
– clips;
– clips, seat belts in automobiles.

The material after martensitizing has the highest Rockwell rating of any hardening process. This process is used to give parts the properties of minimal deformation. For example, in large parts of the aircraft industry. Some typical hardened parts include: crankshafts; gears; parts of industrial equipment; helicopter props. Common materials with isothermal hardening include: carbon steels, iron and alloy steels. These materials are the most hardenable with these methods because of the large amount of carbon they contain, which facilitates the transformation at different temperatures.

A significant limitation of austenitic tempering heat treatment is that it can only be applied to relatively thin cuts because of the requirements for uniform heating and temperature. In addition, the austenitic-perlitic transformation of a particular alloy must be relatively slow and the bainite temperature must be within reasonable limits when considering the tempering process from an economic point of view, mainly the energy consumption during tempering. A study of the effect of deformation temperature on phase transformations and microstructure in nanostructured bainite steel indicates that deformed austenite with deformation 0.3 at 300°C demonstrates accelerated kinetics of bainite transformation. However, the amount of bainite in preformed austenite then decreases as the deformation temperature increases. In deformed austenite, a critical deformation temperature can be detected that determines the possibility of bainite transformation. In addition, the thickness of the bainite plate in deformed austenite decreases with decreasing ausforming temperature. The lower ausforming temperature contributes to the more severe phenomenon of cross-growth of bainite plates. For these reasons, low-carbon steels are not suitable unless they are carburized. Examples of alloys suitable for austenitic tempering include the following groups of alloys: Spring steels (e.g., 50CrV4), smooth medium/high carbon steels, chromium molybdenum steels (AISI 4140), tool steels (e.g., H13) and boron steels (e.g., 94B30). Hardening of cast iron. Austenitizing iron is a heat treatment process that produces an ausferritic matrix. This heat treatment process is usually carried out using these stages:

– the austenitizing of castings usually takes place at temperatures of 850-950°C for between 15 minutes and 2 hours, long enough to saturate the austenite with carbon;
– rapid hardening to avoid the formation of pearlite in a hot salt bath at 250-450°C (lower than pearlite but higher than the beginning of martensite);
– isothermal aging in a hot salt tub, for sufficient time (usually 0.5 to 3 hours) to obtain an ausferritic matrix, a combination of needle ferrite and high-carbon austenite.

The factors controlling the cooling process to room temperature after a given hardening time can vary depending on the required mechanical properties (different microstructure), so there are different types of austenitic iron. Here are the best known of them and their typical uses:

– high-strength cast iron with austenitic tempering;
– the best known and most used technique;
– hardened gray iron;
– used to make quieter parts (excellent damping effect);
– bearing shells;
– brake components;
– carbide austenitic ductile iron;
– wear resistance even higher than austenitic ductile iron;
– hammers;
– parts of threshing drums.

Advantages and applications of austenitic ductile iron:

– no tempering is required after hardening;
– lower strain rate than that of hardening and tempering (isothermal transformation);
– savings are achieved by machining before heat treatment;
– often, wear resistance and strength are also improved;
– for a given surface – increased wear resistance;
– increased ductility and impact resistance for the same hardness;
– density 10% less than that of steel;
– ductile cast iron from austenitic tempering provides higher strength-to-weight ratio;
– lower production costs for castings near a given shape (0.2-0.4% increase in volume);
– good machinability;
– higher damping capacity;
– good casting throwing ability.

Acetylene ductile iron has found successful applications in many industries, including construction, mining, agriculture, automotive, heavy truck and railroad. It is commonly used in applications where both strength and impact resistance are required at the same time. In order to make parts made of economically alloyed cast iron highly resistant to wear, they can be isothermally machined into it with a bainite structure. Material with such structure is just as wear resistant as nitrided material. It makes no sense to subject the material to nitriding itself because of the considerable duration of the process and the brittleness of the resulting layer. In the works of A.I. Belyakov et al. [15] & V. Dubrov [16] point out that the highest wear resistance is possessed by cast irons having a bottom bainite structure and the strength of isothermally hardened irons is at a high level. Isothermal hardening makes it possible to form bainite without pearlite inclusions and structurally free ferrite. At the same time this method requires special equipment and additional production area for placing hardening tubs, the use of scarce alkalis as hardening conditions. The complexity of the method also consists in the difficulty of ensuring constant temperature of the baths, which is associated with high energy costs. At low durations in the tub, cast iron acquires high hardness. This is caused by the presence of a large amount of martensite formed during the precooling of the samples from the isothermal temperature in water. The bainite transformation in ferrite cast irons is slower in the beginning than in pearlitic ones, as indicated by their high hardness. The bainite transformation begins to develop intensively in cast irons with a ferritic initial structure after more than 10 minutes of aging.

At the same time, in the work of J. He et al. [17] demonstrate that carbide-free nanobainitic steels have an excellent combination of high strength and toughness combined with inexpensive adaptability through low-temperature isothermal treatment. In a study by W. Gong et al. [18] reported that the key to obtaining steels with such properties is to reduce the martensitization initiation temperature, suppress the release of carbides and, therefore, create an optimal microstructure of nanosized plates of bainite ferrite, in sum with small layers of residual austenite. Such alloys have the advantage of controlling the number and size of phases by heat treatment compared to conventional high-strength steels, but are less common due to the expensive alloying elements present in the composition.

To properly design a nanobainite alloy, it is necessary to have an understanding of the effects of conventional alloying additives on the bainite transformation as well as the resulting properties. The main dependence of the kinetics of the bainite transformation is the stability of the austenitic and ferrite phases at temperature, during the transformation. Also, in the work of S. Hasan et al. [4] the strength of nanobainite alloy depends on the plate thickness of bainite ferrite and, in general, its amount, while its ductility will depend on the amount and stability of residual austenite in the microstructure. The rate of bainite transformation is significantly affected by the addition of martensite (0.29%) along with a moderately high percentage of aluminum (0.9%) by J. Tian et al. [19], M. Soliman & H. Palkowski [5] & W. Liu et al. [20]. Provision of high-strength structures of the metal matrix of cast iron is possible due to rational alloying and rationally chosen temperature-time parameters of the heat treatment regime. Nanobainitic carbide-free steels entail a combination of high strength and impact toughness combined with inexpensive adaptability by low-temperature isothermal treatment. Therefore, the creation of composite structures in high-strength cast irons with spheroidal graphite is an effective way to harden it, expanding the field of its application.

Conclusions

Therefore, continuous air cooling is an effective way of obtaining the bainite structure in economically alloyed ductile cast irons. The optimum mode of heat treatment providing rational structure and properties of ductile iron castings with nodular graphite for parts of stopper devices for oilfield equipment has been established. Consequently, the analysis of issues related to the structure formation of bainite iron shows that changes in the austenitizing temperature, the time of isothermal aging of castings, temperature and cooling rate contribute to a significant change in the physical and mechanical properties. In contrast to untreated cast irons, steels subjected to the isothermal process have a higher strength, and regardless of alloying, hardening provides the maximum strength value. The structural formation and kinetics of the bainite transformation in steels have been studied in detail and are well described in the fundamental literature. But, unfortunately, the details of austenization and transformation of the matrix into bainite, in cast irons with spheroidal graphite are not studied as qualitatively. Heating to a temperature that destroys the crystal structure of the metal, up to becoming austenitic, hardens carbon steel and other carbon-rich iron alloys.

The advantages of isothermal hardening are: increased strength (the crystal structure of martensite or bainite, after isothermal hardening, significantly hardens metals, unlike untreated ones), impact resistance (where untreated metals can tear or crack, austenitic components are likely to withstand the impact while maintaining their shape, metals with hardening have this property due to their extremely strong crystal structure). Reduced distortion (due to the plasticity acquired during the hardening process, this metal exhibits less deformation compared to untreated steel. For thin components that need to maintain their dimensions during and after treatment, this is a particularly useful property). Ensuring high-strength structures of the metal matrix of cast iron is possible due to rational alloying and rationally chosen temperature-time parameters of the heat treatment regime. The tasks for further research related to the study of nanobainite steels, which do not contain carbide, entail a combination of high strength and toughness in combination with inexpensive adaptability by low-temperature isothermal treatment. Therefore, the creation of composite structures in high-strength cast irons with spheroidal graphite is an effective way to harden it, expanding the field of its application.

References

[1] Hernando J, Elfsberg J, Dahle A, Dioszegi A. Evolution of primary austenite during coarsening and impact on eutectic microstructure in Fe-C-Si alloys. *Materialia.* 2019;(7):article number 100391.

[2] Hernando J, Elfsberg J, Ghassemali E, Dahle A, Dioszegi A. The effect of coarsening of primary austenite on the ultimate tensile strength of hypoeutectic compacted graphite Fe-C-Si alloys. *Scripta Mater.* 2019;(168):33-7.

[3] Hu H, Xu G, Dai F, Tian J, Chen G. Critical ausforming temperature to promote isothermal bainitic transformation in prior-deformed austenite. *Mater. Sc. and Technol.* 2019;(35(4)):1-4.

[4] Hasan S, Ghosh M, Chakrabarti D, Singh S. Development of continuously cooled low-carbon, low-alloy, high strength carbide-free bainitic rail steels. *Mater. Sc. and Engineer. A.* 2020;(771):article number 138590.

[5] Soliman M, Palkowski H. Tensile properties and bake hardening response of dual phase steels with varied martensite volume fraction. *Mater. Sc. and Engineer. A.* 2020;(777):article number 139044.

[6] Hasanli RK. An effective way of obtaining bainite structure in alloyed high-strength cast irons. *Mechan., Mater. Sc. & Engineer.* 2016;(12):7-12.

[7] Writzl V, Rovani AC, Pintaude G, Lima MSF, Guesser WL, Borges PC. Scratch resistances of compacted graphite iron with plasma nitriding, laser hardening, and duplex surface treatments. *Tribol. Internat.* 2020;(143):article number 106081.

[8] Lyu Y. Abrasive wear of compacted graphite cast iron with added tin. *Metallogr., Microstr., and Analys.* 2019;(8(1)):67-71.

[9] Feng JJ, Pan CX, Lu LL, Huang QW, Cao HT. Plasma transferred arc surface alloying of Cr-Ni-Mo powders on compacted graphite iron. *J. of Ir. and St. Res. Internat.* 2016;(23(6)):618-24.

[10] Slatter T, Lewis R, Jones AH. The influence of induction hardening on the impact wear resistance of compacted graphite iron (CGI). *Wear.* 2011;(270(3-4)):302-11.

[11] Ghaderi AR, Ahmadabadi NM, Ghasemi HM. Effect of graphite morphologies on the tribological behavior of austempered cast iron. *Wear*. 2003;(255(1)):410-16.

[12] Ghasemi R, Hassan I, Ghorbani A, Dioszegi A. Austempered compacted graphite iron – influence of austempering temperature and time on microstructural and mechanical properties. *Mater. Sc. and Engineer. A*. 2019;(767):article number 138434.

[13] Eiken Dg, Subasic E, Lacaze J. 3D phase-field computations of microsegregation in nodular cast iron compared to experimental data and CalPhad-based Scheil-prediction. *Materialia*. 2020;(9):article number 100538.

[14] Rahaman M, Odqvist J, Hedström P. Machine learning to predict the martensite start temperature in steels. *Metallur. and Mater. Trans. A*, 2019;(50(5)):2081-91.

[15] Belyakov AI, Belyakov AA, Zhukov AA. Isothermal hardening of cast iron with nodular graphite. *Procur. Prod. in Mechan. Engineer.* 2008;(1):44-8.

[16] Dubrov V. The use of high-strength cast iron in valve building research institutes. In: Ductile Cast Iron with Nodular Graphite. Kyiv: Naukova Dumka; 1998. pp. 78-81.

[17] He J, Zhao A, Huang Y, Zhi C, Zhao F. Acceleration of bainite transformation at low temperature by warm rolling process. *Mater. Tod.: Proceed.* 2015;(2):289-94.

[18] Gong W, Tomota Y, Koo M, Adachi Y. Effect of ausforming on nanobainite steel. *Scr. Mater.*, 2010;(63(8)):819-22.

[19] Tian J, Xu G, Zhou M, Hu H, Xue Z. Effects of al addition on bainite transformation and properties of high-strength carbide-free bainitic steels. *J. of Ir. and St. Res. Internat.* 2019;(17(1)):1-7.

[20] Liu W, Zhang B, Zhao A, Guo H, Sun S. Control of morphology and dimension of blocky retained austenite in medium-carbon steel. *Mater. Res. Expres*. 2019;(6(1)):article number 16526.

Ізотермічні перетворення у високоміцному чавуні

Раміз Гасанлі, Ілгам Алієв, Нізамі Поладов, Лала Азімова, Талех Тагієв

Азербайджанський технічний університет
AZ1073, просп. Г. Джавіда, 25, м. Баку, Азербайджанська Республіка

Анотація

Актуальність. Технологічний процес виготовлення деталей з високоміцних чавунів простіший і економічніший, ніж процес виготовлення деталей із сталі. Чавуни менш чутливі до концентраторів напруг і ударних навантажень. Чавуни зі сфероїдним графітом можуть досягати марок DI 70 навіть у литому стані. Шляхом зміцнювальної термічної обробки або додаткового легування можна отримувати чавуни підвищеної міцності (марки DI 80 і вище). У міру підвищення міцнісних властивостей чавунів все більше виявляються недоліки у вигляді низької пластичності і пластичності. Ці проблеми можна компенсувати, забезпечивши аусферитну, бейнітну або бейнітно-аустенітну структуру металевої матриці чавунів. Хорошим рішенням є отримання чавунів зі складною структурою типу бейніт-аусферит. У зв'язку з цим актуальність даної роботи зумовлена тим, що в практиці сучасного машинобудування все ширше застосовуються високоміцні чавуни.

Мета. Метою даної роботи є дослідження та отримання структури бейніту за рахунок ізотермічного зміцнення. Для досягнення чого враховано особливості ізотермічного перетворення у високоміцному чавуні зі сфероїдальним графітом.

Методи. Дане дослідження ґрунтувалося на теоретичному методі (аналіз, синтез, конкретизація, узагальнення, моделювання) та емпіричному методі (вивчення дослідницько-експериментальних робіт вчених та їх досвіду в цій або подібній галузі із застосуванням подібних конструкцій та вивченням досвідченими фахівцями).

Результати. Доведено можливість та ефективність отримання бейнітної структури в економічно легованих нікелі, міді та молібдені в кількостях відповідно 1,0; Встановлено 0,5 і 0,5 % чавунів при постійному охолодженні на повітрі.

Висновки. Отримані результати та сформульовані на їх основі висновки можуть бути використані в майбутньому як ефективна наукова основа для вивчення перспектив застосування ізотермічного зміцнення легованих і нелегованих високоміцних чавунів із кулястим графітом

Ключові слова: аусферитний чавун, ізотермічне гартування, чавун з кулястим графітом, бейніт, аустенітизація

Scientific Herald of Uzhhorod University
Series “Physics”

Journal homepage: https://physics.uz.ua/en
Issue 51, 59-73
Received: 10.04.2022. Revised: 17.05.2022. Accepted: 06.06.2022

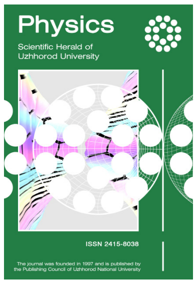

UDC 621.87
PACS: 07.05.Kf
DOI: 10.54919/2415-8038.2022.51.59-73

Optimisation of Dynamic Loads of Rope Systems of Lifting Mechanisms of Bridge Cranes During Cargo Handling

Yuiry V. Chovnyuk[1*], Liubov A. Diachenko[2], Yevhen O. Ivanov[3], Nataliya P. Dichek[2], Olha V. Orel[4]

[1]National University of Life and Environmental Sciences of Ukraine
03041, 12b Heroyiv Oborony Str., Kyiv, Ukraine
[2]Separated Structural Subdivision “Nizhyn Applied College of National University of Life and Environmental Sciences of Ukraine”
16600, 26 T. Shevchenko Str., Nizhyn, Ukraine
[3]National Aviation University
03058, 1 Liubomyr Huzar Ave., Kyiv, Ukraine
[4]National Academy of Pedagogical Sciences of Ukraine
04053, 52-D Sichovykh Striltsiv Str., Kyiv, Ukraine

Abstract

Relevance. In this study, considerable attention is devoted to the analysis of dynamic loads that occur in the rope systems of lifting mechanisms of overhead cranes during start-up and braking, and the reduction of these loads. **Purpose.** To identify the magnitude and nature of changes in dynamic loads in the elements of lifting mechanisms of bridge cranes, a comprehensive dynamic analysis of the lifting mechanism of the bridge crane and its elastic elements (rope systems) was performed.

Methods. The dynamic analysis of the above mechanisms and systems was performed on well-grounded mathematical models of bridge-type cranes (single- and double-mass).

Results. The analysis of the obtained calculations of mathematical models of the mechanism of lifting the load of bridge cranes demonstrated that the dynamic loads applied to the structural elements and drive mechanisms are oscillatory and comparable to static loads. The analysis of the obtained calculations of mathematical models of the mechanism of lifting the load of bridge cranes demonstrated that the dynamic loads applied to the structural elements and drive mechanisms are oscillatory and comparable to static loads. To minimise the integral functionals, the methods of classical calculus of variations, mathematical physics and differential equations were used to model the dynamics of loading processes of rope systems and drives of bridge cranes, and the terminal (initial and final conditions of movement of such systems) were considered, which allowed solving the optimisation problem unambiguouslyThus, to reduce dynamic loads in structural elements (in particular, in ropes) during transients in such lifting mechanisms of bridge cranes, it is proposed to perform optimisation of the modes of movement of their drive mechanisms. An essential place in such optimisation is occupied by the choice of the optimisation criterion. Among such criteria, integral optimisation criteria were used. As such integral optimisation criteria, the RMS values of the current loads in the elastic elements (ropes) of overhead travelling cranes have been used.

Conclusions. Such integral criteria are integral functionalities that usually reflect undesirable properties of machines and their mechanisms, thus, they are subject to minimisation.

Keywords: dynamic optimisation, rope systems, lifting mechanisms, overhead cranes, cargo handling, transients

Suggested Citation:
Chovnyuk YuV, Diachenko LA, Ivanov YeO, Dichek N.P., Orel OV. Optimisation of dynamic loads of rope systems of lifting mechanisms of bridge cranes during cargo handling. *Scientific Herald of Uzhhorod University. Series “Physics”.* 2022;(51):59-73.

*Corresponding author

Introduction

Lifting and transporting machines belong to machines with increased danger during lifting, transporting and installation works. The safe operation of these machines largely determines the magnitude and nature of the change in time of the acting loads on the structural elements and drive mechanisms. Particularly dangerous for the operation of lifting and transport machines are dynamic loads that change in time and can result in complex oscillatory processes in structural elements. Such fluctuations significantly affect the stability of the lifting machines and result in fatigue failure of their elements. All this affects the operational reliability of both lifting and transporting machines. The reliability of lifting and transport machines can be significantly improved by reducing dynamic loads on their structures and drive mechanisms. Particularly dangerous for lifting and transport machines are dynamic loads that occur during transient processes of movement, in particular, starting and deceleration of drive mechanisms. Thus, for example, a slight decrease in dynamic loads during start-up of up to 30% and deceleration of up to 40% of the mechanisms of portal cranes allowed increasing the overhaul cycle of these cranes from 2 to 5 times. Thus, in this study, considerable attention is devoted to the analysis of dynamic loads that occur in the rope systems of lifting mechanisms of overhead cranes during start-up and braking, and the reduction of these loads. To identify the magnitude and nature of changes in dynamic loads in the elements of lifting mechanisms of bridge cranes, a comprehensive dynamic analysis of the lifting mechanism of the bridge crane and its elastic elements (rope systems) was performed. The dynamic analysis of the above mechanisms and systems was performed on well-grounded mathematical models of bridge-type cranes (single- and double-mass).

The analysis of the obtained calculations of mathematical models of the mechanism of lifting the load of bridge cranes demonstrated that the dynamic loads applied to the structural elements and drive mechanisms are oscillatory and comparable to static loads. Thus, to reduce dynamic loads in structural elements (in particular, in ropes) during transients in such lifting mechanisms of bridge cranes, it is proposed to perform optimisation of the modes of movement of their drive mechanisms. An essential place in such optimisation is occupied by the choice of the optimisation criterion. Among such criteria, primarily, integral optimisation criteria were used. In the majority of cases, as such integral optimisation criteria, the RMS values of the current loads in the elastic elements (ropes) of overhead travelling cranes have been used. Such integral criteria are integral functionalities that usually reflect undesirable properties of machines and their mechanisms, thus, they are subject to minimisation. To minimise the integral functionals, the methods of classical calculus of variations, mathematical physics and differential equations were used to model the dynamics of loading processes of rope systems and drives of bridge cranes, and the terminal (initial and final conditions of movement of such systems) were considered, which allowed solving the optimisation problem unambiguously. As a result of the performed optimisation of the modes of movement of the drive mechanisms of lifting bridge cranes in the areas of transitional processes, the dynamic loads of the rope systems of bridge cranes are significantly reduced, the smoothness of the movement of the main elements of such mechanisms is achieved and oscillatory processes are practically eliminated.

The predecessor scientists conducted a comprehensive analysis of dynamic loads in the structural elements of overhead cranes during their start-up and deceleration [1-3]. However, such an analysis has significant disadvantages, since the driving forces that result in the necessary movement of the lifting mechanisms of bridge cranes were not established, and the problem was reduced to the analysis and synthesis of the modes of movement of mechanisms in the presence of specific kinematic terminal conditions [4]. This, in turn, has resulted in inaccuracies and frankly vast formulas that describe the optimal modes of movement (of ropes with loads) in such mechanisms, which has no practical use, since it does not evaluate the usual engineering indicators of movement in such systems (for example, dynamism coefficients). To eliminate such disadvantages, this study was performed, which allowed determining the coefficients of dynamism in the transient modes of functioning of lifting mechanisms and rope systems of overhead travelling cranes for typical methods of lifting loads: “from weight” and “with pickup”/”from the base” [5].

The purpose of the research is to substantiate the modes of starting the lifting mechanisms of overhead travelling cranes, which minimise dynamic loads in rope systems in different ways of lifting the load: “from the weight”, “with pickup”/”from the base”.

Materials and Methods

In the work, the dynamic load on the load-gripping devices was evaluated in two variants – lifting the load: “from weight” and “with pickup”/”from the base”. In the first variant, it is assumed that the load is at a specific (small) height above the base, and the static load acting on the load gripping devices is equal to the weight of the load Q_l. Dynamic load P_{dyn} occurs at the initial moment of deceleration of the descending load when the brakes are applied [4-6].

In the second variant of loading, it is assumed that the load is on any base, the ropes are sagging, and, accordingly, at this moment, the load on the load-catching devices is zero.

In determining the dynamic load, the masses, m_r and m_l are attributed to the periphery of the drum, and the mass m_l is determined proportionally to the square of the ratio of the number of branches of the cargo chain hoist, which are wound (or winding) on the drum, to the total number of branches on which the load hangs [1].

When determining the starting modes of the lifting mechanisms of overhead cranes, the results of the following indicators were considered: excessive driving force, rope speed and rigidity of the supporting structure, mass of the engine rotor and load, kinetic and potential excessive force, system stiffness and time, load dynamics, oscillation frequency, conditions and mode of movement, etc. When assessing the dynamic load on load-gripping devices, the following should be considered: under conditions of proper operation, mainly only the vertical dynamic load during the operation of the load-lifting mechanism is significant, since, during the operation of the crane movement mechanisms and the rotation of its slewing part, it does not exceed 5-6% of the static load (Fig. 1) [1; 2].

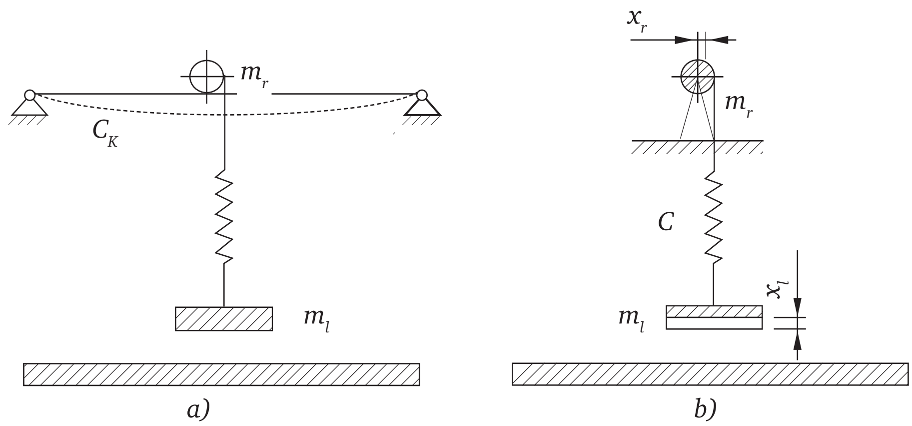

Figure 1. Scheme of dynamic loading of a loading device when lifting a load "from weight"
Note: a) on an overhead crane; b) design scheme
Source: [1; 2]

There are two options for lifting the load: "from weight" and "with pickup"/"from the base" [4-6]. In both cases, the dynamic coefficient (K_d) is determined by the dependence:

$$K_d = 1 + P_{dyn}/Q_l \ , \tag{1}$$

where: P_{dyn} – in the first case is a function of the excess driving force and the stiffness of the supporting structure and in the second case is a function of the rope speed and the stiffness of the supporting structure.

Results

When designing in the case of lifting a load: "from weight" the crane is modelled by a two-mass oscillating system [7-9]. In this system, the stiffness of the ropes and the crane C_K structure are replaced by the reduced stiffness C_p, and the system itself consists of two masses – m_r (mass of the rotor of the engine and the reduced masses of the elements of the lifting mechanism) and m_l (mass of the load), connected by stiffness C:

$$C_p = \frac{C_K}{(C+C_K)} \ . \tag{2}$$

When moving x_r mass m_r and x_l mass m_l, the kinetic and potential energy are respectively:

$$\begin{cases} K = \frac{m_r}{2} \cdot (\dot{x}_r)^2 + \frac{m_l}{2} \cdot (\dot{x}_l)^2; \\ P = C \cdot \{(x_r - x_l)^2/2\} \end{cases} \tag{3}$$

For the mass, m_r the driving force is the weight of the cargo Q_l ($Q_l = m_l \cdot g, g$ – acceleration of free fall, g=9.81 m/s^2), and the excessive force of the engine T_{exc}; for the mass m_l – weight of the cargo Q_l, acting in the same way as the inertial force of the cargo during lifting.

In cranes with the drive of the load-lifting mechanism from a three-phase current motor, the excess force T_{exc} can be considered constant (with other laws of change of the driving force, and, accordingly, the excess force, the dynamism of the lifting process will be less) [1]. The equations of motion have the type:

$$\begin{cases} m_r \cdot \ddot{x}_r + C \cdot (x_r - x_l) = Q_l + T_{exc}; \\ m_l \cdot \ddot{x}_l - C \cdot (x_r - x_l) = -Q_l, \end{cases} \tag{4}$$

where: $(x_r – x_l)$ – can be denoted by ξ. Then:

$$\dot{\xi} = (\dot{x}_r - \dot{x}_l); \ \ddot{\xi} = (\ddot{x}_r - \ddot{x}_l). \tag{5}$$

In the new notation (ξ) and (5) instead of (4) have:

$$\begin{cases} m_r \cdot \ddot{x}_r + C \cdot \xi = Q_l + T_{exc}; \\ m_l \cdot \ddot{x}_l - C \cdot \xi = -Q_l. \end{cases} \Leftrightarrow \begin{cases} \ddot{x}_r + \frac{C}{m_r} \cdot \xi = \frac{Q_l + T_{exc}}{m_r}; \\ \ddot{x}_l - \frac{C}{m_l} \cdot \xi = -Q_l/m_l \end{cases}. \tag{6}$$

After subtracting from the first equation of system (6) the second equation of the same system obtained an inhomogeneous differential equation for ξ:

$$\ddot{\xi} + \Omega^2 \cdot \xi = \frac{Q_l + T_{exc}}{m_r} + \frac{Q_l}{m_l}, \Omega^2 = C \cdot \left(\frac{1}{m_r} + \frac{1}{m_l}\right). \quad (7)$$

For the case of lifting the load "from weight" use the following initial conditions to solve (7):

$$\xi|_{t=0} = \frac{Q_l}{C};\ \dot{\xi}\big|_{t=0} = 0. \quad (8)$$

The general solution of (7) is found in the following type:

$$\xi(t) = A_1 \cdot \cos\Omega\, t + A_2 \cdot \sin\Omega\, t + \frac{1}{\Omega^2} \cdot \left\{\frac{Q_l + T_{exc}}{m_r} + \frac{Q_l}{m_l}\right\}. \quad (9)$$

Considering the conditions (8), from (9) have:

$$A_1 = \frac{Q_l}{C} - \frac{1}{\Omega^2} \cdot \left\{\frac{Q_l + T_{exc}}{m_r} + \frac{Q_l}{m_l}\right\};\ A_2 = 0. \quad (10)$$

Then the solution of $\xi(t)$ (9) is given as follows:

$$\xi(t) = \left(\frac{Q_l}{C}\right) \cdot \cos\Omega\, t + \frac{1}{\Omega^2} \cdot \left(\frac{Q_l + T_{exc}}{m_r} + \frac{Q_l}{m_l}\right) \cdot (1 - \cos\Omega\, t). \quad (11)$$

Present (11) in a more convenient form for analysis:

$$\xi(t) = \left(\frac{Q_l}{C}\right) \cdot \cos\Omega\, t + \frac{2}{\Omega^2} \cdot \left\{\frac{Q_l + T_{exc}}{m_r} + \frac{Q_l}{m_l}\right\} \cdot \sin^2\left(\frac{\Omega t}{2}\right). \quad (12)$$

The force in the elastic element (in the elastic link), which can be considered as the impact of the load on the load-carrying devices:

$$P_{LC} = C\xi = Q_l \cdot \cos\Omega\, t + \frac{2C}{\Omega^2} \cdot \left\{\frac{Q_l + T_{exc}}{m_r} + \frac{Q_l}{m_l}\right\} \cdot \sin^2\left(\frac{\Omega t}{2}\right). \quad (13)$$

Its value is variable and is a function of system stiffness, C and time t. The maximum value of force in an elastic link P_{LCmax} occurs at:

$$\cos\Omega\, t = -1 \Rightarrow \Omega t = (2n-1) \cdot \pi, n \in N, \quad (14)$$

that is, in moments of time:

$$t* = \frac{(2n-1)\cdot\pi}{\Omega}, n \in N, \quad (15)$$

$$P_l \frac{2\cdot m_l}{(m_r+m_l)}{}_{exc\,LCmax}. \quad (16)$$

Since the excess force T_{exc}=ϕ·Q_l (where ϕ – is the proportionality factor [1]), then:

$$P_l \left\{1 + 2\phi \cdot \frac{m_l}{m_l + m_r}\right\}_{LCmax}, \quad (17)$$

and the coefficient of dynamism has the form:

$$K_d|_{t=t*} = \frac{P_{LCmax}}{Q_l \left\{\frac{m_l}{(m_l+m_r)}\right\} \frac{2m_l}{(m_l+m_r)} \frac{T_{exc}}{Q_l}}, \quad (18)$$

where: the last expression for the coefficient (K_d) characterises the dynamic loading of the load-gripping device, provided that the lifting begins when the weight of the load affects the ropes Q_l [10-12].

To establish the dependence K_d (t) the following relation is used:

$$K_d(t) = 1 + \frac{m_l}{(m_l+m_r)} \cdot \frac{T_{exc}}{Q_l} \cdot (1 - \cos\Omega\, t), \quad (19)$$

or:

$$K_d(t) = 1 + \frac{m_l}{(m_l+m_r)} \cdot \frac{T_{exc}}{Q_l} \cdot 2 \cdot \sin^2\left(\frac{\Omega t}{2}\right). \quad (20)$$

At $\frac{\Omega t}{2} = (2n_1 - 1) \cdot \left(\frac{\pi}{2}\right), n_1 \in N$, that is, at:

$$t ** = \frac{(2n_1 - 1)\cdot\pi}{\Omega}, n_1 \in N. \quad (21)$$

K_d (t) assumes the maximum values:

$$K \frac{2\cdot T_{exc}\cdot m_l}{Q_l\cdot(m_r+m_l)}{}_{dmax}. \quad (22)$$

When decelerating the descending load P_{dyn} and the coefficient of dynamism K_d are determined by formulas (13)-(18), and K_d (t) – by formulas (19)-(22) [13-15]. Therewith, under the T_{exc} understand the following difference:

$$T_{exc} = T_{dec} - Q_l, \quad (23)$$

where: T_{dec} – deceleration force applied to the load.

As the moment generated by the brakes is usually less than the maximum torque [1; 2] generated by the engine, the dynamic force when braking the load being lowered does not exceed the dynamic force that occurs when lifting the load "from weight". Define further the laws of motion of masses m_p and $m_в$, based on the equations of the system (4), (6), (7) and the law $\xi(t)$ (11), (12) under the following (non-zero) initial conditions (when lifting the load "from weight"):

$$x_l|_{t=0} = 0;\ \dot{x}_l|_{t=0} = 0;\ x_r|_{t=0} = x_l|_{t=0} + \frac{Q_l}{C} = \frac{Q_l}{C};\ \dot{x}_r| = 0. \quad (24)$$

From system (6) for x_r have:

$$\ddot{x}_r + \frac{C}{m_r} \cdot \xi(t) = \frac{Q_l + T_{exc}}{m_r}. \qquad (25)$$

From system (6) for x_l have:

$$\ddot{x}_l + g = \frac{C}{m_l} \cdot \xi(t). \qquad (26)$$

Equations (25) and (26) must be solved under the initial conditions (24). Knowing $\xi(t)$ (11) and integrating twice for t each of equations (25) and (26), obtain [16-18]:

$$x_r(t) = \frac{2m_l^2 \cdot T_{exc}}{C \cdot (m_r + m_l)^2} \cdot sin^2\left(\frac{\Omega t}{2}\right) + \frac{(Q_l + T_{exc})}{2m_r} \cdot t^2 + \frac{Q_l}{C}, \qquad (27)$$

$$x_l(t) = -\frac{2m_r \cdot m_l \cdot T_{exc}}{C \cdot (m_r + m_l)^2} sin^2\left(\frac{\Omega t}{2}\right) + \frac{T_{exc}}{(m_r + m_l)} \cdot \frac{t^2}{2}. \qquad (28)$$

From (27) and (28) evidently seen that the mass m_l and the mass m_r have oscillations whose frequency is Ω [19]. Define the conditions and modes of motion $\xi(t)$, $x_l(t)$, $x_r(t)$,under which in the period of acceleration of the system (before the lifting mechanism acquires a steady speed of lifting/lowering the load (V)) there are no oscillatory processes in the mass m_r, and mass m_l. Suppose that the duration of the system start-up, during which the steady-state mode of lifting the load is established, i.e. the speed of movement (during lifting) becomes a constant value and is V, equal to τ_Π. Then the motion for which the coordinate $\xi(t)$ satisfies the motion quality criterion:

$$\left\{\frac{1}{\tau_\Pi} \cdot \int_0^{\tau p} (\xi(t))^2 dt\right\}^{1/2} \Rightarrow min, \qquad (29)$$

and will be the sought mass m_r and m_l systems. A necessary condition for the implementation of the criterion (29) is the Euler-Poisson equation, which can be obtained by replacing the integral expression (29) $\xi(t)$ with the expression (according to (7)):

$$\xi(t) = \frac{1}{\Omega^2} \cdot \left\{\frac{Q_l + T_{exc}}{m_r} + \frac{Q_l}{m_l} - \ddot{\xi}\right\}. \qquad (30)$$

then the above (Euler-Poisson) equation for (29), (30) becomes as follows:

$$\xi^{(IV)} = 0. \qquad (31)$$

Consider the solution of (31) as a spline of the third order in t:

$$\xi(t) = a_1 + a_2 \cdot t^1 + a_3 \cdot t^2 + a_4 \cdot t^3. \qquad (32)$$

To find the undefined constants $a_i, i = \overline{(1.4)}$, use the following conditions (terminal):

$$\xi|_{t=0} = \frac{Q_l}{C};\ \dot{\xi}\Big|_{t=0} = 0;\ \ddot{\xi}\Big|_{t=0} = \left\{\frac{Q_l + T_{exc}}{m_r} + \frac{Q_l}{m_l}\right\} - \Omega^2 \cdot \xi|_{t=0} = \frac{Q_l + T_{exc}}{m_r} + g *, \qquad (33)$$

where: $g *= g - \Omega^2 \cdot \frac{Q_l}{C}$. The last terminal condition is of the form:

$$\dot{\xi}\Big|_{t=\tau_p} = 0. \qquad (34)$$

Differentiating by t the appropriate number of times the expression (32) and using the conditions (33), (34), obtain:

$$a_1 = \frac{Q_l}{C};\ a_2 = 0;\ 2a_3 = \frac{Q_l + T_{exc}}{m_r} + g *;\ a_4 = -\frac{2a_3}{3\tau_p}. \qquad (35)$$

Thus, for the traffic quality criterion (29) or (30) to be satisfied, it is necessary that $\xi(t)$ the time varies according to the following law:

$$\xi(t) = \frac{Q_l}{C} + \left\{\frac{Q_l + T_{exc}}{m_r} + g *\right\} \cdot \frac{t^2}{2} - \left\{\frac{Q_l + T_{exc}}{m_r} + g *\right\} \cdot \frac{t^3}{3\tau_p}. \qquad (36)$$

or:

$$\xi(t) = \frac{Q_l}{C} + \left\{\frac{Q_l + T_{exc}}{m_r} + g *\right\} \cdot \left\{\frac{t^2}{2} - \frac{t^3}{3\tau_p}\right\}. \qquad (37)$$

Then P_{LC} takes the form:

$$P_{LC} = C \cdot \xi(t) = Q_l + C \cdot \left\{\frac{Q_l + T_{exc}}{m_r} + g *\right\} \cdot \left(\frac{t^2}{2} - \frac{t^3}{3\tau_p}\right). \qquad (38)$$

For $K_d(t)$ have:

$$K_d(t) = \frac{P_{LC}(t)}{Q_l} = 1 + C \cdot \left\{\frac{1 + T_{exc}/Q_l}{m_r} + \frac{g*}{m_l \cdot g}\right\} \cdot \left\{\frac{t^2}{2} - \frac{t^3}{3\tau_p}\right\}. \qquad (39)$$

The maximum values P_{LC} (t) of (38) and K_d (t) (39) are obtained at the end of the transient process (start-up) at $t = \tau_p$:

$$Pl\left\{\frac{Q_l+T_{exc}}{m_r} + g *\right\}\frac{\tau_p{}^2}{6}{}_{LCmax}, \qquad (40)$$

$$K\left\{\frac{1+T_{exc}/Q_l}{m_r} + \frac{g*}{m_l \cdot g}\right\}\frac{\tau_p{}^2}{6}{}_{dmax}. \qquad (41)$$

Further find the laws of motion x_l (t) and x_r (t), which have masses m_l and m_r at $\xi(t)$ (36), and satisfy the terminal conditions (24):

$$x_r(t) = \left(-\frac{C}{m_r}\right)\cdot\left\{\frac{Q_l}{C}\cdot\frac{t^2}{2} + \left(\frac{Q_l+T_{exc}}{m_r} + g *\right)\cdot\left(\frac{t^4}{24} - \frac{t^5}{60\tau_p}\right)\right\} + \left(\frac{Q_l+T_{exc}}{m_r}\right)\cdot\frac{t^2}{2} + \frac{Q_l}{C}, \qquad (42)$$

$$x_l(t) = \left(\frac{C}{m_l}\right)\cdot\left\{\frac{Q_l}{C}\cdot\frac{t^2}{2} + \left(\frac{Q_l+T_{exc}}{m_r} + g *\right)\cdot\left(\frac{t^4}{24} - \frac{t^5}{60\tau_p}\right)\right\} - \frac{gt^2}{2}. \qquad (43)$$

Using the dependencies $\dot{x}_r(t)$ and $\dot{x}_l(t)$ and their values at the moment $t = \tau_p$, namely: $\dot{x}_r|_{t=\tau_p} = \dot{x}_l|_{t=\tau_p} = V$, can be found the value of τ_Π and V:

$$\frac{\left(-\frac{C}{m_r}\right)\cdot\left\{\frac{Q_l}{C}\cdot\tau_p + \left(\frac{Q_l+T_{exc}}{m_r}+g*\right)\cdot\left(\frac{\tau_\Pi{}^3}{12}\right)\right\} + \left(\frac{Q_l+T_{exc}}{m_r}\right)\cdot\tau_p}{\left(\frac{C}{m_l}\right)\cdot\left\{\frac{Q_l}{C}\cdot\tau_p + \left(\frac{Q_l+T_{exc}}{m_r}+g*\right)\cdot\left(\frac{\tau_p{}^3}{12}\right)\right\} - g\cdot\tau_p} = 1, \qquad (44)$$

Thus, have:

$$\tau_p = \left\{\frac{12\cdot\left(\frac{T_{exc}}{m_r}\right)}{\Omega^2\left(\frac{Q_l+T_{exc}}{m_r}+g*\right)}\right\}^{1/2}. \qquad (45)$$

Knowing from the relation (45) τ_Π it is easy to find V as follows (this value must satisfy the provisions, standards that are accepted for crane structures and, obviously, not exceed them for specific types of crane loads and specific types of work performed by them on cargo handling) [20]:

$$V = \frac{1}{2}\cdot\left\{C\cdot\left(\frac{1}{m_l} - \frac{1}{m_r}\right)\cdot\left[\frac{Q_l}{C}\cdot\tau_p + \left(\frac{Q_l+T_{exc}}{m_r} + g *\right)\cdot\left(\frac{\tau_p{}^3}{12}\right)\right] + \left(\frac{Q_l+T_{exc}}{m_r} - g\right)\cdot\tau_p\right\}. \qquad (46)$$

For the case of lifting the load "from the base"/"with pickup", the following initial conditions should be used to solve (7):

$$\xi|_{t=0} = 0;\ \dot{\xi}\big|_{t=0} = v_0, \qquad (47)$$

where: v_0 – initial speed of steady-state movement of the system in the process of lifting the load.

The following considerations v_0 can be used to determine the value. When the weight of the load $Q_l = m_l \cdot g$ is on the base, it deforms the latter and the magnitude of the displacement $\tilde{x}_\Pi$ of the base due to the force on it Q_l is $\tilde{x}_\Pi = Q_l/C_{base}$, where C_{base} – is the stiffness coefficient of the base [18; 21]. When the load is detached from the base in this method of lifting it with a crane, all the potential energy that the load has as a result of interaction with this base and its deformation is transferred (due to the presence of the law of conservation of energy in mechanics) to the kinetic energy of the load movement with the initial speed v_0. Thus, there is the following correlation:

$$\frac{C_{base}\cdot\tilde{x}_p{}^2}{2} = \frac{m_l\cdot v_0{}^2}{2} \Rightarrow v_0 = \sqrt{\frac{m_l\cdot g^2}{C_{base}}} = g\cdot\sqrt{\frac{m_l}{C_{base}}} = \sqrt{\frac{Q_l\cdot g}{C_{base}}}. \qquad (48)$$

The general solution of (7) is again sought in the form of (9), but now considering the conditions (47), obtained:

$$A_1 = \left(-\frac{1}{\Omega^2}\right)\cdot\left(\frac{Q_l+T_{exc}}{m_r} + \frac{Q_l}{m_l}\right);\ A_2 = \frac{v_0}{\Omega}. \qquad (49)$$

Then the solution of $\xi(t)$ (9) is given as follows:

$$\xi(t) = \frac{2}{\Omega^2}\cdot\left\{\frac{Q_l+T_{exc}}{m_r} + \frac{Q_l}{m_l}\right\}\cdot sin^2\left(\frac{\Omega t}{2}\right) + \frac{v_0}{\Omega}\cdot sin\,\Omega\,t. \qquad (50)$$

The force in the elastic element/rope, which can now be considered as the impact of the load on the load-carrying devices, will be:

$$P_{LC} = C\cdot\xi(t) = \frac{2C}{\Omega^2}\left\{\frac{Q_l+T_{exc}}{m_r} + \frac{Q_l}{m_l}\right\}\cdot sin^2\left(\frac{\Omega t}{2}\right) + \frac{C\cdot v_0}{\Omega}\cdot sin\,\Omega\,t. \qquad (51)$$

Using the relations of elementary trigonometry, (51) can be represented as follows:

$$P_{LC}(t) = \frac{2C}{\Omega}\cdot sin\left(\frac{\Omega t}{2}\right)\cdot\left\{\frac{\left(\frac{Q_l+T_{exc}}{m_r}+\frac{Q_l}{m_l}\right)}{\Omega} + v_0\cdot cos\left(\frac{\Omega t}{2}\right)\right\}. \qquad (52)$$

Analysis of the relations (50)-(52) demonstrates that in this variant of lifting the load ("with pickup") at the time moments t^* (15) the value P_{LCmax} is even greater than in the case of lifting the load "from the weight", since now:

$$P_{LCmax}\big|_{t=t^*l}\frac{2m_l}{(m_r+m_l)}{}_{exc}\Big|. \quad (53)$$

Considering the arguments given above for (17), (18), now have that the dynamism coefficient takes the form:

$$K_d(t)\big|_{t=t^*} = 2 + \frac{2m_l}{(m_r+m_l)}\cdot\frac{T_{exc}}{Q_l}. \quad (54)$$

Consequently, when lifting the load "from the base"/"with pickup", the value K_d at specific moments of time (t^*) acquires even greater values than when lifting "from the weight". Now define the law of motion $\xi(t)$ that satisfies the quality criterion (29), but with the lifting method "from the base"/"with pickup".

Repeating the above algorithm for the method of lifting the load "from the weight" have the following results. Again $\xi(t)$ search in the form (32), since $\xi(t)$ must satisfy (31). But now the initial and final conditions change, i.e. instead of (33) have [22]:

$$K_d(t)\big|_{t=t^*} = 2 + \frac{2m_l}{(m_r+m_l)}\cdot\frac{T_{exc}}{Q_l}. \quad (55)$$

Then for the coefficients of the spline by t function $\xi(t)$ (32) have:

$$a_1 = 0;\ a_2 = v_0;\ 2a_3 = \frac{Q_l+T_{exc}}{m_r} + g;\ a_4 = -\frac{2a_3}{3\tau_p}. \quad (56)$$

Thus, for the traffic quality criterion (29) or (30) to be satisfied, it is necessary that $\xi(t)$ the following law of change over time be satisfied t:

$$\xi(t) = v_0\cdot t + \left\{\frac{Q_l+T_{exc}}{m_r} + g\right\}\cdot\left\{\frac{t^2}{2} - \frac{t^3}{3\tau_p}\right\}. \quad (57)$$

Then P_{LC} takes the form:

$$P_{LC}(t) = C\cdot\xi(t) = C\cdot v_0\cdot t + C\cdot\left\{\frac{Q_l+T_{exc}}{m_r} + g\right\}\cdot\left\{\frac{t^2}{2} - \frac{t^3}{3\tau_p}\right\}. \quad (58)$$

For K_d (t) have:

$$K_d(t) = \frac{P_{LC}{}^{(total)}}{Q_l} = \frac{Q_l+P_{LC}(t)}{Q_l} = 1 + \frac{P_{LC}(t)}{Q_l}, \quad (59)$$

where $P_{LC}{}^{(total)}$ – is the total force load of the load-carrying device: $P_{LC}{}^{(total)} = Q_l + P_{LC}(t)$, or:

$$K_d(t) = 1 + \frac{C\cdot v_0\cdot t}{Q_l} + \frac{C}{Q_l}\cdot\left\{\frac{Q_l+T_{exc}}{m_r} + g\right\}\cdot\left\{\frac{t^2}{2} - \frac{t^3}{3\tau_p}\right\}. \quad (60)$$

This coefficient reaches its maximum value at the moment $t = \tau_p$:

$$K_d(t)\big|_{t=\tau_p} = K_d(\tau_p) = K\frac{C\cdot v_0\cdot\tau_p}{Q_l}\frac{C}{Q_l}\left\{\frac{Q_l+T_{exc}}{m_r} + g\right\}\frac{\tau_p{}^2}{6}{}_{dmax}. \quad (61)$$

From (60) it is obvious that in this case K_d (t) it is less than in the law of motion $\xi(t)$ (50). The latter, moreover, results in undesirable oscillations of the load on the rope. For $\xi(t)$ (57) there are no such fluctuations [23]. Define further the laws of motion $x_r(t)$, $x_l(t)$. For this purpose again using the laws and equations (25), (26) and initial conditions:

$$x_l(t)\big|_{t=0}, \dot{x}_l(t)\big|_{t=0};\ \dot{x}_r(t)\big|_{t=0} = v_0;\ x_r(t)\big|_{t=0} = 0. \quad (62)$$

For $\ddot{x}_r(t)$ have equation (25), which must be solved under the conditions (62) at $\xi(t)$ (57). Have:

$$x_r(t) = \left(-\frac{C}{m_r}\right)\cdot\left\{\frac{v_0\cdot t^3}{6} + \left(\frac{Q_l+T_{exc}}{m_r} + g\right)\cdot\left(\frac{t^4}{24} - \frac{t^5}{60\cdot\tau_p}\right)\right\} + \left(\frac{Q_l+T_{exc}}{m_r}\right)\cdot\frac{t^2}{2} + v_0\cdot t. \quad (63)$$

$$x_l(t) = \frac{(-gt^2)}{2}\cdot\left(\frac{C}{m_l}\right)\cdot\left\{\frac{v_0\cdot t^3}{6} + \left(\frac{Q_l+T_{exc}}{m_r} + g\right)\cdot\left(\frac{t^4}{24} - \frac{t^5}{60\tau_p}\right)\right\}. \quad (64)$$

Since at where V – steady speed of lifting the load, it can be used to determine this circumstance τ_Π. Generally, the value of V is set by the operating standards of crane structures of a specific type and load lifting mechanisms that are used in this case. Thus, to find τ_p can be used, for example, expression $x_l(t)$ (64), differentiate it in time t and find the value of this last expression at $t = \tau_p$. Then have:

$$\dot{x}_l(t)\big|_{t=\tau_p} = V \Leftrightarrow (-g\tau_p) + \left(\frac{C}{m_l}\right)\cdot\left\{\frac{v_0\cdot\tau_p{}^2}{2} + \left(\frac{Q_l+T_{exc}}{m_r} + g\right)\cdot\frac{\tau_p{}^3}{12}\right\} = V. \quad (65)$$

The cubic equation (65) is obtained with regard to τ_Π, is solved using the Cardano formulas. In contrast, if the value τ_Π is given, using (65), it is easy explicitly to calculate the value V for a particular variant of lifting the load "from the base"/"with pickup". In calculation in the case of dynamic loading of the crane loading device when lifting the load "with pickup" ("from the base"), other approaches can be used [1].

In particular, it allows neglecting the stiffness of one of the elements (ropes, since the elasticity of the metal structure of the crane is much higher than that of the ropes themselves, and the oscillations of the latter quickly damped) and consider only the elasticity of the second element of stiffness – the crane structure, that is, the mass of the crane $m_к$ and the load m_l are considered as one mass m (Fig. 2).

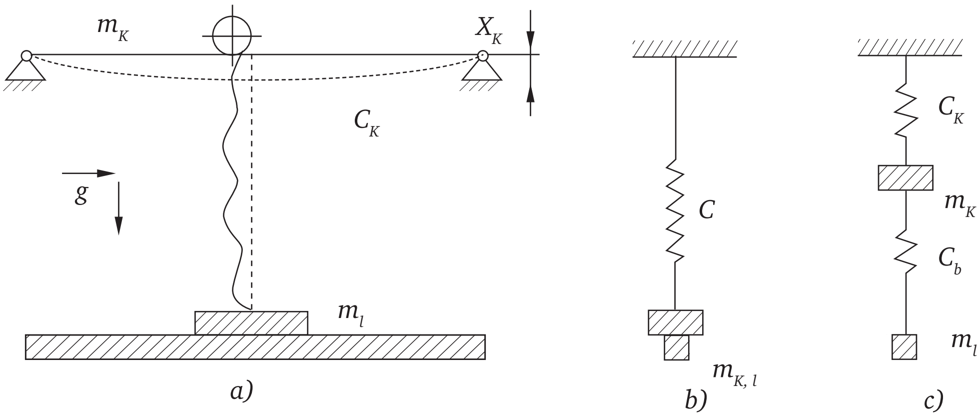

Figure 2. Scheme of dynamic loading of the load device when lifting the load "with pickup"
Note: a) on overhead cranes; b) and c) design schemes of single- and double-mass systems
Source: [1; 2]

Under the assumptions made, it can be considered that the load is lifted as follows. In the first stage, after turning on the engine. The rope slack is selected, in the second stage – elastic deformation of all structural elements (Fig. 2). The second stage continues until the force P_0 on the load-gripping devices, increasing from zero, becomes equal $Q_l = m_l{\cdot}g$. Only after that, in the third stage, the lifting of the load begins [18]. When moving $x_к$ the mass of the crane $m_к$ with rigidity $C_к$ (more precisely, the crane beam as part of the metal structure of the crane) kinetic energy:

$$W = \widetilde{m}_к \cdot \frac{\dot{x}_к{}^2}{2}, \widetilde{m}_к = m_l + m_к, \tag{66}$$

but potential energy:

$$U = C_к \cdot x_к{}^2/2. \tag{67}$$

The driving force here P, varies for different stages of lifting the load. The equation of motion of the system, which arises from the Lagrange equation of the second kind, has the form:

$$\widetilde{m}_к \cdot \ddot{x}_к + C_к \cdot x_к = P, \tag{68}$$

its solution is as follows:

$$x_к = y_{ST} + A \cdot \sin r\,t + B \cdot \cos r\,t, r = \sqrt{\frac{C_к}{(m_к+m_l)}}, \tag{69}$$

provided that at the beginning of the movement the following relations are satisfied for $x_к(t)$ and $\dot{x}_к(t)$:

$$x_к(t)|_{t=0} = y_{ST} = \frac{(m_l+m_к)\cdot g}{C_к};\ \dot{x}_к|_{t=0} = v_0, \tag{70}$$

where v_0 – the initial speed of lifting the load, i.e. the initial speed of movement of the rope when it is fully selected (its slack is eliminated); y_{ST} – deflection of the structure from a static load.

After setting the values of the coefficients A and L have:

$$\begin{cases} x_к = y_{ST} + y_{ST} \cdot \cos r\,t + \frac{v_0}{r} \cdot \sin r\,t; \\ \dot{x}_к = -r \cdot y_{ST} \cdot \sin r\,t + v_0 \cdot \cos r\,t; \\ \ddot{x}_к = -r^2 \cdot y_{ST} \cdot \cos r\,t - v_0 \cdot r \cdot \sin r\,t. \end{cases} \tag{71}$$

P_{dyn} – the dynamic load applied to the load-carrying device takes the form:

$$P_{dyn} = m_l \cdot \ddot{x}_к = \left(\frac{Q_l}{g}\right) \cdot \{-r^2 \cdot y_{ST} \cdot \cos r\,t - v_0 \cdot r \cdot \sin r\,t\}. \tag{72}$$

If the condition holds: $v_0 >> r{\cdot}y_{ST}$, then from (71) have:

$$P_{dyn} = -\left(\frac{Q_l}{g}\right) \cdot v_0 \cdot r \cdot \sin r\,t. \tag{73}$$

The maximum value P_{dyn} in this case is obtained under the condition:

$$\sin r\,t = -1. \tag{74}$$

This mode and condition are implemented at high initial load lifting speed (v_0). If the ratio: $v_0 << r{\cdot}y_{ST}$, then from (72) have:

$$P_{dyn} = -\left(\frac{Q_l}{g}\right) \cdot r^2 \cdot y_{ST} \cdot \cos r\,t. \tag{75}$$

The maximum value P_{dyn} in this case is obtained under the condition:

$$cos\, r\, t = -1. \tag{76}$$

This mode and condition are implemented at low initial load lifting speed (v_0). In the general case (for arbitrary values of v_0) have:

$$P_{dyn} = \left(-\frac{Q_l}{g}\right) \cdot \left\{\sqrt{{v_0}^2 \cdot r^2 + r^4 \cdot {y_{ST}}^2} \cdot sin(\, rt + \alpha)\right\}, \alpha = arctg\left\{\frac{r \cdot y_{ST}}{v_0}\right\}. \tag{77}$$

The maximum value P_{dyn}, which is equal to:

$$P_{dyn}^{(max)} = \frac{Q_l}{g} \cdot \sqrt{{v_0}^2 \cdot r^2 + r^4 \cdot {y_{ST}}^2}\,, \tag{78}$$

acquires at times t *,determined from the ratio:

$$r \cdot t_n * + arctg\left\{\frac{r \cdot y_{ST}}{v_0}\right\} = \frac{\pi}{2} \cdot (4n-1), n \in N. \tag{79}$$

The full load applied to the load-gripping device is as follows:

$$\begin{gathered} P_{LC} = Q_l + P_{dyn}^{(max)} = Q_l \cdot \left\{1 + \frac{1}{g} \cdot \sqrt{{v_0}^2 \cdot r^2 + r^4 \cdot {y_{ST}}^2}\right\}, \\ {K_d}^{(max)} = 1 + \frac{1}{g} \cdot \sqrt{{v_0}^2 \cdot r^2 + r^4 \cdot {y_{ST}}^2} \end{gathered} \tag{80}$$

and when performing the relation that results in (73), (74), have:

$$P_{LC} = Q_l \cdot \left(1 + \frac{v_0}{g} \cdot r\right) = Q_l \cdot \left\{1 + \frac{v_0}{g} \cdot \sqrt{\frac{C_\kappa}{(m_\kappa + m_l)}}\right\}. \tag{81}$$

Since $C_\kappa = Q_l / y_{ST} = \frac{m_l \cdot g}{y_{ST}}$, then from (81) can be obtained:

$$K_d{}^{(max)} = 1 + \frac{v_0}{g} \cdot \sqrt{\frac{C_\kappa}{(m_\kappa + m_l)}} = 1 + v_0 \cdot \sqrt{\frac{1}{g \cdot y_{ST}} \cdot \left\{\frac{m_l}{(m_\kappa + m_l)}\right\}}. \tag{82}$$

Define further the law of motion $x_\kappa\,(t)$, for which there are no oscillations in the considered system and the initial conditions (70) and the criterion of quality of type motion are performed:

$$\left\{\frac{1}{\tau_p} \cdot \int_0^{\tau_p} (x_\kappa(t))^2 dt\right\}^{1/2} \Rightarrow min. \tag{83}$$

Considering that in (68) $P = const$, condition (83) is performed at (Euler-Poisson equation):

$$x_\kappa{}^{(IV)} = 0. \tag{84}$$

The solution of (84) is sought under the following terminal (initial and final) conditions of lifting the load “with pickup”:

$$x_\kappa(t)|_{t=0} = y_{ST};\ \dot{x}_\kappa(t)|_{t=0} = v_0;\ \ddot{x}_\kappa(t)|_{t=0} = \{(m_l + m_\kappa) \cdot g - C_\kappa \cdot y_{ST}\} = \frac{m_\kappa \cdot g}{(m_l + m_\kappa)};\ \dot{x}_\kappa(t)|_{t=\tau_{II}} = V, \tag{85}$$

where: V – steady-state speed of lifting the load after the transition process ($t \geq \tau_p$).

Search for $x_\kappa\,(t)$, which satisfies equation (84) and conditions (85) in the form of a spline on t:

$$x_\kappa(t) = b_0 + b_1 \cdot t + b_2 \cdot t^2 + b_3 \cdot t^3. \tag{86}$$

Then from (85) have:

$$b_0 = y_{ST};\ b_1 = v_0;\ 2b_2 = \frac{m_\kappa \cdot g}{(m_l + m_\kappa)};\ b_3 = -\frac{2b_2}{3\tau_p}\,, \tag{87}$$

or:

$$x_\kappa(t) = y_{ST} + v_0 \cdot t + \frac{m_\kappa \cdot g}{2 \cdot (m_\kappa + m_l)} \cdot t^2 - \frac{m_\kappa \cdot g}{3\tau_{II} \cdot (m_l + m_\kappa)} \cdot t^3. \tag{88}$$

The dynamism coefficient $K_d\,(t)$ has no oscillating character in the driving mode (88):

$$K_d(t) = \frac{Q_l + m_l \cdot \ddot{x}_\kappa}{Q_l} = 1 + \frac{\ddot{x}_\kappa}{g} = 1 + \frac{m_\kappa}{(m_\kappa + m_l)} \cdot \left(1 - \frac{2t}{\tau_p}\right). \tag{89}$$

Note that its maximum value K_d reaches at the initial moment of time $t = 0$:

$$K_d^{(max)}(t)\Big|_{t=0} = 1 + \frac{m_\kappa}{(m_\kappa + m_l)}. \tag{90}$$

The obtained formulas (in the approximation of a single-mass model of lifting a load “with a pickup”) are quite simple and can be used in practical calculations, although, they do not consider the influence of the second stiffness element that exists in the system under consideration (Fig. 2). Accounting for it, the system should be considered as a biaxial system with two elastic couplings and, accordingly, as having two degrees of freedom of motion, with the corresponding superposition of oscillations at each of the frequencies and finding the maximum during several periods of oscillations. Using the Lagrange function for this problem allows writing in this case the following system of equations for x_l and x_κ:

$$\begin{cases} m_к \cdot \ddot{x}_к + C_к \cdot x_к + C_l \cdot (x_к - x_l) = P_r - Q_l + Q_l = T_{exc} + Q_l;\ T_{exc} = P_r - Q_l;\ Q_l = m_l \cdot g; \\ m_l \cdot \ddot{x}_l - C_l \cdot x_к + C_l \cdot x_l = -Q_l \end{cases}, \quad (91)$$

where: P_r – the driving force of the lifting mechanism drive. Using the second equation of the system (91) can establish that:

$$x_к = \frac{1}{C_l} \cdot (m_l \cdot \ddot{x}_l + C_l \cdot x_l + Q_l). \quad (92)$$

Then, from (92) for $\ddot{x}_к$ have:

$$\ddot{x}_к = \frac{1}{C_l} \cdot \left(m_l \cdot x_l^{(IV)} + C_l \cdot \ddot{x}_l\right). \quad (93)$$

Using the relations (92), (93), the first equation of the system (93) can be reduced to the equation for x_l the fourth order, which is a linear inhomogeneous differential equation:

$$x_l^{(IV)} + \ddot{x}_l \cdot \left\{\frac{C_l}{m_l} + \frac{C_l + C_к}{m_к}\right\} + \frac{C_к}{m_к} \cdot \frac{C_l}{m_l} = \frac{C_l}{m_l \cdot m_к} \cdot \left(T_{exc} - \frac{C_к}{C_l} \cdot Q_l\right), \quad (94)$$

or:

$$x_l^{(IV)} + \ddot{x}_l \cdot \left\{\Omega_l^2 + \Omega_{red}^2\right\} + \Omega_к^2 \cdot \Omega_l^2 \cdot x_l = \Omega_l^2 \cdot \frac{1}{m_к} \cdot \left(T_{exc} - \frac{C_к}{C_l} \cdot Q_l\right), \quad (95)$$

where: $\Omega_l^2 = \frac{C_l}{m_l}, \Omega_{red}^2 = \frac{C_l + C_к}{m_к}, \Omega_к^2 = \frac{C_к}{m_к}$. Here introduced the following designations: C_l – stiffness of hoisting ropes and reduced to them the stiffness of the drive elements, N/m; $\Omega_{red} = \sqrt{\frac{C_l + C_к}{m_к}}$ reduced frequency, 1/s; $C_к$ – stiffness of the metal structure of the crane, N/m; $m_к$ – reduced weight of the metal structure of the crane, kg; m_l – weight of the load, kg [8; 9].

The partial frequencies of this system (in s[-1]) $r_{1,2} \equiv \Omega_{1,2}$ can be obtained from the following relations:

$$\Omega_{1,2} = \left\{\frac{\Omega_l^2 + \Omega_{red}^2}{2} \pm \sqrt{\frac{\left(\Omega_l^2 + \Omega_{red}^2\right)^2}{4} - \Omega_к^2 \cdot \Omega_l^2}\right\}^{1/2}. \quad (96)$$

The duration of the time corresponding to the moment of the detachment of the load from the support (when lifting the load by the "with pickup" method) is obtained from the following transcendental equation [1]:

$$\tau_0 + \left(\frac{C_l}{C_к \cdot \Omega_{red}}\right) \cdot sin(\Omega_{red}\tau_0) = g \cdot \Omega_{red}^2 / \left(v_0 \cdot \Omega_к^2 \cdot \Omega_l^2\right), \quad (97)$$

where: v_0 – speed of lifting the load after its separation from the surface of the support.

Quite often v_0 is identified with V – is the steady-state lifting speed of the load [1; 3], i.e. ($v_0 \approx V$) [3]. Although in the exact analysis of the process of lifting the load by the method "with pickup" v_0 is from (48). Notably, neglect the costs of thermal processes that occur in the deformed foundation during its deformation and detachment of the load from it, i.e. neglect the heat losses that exist in the foundation during the restoration of its original, (almost) undeformed state. At $t > \tau_0$ starts lifting the load by the method "from the weight", which is defined above as a system of equations (4), where $m_r \equiv m_к$. The solution of equation (95) can be given as follows:

$$\begin{cases} x_l(t) = A_1 \cdot sin\,\Omega_1\,t + A_2 \cdot cos\,\Omega_1\,t + A_3 \cdot sin\,\Omega_2\,t + A_4 \cdot cos\,\Omega_2\,t + X*, \\ X* = \frac{1}{C_к} \cdot \left(T_{exc} - \frac{C_к}{C_l} \cdot Q_l\right), \end{cases} \quad (98)$$

and the constants $A_i, i = \overline{(1{,}4)}$, are obtained from the following terminal (initial and final) conditions of lifting the load by the "with pickup" method:

$$x_l(t)|_{t=0} = 0;\ \dot{x}_l(t)|_{t=0} = 0;\ \ddot{x}_l(t)|_{t=\tau_0} = -g;\ \dot{x}_l(t)|_{t=\tau_0} = v_0. \quad (99)$$

From (98), evidently, the load, which is lifted by the method "with a pickup", is inherent in oscillations with partial frequencies, Ω_1, Ω_2,which causes inconvenience and dynamic overloading of the crane rope system during the implementation of the last series of loading and unloading operations [1]. Define what mode of movement x_l (t) can eliminate the above inconveniences. For this, it is required to consider the system of equations (4), (6), which is reduced to equation (7), but for $t > \tau_0$ (when the load has already been detached from the support), with the following terminal (initial and final) conditions of motion (they are valid at the moments of time $t \in (\tau_0, \tau_p)$, where τ_p – the moment of time, when the speed of lifting the load reaches a steady state V, value at which a uniform movement (in particular, lifting) of the load is performed:

$$\xi(t)|_{t=\tau_0} = \frac{Q_l}{C}; \dot{\xi}(t)\Big|_{t=\tau_0} = v_0; \ddot{\xi}(t)\Big|_{t=\tau_0} = \frac{T_{exc}}{m_r}; \ \dot{\xi}(t)\Big|_{t=\tau_p} = V. \tag{100}$$

From equation (7) it can be determined easily $\xi(t)$:

$$\xi(t) = \frac{1}{\Omega^2}\cdot\left\{\left(\frac{Q_l+T_{exc}}{m_r}+\frac{Q_l}{m_l}\right)-\ddot{\xi}\right\}. \tag{101}$$

The following quality criterion (of this movement) will be searched for:

$$\int_{\tau_0}^{\tau_p}\int\{\xi(t)\}^2 dt \Rightarrow min. \tag{102}$$

If you enter a new variable $t* = t-\tau_0$, then the criterion (102) and conditions (100) will be as follows:

$$\begin{cases}\int_0^{\tau_p-\tau_0}\{\xi(t*+\tau_0)\}^2 dt* \Rightarrow min;\\ \xi(t*)|_{t*=0} = \frac{Q_l}{C}; \ \dot{\xi}(t*)\Big|_{t*=0} = v_0; \ \ddot{\xi}(t*)\Big|_{t*=0} = \frac{T_{exc}}{m_r}; \ \dot{\xi}(t*)\Big|_{t*=\tau_p-\tau_0} = V.\end{cases} \tag{103}$$

Using the substitution $\xi(t*+\tau_0)$ (101) and substituting it into the motion quality criterion (102), obtain the necessary condition for the realisation of this criterion (Euler-Poisson equation) of the following form:

$$\xi^{(IV)}(t*+\tau_0) = 0. \tag{104}$$

Consider the solution of this equation in the form of a spline of the third order by the argument $t*+\tau_0 = t$. The same will be for $t* \geq 0$ or $t \geq \tau_0$ to find the solution of the equations accordingly:

$$\xi^{(IV)}(t*) = 0 \tag{105}$$

and:

$$\xi^{(IV)}(t) = 0. \tag{106}$$

Thus, for $\xi(t*)$ have:

$$\xi(t*) = d_0 + d_1\cdot(t*)^1 + d_2\cdot(t*)^2 + d_3\cdot(t*)^3, t* \geq 0. \tag{107}$$

Considering the conditions (103) for $\xi(t*)$ (107), have:

$$\xi(t*) = \frac{Q_l}{C} + v_0\cdot t* + \frac{T_{exc}}{2m_r}\cdot(t*)^2 + \left\{\frac{(V-v_0)-\frac{T_{exc}}{m_r}\cdot(\tau_{II}-\tau_0)}{3\cdot(\tau_p-\tau_0)^2}\right\}\cdot(t*)^3. \tag{108}$$

The dynamic component of the force that occurs in the rope system when lifting a load "with a pickup" has the following form:

$$P_{LC}(t*) = C\cdot\xi(t*) = Q_l + C\cdot v_0\cdot t* + \frac{C\cdot T_{exc}}{2m_r}\cdot(t*)^2 + C\cdot\left\{\frac{(V-v_0)-\frac{T_{exc}}{m_r}\cdot(\tau_p-\tau_0)}{3\cdot(\tau_p-\tau_0)^2}\right\}\cdot(t*)^3. \tag{109}$$

The dynamism coefficient $K_d(t*)$ has the following form:

$$K_d(t*) = \frac{P_{LC}(t*)}{m_l\cdot g} = 1 + \frac{C\cdot v_0\cdot(t*)}{m_l\cdot g} + \frac{C\cdot T_{exc}}{2m_r\cdot m_l\cdot g}\cdot(t*)^2 + \frac{C\cdot\left\{(V-v_0)-\frac{T_{exc}}{m_r}\cdot(\tau_p-\tau_0)\right\}}{m_l\cdot g\cdot 3\cdot(\tau_p-\tau_0)^2}\cdot(t*)^3. \tag{110}$$

From (110) evident that $K_d(t*)$ it has no oscillatory character. The maximum value this value acquires at $t* = \tau_p-\tau_0$, namely:

$$K_d{}^{(max)}(t*) = K_d(t*)|_{t*=\tau_p-\tau_0} = 1 + \frac{2C\cdot v_0\cdot(\tau_p-\tau_0)}{3\cdot m_l\cdot g} + \frac{C\cdot V\cdot(\tau_p-\tau_0)}{3\cdot m_l\cdot g} + \frac{C\cdot T_{exc}\cdot(\tau_p-\tau_0)^2}{6m_r\cdot m_l\cdot g}. \tag{111}$$

As a rule: $\tau_p >> \tau_0$, $V\approx v_0$, thus from (111) have:

$$K_d{}^{(max)}(t*)\Big|_{t*=\tau_p} = 1 + \frac{C\cdot V\cdot\tau_p}{m_l\cdot g} + \frac{C\cdot T_{exc}\cdot\tau_p{}^2}{6m_r\cdot m_l\cdot g}. \tag{112}$$

Due to the small values of the terms included in (112), compared to unity, practically the value of the dynamism coefficient for this method of lifting the load (as, incidentally, for the case of lifting the load "from weight") differs little from unity (not more than 10%, exceeding unity).

Discussion

The quality of operation and functioning of the lifting mechanisms of bridge cranes largely depends on the proper optimisation of the dynamic loads of rope systems due to the handling of goods, and their efficiency is one of the most pressing issues of our time, and some problems require immediate solutions. For example, the mechanisms with which it can be performed installation and transporting works are quite dangerous and cumbersome during operation, this is a significant problem in using these mechanisms, and it is essential to increase the efficiency of exploring these problems to solve them as soon as possible. Most of the lifting mechanisms at the moment are outdated both technically and morally, and the significant amount of resource cranes has greatly decreased.

According to the results of recent studies by Q. Guo et al. [24], the constant use of lifting machines in such a technically worn-out condition can result in their destruction and breakdowns, which causes the termination of the cargo flows used by them. On the one hand, the provision of high productivity of shifting loads in the river and sea warehouses, ports, construction sites, and production workshops is combined with increased dynamic loads in the details of cranes, they are one of the main reasons for their transition to the limiting environment, after which the efficient and high-quality operation of the mechanism is unrealistic. The most urgent issue that must be considered during the development and operation of the cargo lifting facility is the energy efficiency of this mechanism.

The entire mechanism of lifting machines was analysed, and as a result, it was decided that for the application of various constructions, especially theoretical ones, it is necessary to have a basic knowledge of these objects to indicate the physical properties of this device and their number, which will allow understanding the process of operation of lifting mechanisms under the given conditions of their use. The problem of energy efficiency of lifting mechanisms was almost indecisive before, as there were not enough available means of energy saving in the crane drive, and they appeared recently. Complex vibrations have an adverse impact on the stability of the elements of lifting machines, which results in numerous destructions.

According to the definition of H.M. Omar et al. [25], gantry cranes are most often used for the construction of civil and industrial facilities. The features of operation of these lifting mechanisms are that a large part of the work process is represented by transient modes, namely starting and deceleration, machines for changing the departure and lifting loads. Thus, the productivity of the crane is connected with the duration of the transitional processes of the machines for changing the outreach and lifting loads.

It indicates that in the design and modelling of gantry cranes used for the construction of various structures, it is required to consider all the features of the mechanism and its modes that affect the quality of operation and ensure proper performance. Efforts to reduce the duration of transients in the departure change machine are not successful due to the necessity to reduce the load fluctuations that occur during transients. All these damages the operational performance and reliability of gourd cranes, and, in general, lifting and transporting mechanisms.

Researcher Y. Liu [26] determined that there are almost no systems for monitoring the energy consumption of lifting mechanisms in Ukraine, although lifting machines, compared to other industrial equipment and mechanisms, have low efficiency and are one of the most energy-efficient mechanisms. Very large energy losses in crane electric drives occur through the outdated control systems of drives, inefficient cycles of operation of machines, and their worn-out technical condition. In general, this applies to 80% of cranes that have reached the end of their regulatory service life.

But when modelling lifting mechanisms and other industrial equipment, using this class of energy consumption monitoring systems, allows for improving the work of these machines, due to the massive number of receiving elements and the large number of parts that are involved in the process, thus, it is very necessary to consider the specific features of using this type of mechanisms and systems, timely investigation of data and possible causes of problems, for further prospective development of using lifting machines and monitoring systems in Ukraine. It is essential to draw attention to the development of systems for monitoring the energy consumption of cranes, considering the regulatory requirements for their safe operation. To improve the reliability of the operation of lifting mechanisms, it is required to reduce the dynamic loads on their body and drive parts.

C.M. Niu et al. [27] identified that the cost of energy resources is constantly increasing, which optimises research to reduce energy consumption when lifting or lowering loads. Suboptimal and unreliable choices of cycles of operation of the lifting machine, even in the presence of innovative hardware, can cause energy overruns during the unloading and loading processes. The investigation and resolution of these contradictions can be promising only using the mechatronic approach, through which lifting mechanisms are presented as a synergistic combination of electrical, hydraulic, mechanical and electronic components.

The results of this mechatronic approach to resolving contradictions were analysed and explored more precisely, it can be concluded that the efficiency of using innovative designs of lifting mechanisms and support apparatus, their use allows for keeping energy overrun. The main role in the modelling and design of mechatronic crane systems is the development and calculation of software that allows the implementation of control of some individual mechanisms, devices and parts. During start-up and deceleration of drive devices, i.e. transient modes, dynamic loads dangerous for lifting mechanisms appear.

M. Ziaei et al. [28] demonstrated that such transient modes in cranes have an impact on the energy and dynamic properties and performance of the crane. For a load-lifting machine, the dynamic cycles that occur during the transitional modes of movement, i.e. lifting or lowering the load, have an impact on the magnitude of the moment and force loads in the flexible suspension and drive of the machine. The vibrations in the flexible suspension are transferred to the crane boom and load it with additional bending moments.

These modes may have a specific modification, it happens due to the specific features of the cranes that are observed and considered. It is essential to use the tower crane in such a way that the oscillatory dynamic cycles in its mechanisms are reduced during transient modes of movement. Small elimination of dynamic loads during the start-up and deceleration of gourd cranes helped to increase the overhaul time of these cranes many times.

As noted by N. Zhao et al. [29], modern monitoring systems operate on the established mechanism link between the replacement of energy losses during the operation of lifting mechanisms, namely cranes, and their technological condition. At the time of operation of cranes, it changes a lot: the position of the crane runway, flanges and rims of the running wheel, brake linings, brake pulleys, rope block, drum, bearing and various friction units in crane machines, the position of the electric motor winding and the resistance of the separate relay and contact equipment, the electromagnetic pusher coil, the viscosity of the operating emulsion in gearboxes and electrohydraulic brakes. Thus, as a result of these work processes, the energy consumption of lifting mechanisms changes.

To optimise the energy performance of lifting mechanisms and their electric drives, dynamic loads and kinematic parameters of cranes, it is required to develop mathematical models that can consider transient cycles in lifting electric drives, structural vibrations, loosening of loads and represent a set of non-linear differential equations. It is essential to increase funding and improve the skills of employees, to start introducing new technologies to improve the design and modelling of lifting machines and to reduce errors in the operation of these mechanisms.

Conclusions

The physical-mechanical models for the analysis of the process of lifting loads by overhead cranes in two ways are substantiated: "from weight" and "with pick-up"/"from the base". The laws of motion of the elements of these models within the one- and two-mass calculation schemes are determined, which allows for avoiding fluctuations of the load and significantly (in some cases, several times) reducing the value of the dynamism coefficients. In the future, it is essential to improve, according to the authors of this work, the investigation of the processes of lifting loads by overhead cranes in various ways by considering the discrete-continuous properties of systems and lifting mechanisms designed for this purpose, and to improve control processes through using modern mechatronic control systems.

The main problems of increasing the efficiency and optimisation of dynamic loads of rope systems of lifting mechanisms of overhead cranes during cargo handling are mediocre training, problems of proper modelling and design of monitoring systems, multiple errors in the preparation for the operation of lifting machines, these problems are and will be relevant and require further investigation. The obtained results demonstrate that it is essential to be able to eliminate uncertainties in the process of functioning lifting machines if a specific scheme and rules are followed when operating the lifting mechanisms of overhead cranes. In this research, the purpose of the study was achieved, namely, the dynamic loads that arise in the rope systems of lifting machines of bridge cranes during start-up and deceleration were analysed, and efficient ways to help reduce these loads were found, the magnitude and nature of changes in dynamic loads in the elements of the lifting mechanisms of bridge cranes were identified, a comprehensive dynamic analysis of the lifting mechanisms of the bridge crane and its elastic elements was performed. To improve these mechanisms in the country, it is essential to increase the use and development of lifting machines, especially overhead cranes. In addition, it is necessary to draw attention to the quality of the elements and introduce newly developed methods for their quality development.

References

[1] Novak SM, Logvinets AS. 1990. Vibration and noise protection in construction. Kyiv: Budivelnik; 1990.

[2] Vaynson AA, Andreyev AF. 1982. Crane lifting devices. Moscow: Engineering; 1982.

[3] Goberman LA, Stepanyan KV, Yarkin AA, Zalenskiy VS. 1979. Theory, design and calculation of construction and road machines. Moscow: Engineering; 1979.

[4] Loveykin VS, Chovnyuk YuV, Dikteruk MH, Pastushenko SI. 2004. Modeling of the dynamics of mechanisms of lifting machines. Kyiv: Kyiv National University of Construction and Architecture; 2004.

[5] Loveykin VS, Romasevych YuO. Optimization of transient modes of motion of mechanical systems by the direct variational method. *B. of the Tern. Nat. Techn. Univ*. 2010;(15(1)):7-13.

[6] Loveykin VS, Romasevych YuO. Analysis and synthesis of movement modes of mechanisms of lifting machines. Kyiv: Comprint; 2012.

[7] Romasevych Yu, Loveykin V. Synthesis of optimal movement control of cargo cranes. *Min., Constr., Road and Reclam. Mach*. 2014;(83):26-33.

[8] Loveykin VS, Romasevych YuO. Synthesis of optimal motion control of dynamic systems by the integral-terminal criterion. *Collec. of Sc. Wor. of the Poltava Nat. Techn. Univ. named after Y. Kondratyuk*. 2012;(1):67-73.

[9] Loveykin VS, Romasevych YuO. Complex synthesis of optimal control of the movement of a cargo crane. *Aut. of Prod. Proc. in Mech. Engin. and Instr. Engin*. 2011;(45):385-399.
[10] Loveykin VS., Romasevych YuO. Justification of the introduction of a modified restriction on the function of optimal control of technical systems. *Constr., Mater. Sc., Mech. Engin*. 2011;(63):211-220.
[11] Loveykin VS, Romasevych YuO. Analysis and synthesis of optimal control of the movement of a cargo-lifting crane by the direct variation method. *Sc. B. of the Nat. Univ. of Bior. and Nat. Manag. of Ukraine*. 2014;(196(1)):129-139.
[12] Loveykin VS. Calculations of optimal modes of movement of mechanisms of construction machines. Kyiv: UMK; 1990.
[13] Loveykin VS, Romasevych YuO. Dynamic optimization of the load lifting mechanism of bridge cranes. Kyiv: Comprint; 2015.
[14] Loveykin VS, Romasevych YuO, Chovnyuk YuV, Kadykalo IO. Dynamics and optimization of lifting and transporting machines. Kyiv: Comprint; 2019.
[15] Loveykin VS, Romasevych YuO. Optimizing the movement modes of crane mechanisms. Nizhin: M.M. Lysenko; 2011.
[16] Loveykin VS, Romasevych YuO, Chovnyuk YuV. Application of variational calculus methods in optimal management of agricultural lifting machines. *Lift. and Tran. Equip*. 2010;(2(34)):3-15.
[17] Loveykin VS., Romasevych, Yu.O. 2011. Optimal control of the motion of dynamic systems taking into account higher derivatives of the control function. *Scientific Bulletin of the National Forestry University of Ukraine*, 21(15), 304-312.
[18] Loveykin, VS, Voytyuk DH, Romasevych YuO, Chovnyuk YuV. Development of mechatronic systems for controlling the movement of a crane mechanism with a flexible load suspension. Kyiv: Agrarian Education; 2011.
[19] Loveykin VS. 1998. Minimization of dynamic loads in elastic elements of lifting machines. *Min., Constr., Road and Reclam. Mach.* 1998;(52):63-68.
[20] Hekman K, Singhouse WE. A feedback control system for suppressing crane oscillations with on – off motors. *Intern. Jour. of Cont. Autom. and Sys*. 2007;(5(3)):223-233.
[21] Loveikin VS., Romasevych YO. Dynamic optimization of a mine winder acceleration mode. *Sc. B. of the Nat. Min. Univ*. 2017;(4):55-61.
[22] Loveikin VS, Chovniuk YuV, Liashko AP. The crane's vibrating systems controlled by mechatronic devices with magnetorheological fluid: The nonlinear mathematical model of behavior and optimization of work regimes. *Sc. B. of the Nat. Min. Univ*. 2014;(6):97-102.
[23] Grigorov O, Druzhynin E, Anishchenko G, Strizhak M, Strizhak V. Analysis of various approaches to modelling of dynamics of lifting-transport vehicles. *Inter. J. of Engin. & Tech*. 2018;(7(4.3)):64-70.
[24] Guo Q, Chai L, Liu H. Anti-swing sliding mode control of three-dimensional double pendulum overhead cranes based on extended state observer. *Nonl. Dynam*. 2022;(1):1-20.
[25] Omar HM, Akram R, Mukras SM, Mahvouz AA. Recent advances and challenges in controlling quadrotors with suspended loads. *Alex. Engin. J.* 2022;(63):253-270.
[26] Liu Y. Research on flexible unloading method for dynamic compaction. *J. of Buil. Engin.* 2021;(44):article number 103359.
[27] Niu CM, Zhang HW, Ouyang H. A comprehensive dynamic model of electric overhead cranes and the lifting operations. *Proc. of the Inst. of Mech. Engin., Part C: J. of Mech. Engin. Sc.* 2021;(2266):1484-1503.
[28] Ziaei M, Choobineh A, Ghaem H, Abdoli-Eramaki M. Evaluation of a passive low-back support exoskeleton (Ergo-Vest) for manual waste collection. *Ergon*. 2021;(6410):1255-1270.
[29] Zhao N, Liu Y, Mi W, Shen Y, Xia M. Digital management of container terminal operations. Singapore: Springer; 2020.

Оптимізація динамічних навантажень канатних систем вантажопідйомних механізмів мостових кранів при обробці вантажів

Юрій Васильович Човнюк[1], Любов Анатоліївна Дяченко[2], Євген Олександрович Іванов[3], Наталія Петрівна Дічек[2], Ольга Володимирівна Орел[4]

[1]Національний університет біоресурсів і природокористування України
03041, вул. Героїв Оборони, 15, м. Київ, Україна

[2]Відокремлений структурний підрозділ «Ніжинський фаховий коледж Національного університету біоресурсів і природокористування України»
16600, вул. Т. Шевченка, 26, м. Ніжин, Україна

[3]Національний авіаційний університет
02000, просп. Любомира Гузара, 1, м. Київ, Україна

[4]Інститут педагогіки Національної академії педагогічних наук України
04053, вул. Січових стрільців, 52-Д, м. Київ, Україна

Анотація.

Актуальність. У даному дослідженні приділена значна увага аналізу динамічних навантажень, які виникають у канатних системах вантажопідйомних механізмів мостових кранів під час пуску та гальмування, а також зменшенню цих навантажень.

Мета. Для виявлення величини та характеру зміни динамічних навантажень у елементах вантажопідйомних механізмів мостових кранів проведений всебічний динамічний аналіз саме механізму підйому мостового крану та його пружних елементів (канатних систем).

Методи. Динамічний аналіз вказаних вище механізмів та систем проведено на обґрунтованих математичних моделях кранів мостового типу (одно- та двомасових).

Результати. Аналіз отриманих розрахунків математичних моделей механізму підйому вантажу мостових кранів показав, що динамічні навантаження, які діють на елементи конструкцій та приводних механізмів, мають коливний характер і по величні співставлені зі статичними навантаженнями. Тому для зменшення динамічних навантажень в елементах конструкцій (зокрема, у канатах) під час перехідних процесів у таких вантажопідйомних механізмах мостових кранів запропоновано провести оптимізацію режимів руху їх приводних механізмів. Для мінімізації інтегральних функціоналів використовувались методи класичного варіаційного числення, математичної фізики та диференціальні рівняння, які моделюють динаміку процесів навантаження канатних систем та приводів мостових кранів, а також були враховані термінальні (початкові та кінцеві умови руху подібних систем), що дозволило однозначно розв'язати оптимізаційну задачу. Важливе місце в такій оптимізації займає вибір критерію оптимізації. Серед таких критеріїв використовувались інтегральні критерії оптимізації. У якості таких інтегральних критеріїв оптимізації використовувались середньоквадратичні значення діючих навантажень у пружних елементах (канатах) мостових кранів.

Висновки. Такі інтегральні критерії являють собою інтегральні функціонали, які, як правило, відображають небажані властивості машин та їхніх механізмів, тому вони підлягають мінімізації

Ключові слова: динамічна оптимізація, канатні системи, вантажопідйомні механізми, мостові крани, обробка вантажів, перехідні процеси

Scientific Herald of Uzhhorod University Series “Physics”

Journal homepage: https://physics.uz.ua/en

Issue 51, 74-82

Received: 18.04.2022. Revised: 31.05.2022. Accepted: 20.06.2022

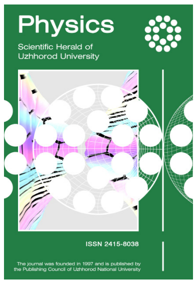

UDC 533
PACS 87.15.K
DOI: 10.54919/2415-8038.2022.51.74-82

Alternative Representation of Space and Time: Geometric Solution of Problems of Relativity Theory

Iurii M. Shynkariuk*

Research and Production Enterprise “Silverhorst”

04071, 26 Vvedenska Str., Kyiv, Ukraine

Abstract

Relevance. The relevance of the stated subject of this scientific research is due to the importance of theoretical issues of alternative representation of the categories of space and time from the point of view of developing geometric solutions to problems of relativity theory, which are important in solving numerous practical issues encountered in various fields of modern science and technology.

Purpose. The purpose of this research work is to form an alternative view of the categories of space and time, which are of significant practical importance for creating geometric solutions to problems that reflect certain principles of the theory of relativity.

Methods. The basis of the methodological approach to the construction of research works in this scientific study was a combination of a systematic analysis of the features of compiling an alternative representation of the categories of space and time with an analytical study of the features of constructing geometric solutions to problems that reflect various problematic aspects of the general theory of relativity.

Results. The results of this research work reflect the entire course of scientific research, and indicate the absence of contradictions in the very fact of the existence of alternative space-time models, as not meeting the fundamental principles of the special theory of relativity.

Conclusions. The results and conclusions of this research have significant practical significance from the point of view of forming new ideas about the provisions of the special theory of relativity and the possibilities of practical use of geometric models to solve complex problems of this theory, through the use of corrected ideas about the real properties of space and time, and are also of significant importance for employees of design bureaus engaged in the development of the latest samples of high-tech equipment and using the principles of special relativity in their calculations

Keywords: physical theories, space, geometric aspects, science, scientific concepts

Suggested Citation:
Shynkariuk IuM. Alternative representation of space and time: Geometric solution of problems of relativity theory. *Scientific Herald of Uzhhorod University. Series “Physics”.* 2022;(51):74-82.

*Corresponding author

Introduction

According to numerous scientific publications concerning the role and place of the theory of relativity in the world scientific paradigm, there are many scientists who almost unconditionally accept this theory, without casting any doubts on it [1]. In addition, there are scientific studies that declare the very conditions of the problem statement to be far-fetched (over-idealized) and the possibilities of observing specific events, as well as the paradoxes that occur (in particular, the "clock paradox"), to be unrealistic. The concepts of "space" and "time" raise many questions, and the latter criterion attracts the most attention, becoming periodically the object of fierce disputes. The situation is eloquently illustrated by the thesis of Aristotle, who called time the most "unknown" of the entire unknown.

Numerous ideas about the attitudes of various ancient peoples and civilizations reach us today from the depths of centuries. In particular, of particular interest is the study of symbols conducted by the ancient Sumerians and devoted to the study of a six-pointed star [2]. From the Sumerian civilization, this symbol passed to Egypt, after which it came to the Jews, being now known as the "Star of David". In this context, it is noteworthy that the original interpretation of this symbol of two united equilateral triangles was the unity of three-dimensional space and the same three-dimensional time. The connection of space-time turns out to be six-dimensional!

The four-dimensional model of time and space, better known as the Minkowski model, by analogy with the three-dimensional space of classical physics, has an absolute character. In a way, the Minkowski spatial model can be regarded as an extrapolation of the absolute three-dimensional Euclidean space to an additional dimension [3]. Therefore, such criteria as uniformity and isotropy can characterize this space in four dimensions, if we do not take into account the boundaries set by the cone of light. In the SRT, space-time is passive, since not all bodies and fields have a counter effect on it, being located and moving in this space-time.

In the Minkowski space, concepts such as simultaneity or different timing of events are interpreted from the position of observers (for example: A and B), which move relative to each other [4]. To facilitate perception as much as possible, we will consider a straight horizontal line containing many objects at a particular time usually denotes a two-dimensional model of space-time, which lends to visual representation in the drawing plane, despite that one-dimensional space, and a straight vertical line denotes one-dimensional time. Lines that show the position of an object at certain time intervals are the trajectories of objects moving directly in space-time. Lines located at a certain angle of inclination display the trajectories of moving objects. At the same time, it should be taken into account that all events were located on the same horizontal line that occurred at the same time. Other events were on the same line that took place in the same place, located strictly vertically. All these geometric images are called world lines of the trajectories of moving and resting objects in space-time [5]. Any of the points of the world lines should be perceived as an event in space at a specific time interval.

The lack of geometric models for solving problems of relativity theory, capable of clarifying the issue under study, was the main problem of scientific research of alternative representations of space and time. This scientific research sets to expand alternative ideas about the properties of space and time, using a wide range of possibilities for solving problems of the theory of relativity by geometric methods.

Materials and methods

This research is based on the methodological approach, which includes an alternative systematic analysis of space and time and an analytical study of geometric solutions to problems reflecting various problematic aspects of the general theory of relativity. The study of the features of geometric solutions to problems reflecting the problematic aspects of general relativity involves the construction of graphical representations of various kinds of events that are important in the context of displaying the basic laws that affect the expansion of alternative representations regarding the parameters of space and time from the point of view of the principles of relativity theory.

The theoretical basis of this research work is numerous studies by Ukrainian and a number of international scientists that reflect various aspects of constructing geometric solutions to problems of relativity theory that are of significant practical importance in the context of the development of alternative ideas about the properties of space and time. Thus, the theoretical basis of this scientific work was selected and compiled in strict accordance with the stated topic and should contribute to its maximum qualitative disclosure.

This scientific research was carried out in several main stages.

At the first stage of this research, a theoretical study was carried out of available publications in Ukrainian and international sources devoted to the study of the properties of space and time in the context of the general theory of relativity, which generally contributes to a qualitative theoretical basis for further research. In addition, at this stage of scientific research, an alternative systematic analysis of space and time was carried out, which lays the groundwork for further scientific research and combined with the accumulated theoretical base.

At the second stage of this research, an analytical study was carried out of geometric solutions to problems reflecting various problematic aspects of the general theory of relativity. This study included graphical dependencies of different events that are important in the context of the main patterns affecting the expansion of alternative representations regarding the parameters of space and time from the point of view of the principles of relativity theory. In addition, at the second stage of this scientific study, an analytical comparison was carried out of the results obtained during it with the results and conclusions of other researchers on alternative ideas about the properties of space and time in the context of the general theory of relativity, which generally contributes to objective ideas about the results obtained in this scientific study.

At the final stage of this scientific research, during it, the conclusions were formulated based on the obtained results, acting as their logical reflection and summing up the entire spectrum of scientific research that was carried out in this work. The results of the study of alternative ideas about the properties of space and time through the geometric solution of the problems of relativity theory and the conclusions formulated on their basis can serve as a qualitative foundation to continue scientific research.

Results

The scientific study of the possibilities of forming alternative representations regarding the properties of the categories of space and time by creating geometric solutions to problems of relativity theory has resulted in the following.

When creating geometric solutions, special attention should be paid to the units of measurement used [6]. In particular, space is divided into equal segments that turn out to be multiples of the length nl_{Pl}. At the same time, time is divided into equal segments, which turn out to be multiples of the Planck time nt_{Pl}.

The travel speed of objects should be taken in parts of the speed of light $\boldsymbol{c}$. Because:

$$c = lPl/tPl, \qquad (1)$$

then the value of the speed in two-thirds of the speed of light in the presented figures will have the form:

$$V = (2/3)\mathrm{c} = (2\,nlPl)/(3\,ntPl). \qquad (2)$$

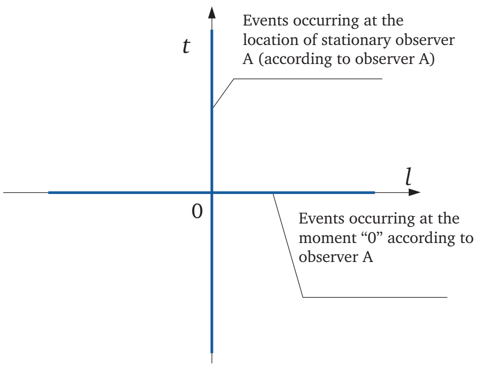

Figure 1. Two-dimensional space-time model
Source: developed by the author

Figures 2 and 3 show the trajectories of objects represented as inclined lines. Simultaneously occurring events are reflected on the horizontally located straight line, while events that occurred in the same place are spread out on the vertical straight line.

When the observer B is moving at a speed V=(2/3) c from the distance between points 0 and K_b will be the value Δ_B when B meets with the observer A, as shown in Figure 4. Also, it follows from this figure that all linear dimensions will not be identical of the system of moving observer B (in the direction of movement), in projection onto the space of stationary observer A, (the projection of the linear size of the moving system $(t_B;l_B)$ on the stationary one $(t_A;l_A)$ must uniformly decrease) because the linear dimensions of stationary observer A will be significantly smaller than the actual ones for moving observer B. A comparison of calculations of relativistic reduction of lengths and simple geometric parameters do not provide full and equivalent values Δ_A (distance from 0 to K_A).

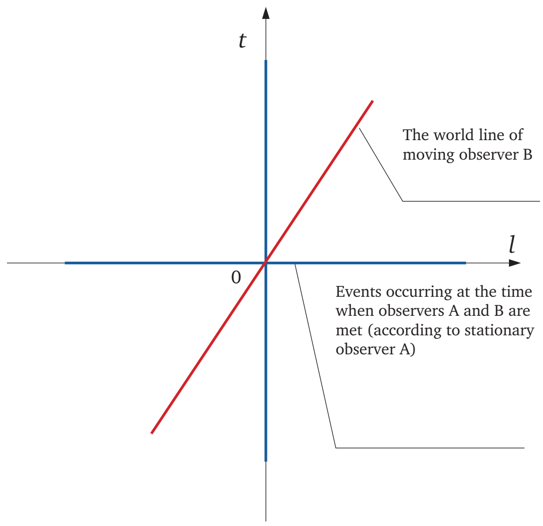

Figure 2. The inclined line is the trajectory of objects
Source: developed by the author.

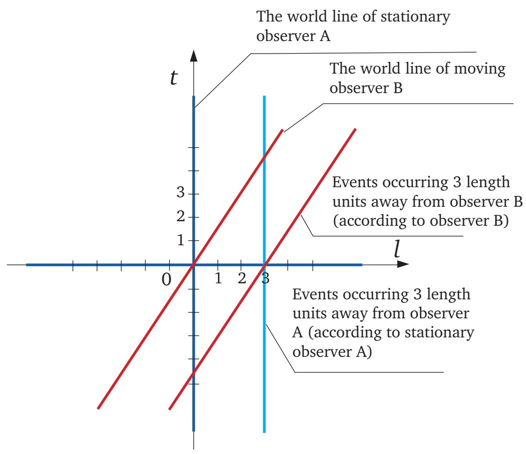

Figure 3. The inclined line is the trajectory of objects
Source: developed by the author

The laws of physics apply equally in all systems where rectilinear and uniform motion takes place. For this reason, the system of observer B should be considered as stationary. In such a state of affairs, the world line of moving observer B coincides in the system of stationary observer A with the time axis in the system of observer B (as shown in Fig. 4), and the spatial axis is perpendicular to the time axis.

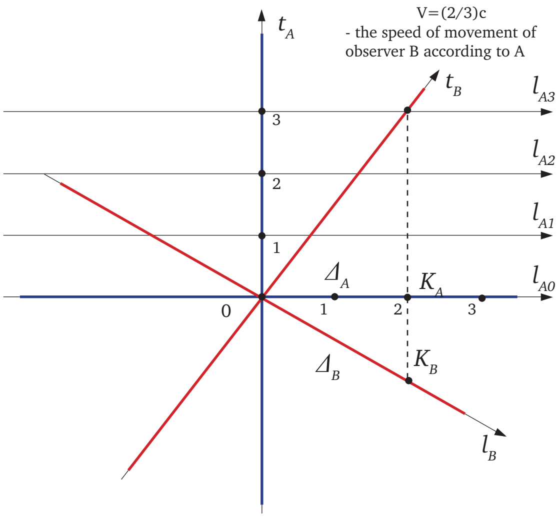

Figure 4. Coincidence of axes and observation systems A and B
Source: developed by the author

Figure 5 shows the movement of observer B relative to the location of observer A with the same velocity V=(2/3) c. The front of a flash of light displays the passage of time on the plane; within one plane it has the form of concentric circles, the radius of which is equal to

$$R\,n = R\,n - 1 + 1\,tu, \tag{3}$$

and the center is located at the reference point 0, which simultaneously acts as the beginning of measurements and the meeting point. Since $c=l_{Pl}/t_{Pl}$ and any of the units of length is a multiple of the Planck length in Figure 5, and the unit on the conditional axis of time (radius of the sphere) is a multiple of the Planck time, then graphically it is necessary to mark the same single segments on the axes of length and time values.

The location of the world line of the observer B in motion is completely superimposed on the conditional time axis, so this world line passes directly through the point of contact of the two observers O, as well as the point T_B. The latter indicates the place where observer B is located, moving relative to observer A at a speed of V=(2/3) c, after passing two units of length in 3 units of time since their meeting.

Figure 5 can be modified somewhat by moving the center of the coordinate system of observer B to the center of the coordinate system of observer A, as shown in Figure 6. Such a combination does not change the essence of the matter at all, while simplifying the understanding of the situation [7]. From the data presented in Figure 6, it follows that observer A will be at point T_{AB} when observer B (in his opinion) will be at point T_B. In other words, the events T_{AB} and T_B do not differ in time at all for observer A. For observer B, the events T_B and T_{BA} occur simultaneously. Events L_A and L_B occur at the same time and spatial distance for observer A.

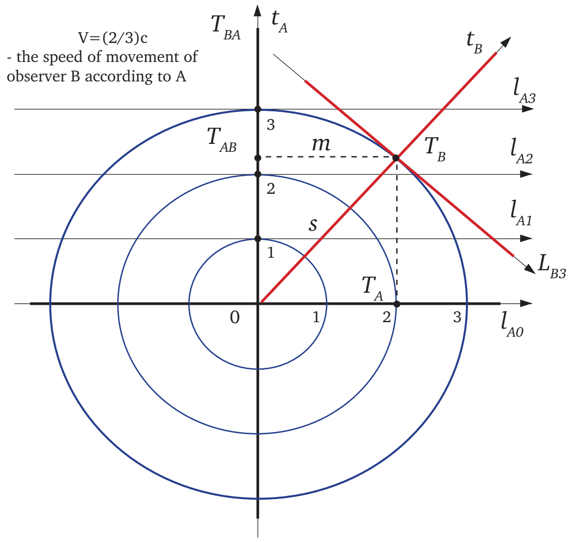

Figure 5. Moving observer B relative to the location of observer A
Source: developed by the author

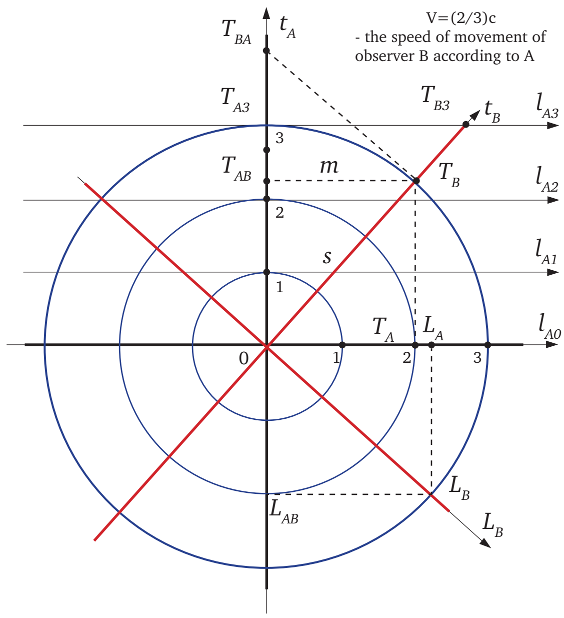

Figure 6. Combining the centers of the coordinate systems of observers A and B
Source: developed by the author

Geometric transformations according to Figure 6 have the following form:

$$V = \frac{2}{3}c = \frac{m}{s}c; \quad (4)$$

$$t = s = \frac{m}{V}c; \quad (5)$$

$$l = m = \frac{Vs}{c}. \quad (6)$$

Consider geometrically identical triangles $\Delta\, OT_{AB}\, T_B$ and $\Delta\, OL_A\, L_B$,

$$\Delta \mathrm{OT}\ AT\ B \ and\ \Delta\ OL\ AB\ L\ B. \quad (7)$$

Because

$$|OL\ A/=/L\ AB\ L\ B|, \quad (8)$$

that

$$|OLA| = \sqrt{|OL_B|^2 - |OL_{AB}|^2} = \sqrt{s^2 - m^2} \quad (9)$$

$$|OL\ A| = \sqrt{3^2 - 2^2} = 2{,}236\ units, \quad (10)$$

This corresponds to the linear parameters in Figure 6 and the relativistic reduction of the longitudinal linear dimension in a dynamic system (from the position of a static observer A).

After converting formula (9), the right part is substituted into it, under the value of the root $(V = \frac{m}{s}c)$:

$$|OLA| = \sqrt{(\frac{m}{V}c)^2 - (\frac{Vs}{c})^2} = \sqrt{\frac{m^2c^2}{V^2} - \frac{V^2s^2}{c^2}} = \sqrt{\frac{m^2c^2s^2}{m^2c^2} - \frac{V^2s^2}{c^2}} = \sqrt{s^2 - s^2\frac{V^2}{c^2}} = \sqrt{s^2(1 - \left(\frac{V}{c}\right)^2)} = s\sqrt{1 - \left(\frac{V}{c}\right)^2} \quad (11)$$

As a result, we have the formula:

$$|OLA| = s\sqrt{1 - \left(\frac{V}{c}\right)^2}. \quad (12)$$

This formula is identical to the formula of the special theory of relativity obtained to describe the relativistic effect of reducing the longitudinal linear parameters of a moving system from the position of an observer at complete rest.

The presented logic of scientific research is applicable to calculate the deceleration rate of the running clock. If we assume that moving observer (Fig. 6) B will not be able to change the work of its watches in point T_B , but can see the acceleration of watches of static observer A directly at the point of its stay T_{BA} (as events T_B and T_{BA} occur in one and the same time from the perspective of observer B). At point T_{A3}, static observer A will be able to note an increase in the clock speed of observer B at point T_{B3} (since both events T_{A3} and T_{B3} take place at the same time, from the position of static observer A). Everything is logical, due to the inertia of the systems under study and the similarity of the flow of all physical processes that take place in them [8].

The course of the clock can be output as follows, according to the data presented in Figure 6:

$$|T\ ABT\ B| = m; \quad (13)$$

$$|OT\ B| = s = tA; \quad (14)$$

$$|OT\ AB| = t\ B; \quad (15)$$

Consider similar triangles $\Delta\, OT_{AB}\, T_B$ and $\Delta\, T_B\, T_{AB}\, T_{BA}$, for which the following algebraic relations can be considered valid:

$$|OT\ AB| = \sqrt{s^2 - m^2}, \quad (16)$$

$$\frac{|T_{AB}T_{BA}|}{|T_{AB}T_B|} = \frac{|T_{AB}T_B|}{|OT_{AB}|}, \quad (17)$$

$$|T_{AB}T_{BA}| = \frac{|T_{AB}T_B||T_{AB}T_B|}{|OT_{AB}|} = \frac{m^2}{\sqrt{s^2-m^2}}, \quad (18)$$

$$|OT_{BA}| = |OT_{AB}| + |T_{AB}T_{BA}|, \quad (19)$$

$$|OT_{BA}| = \sqrt{s^2 - m^2} + \frac{m^2}{\sqrt{s^2-m^2}} = \frac{1}{\sqrt{s^2-m^2}}(s^2 - m^2 + m^2) = \frac{s^2}{\sqrt{s^2-m^2}}. \quad (20)$$

All substitutions and abbreviations are performed in strict and complete accordance with the previous calculation:

$$\frac{s^2}{\sqrt{s^2-m^2}} = \frac{s^2}{s\sqrt{1-\left(\frac{V}{c}\right)^2}} = \frac{s}{\sqrt{1-\left(\frac{V}{c}\right)^2}} = \frac{t_A}{\sqrt{1-\left(\frac{V}{c}\right)^2}}. \quad (21)$$

The result will be a formula for the sequence of relativistic deceleration of the clock mechanism:

$$t_B = \frac{t_A}{\sqrt{1-\left(\frac{V}{c}\right)^2}} \quad (22)$$

Thus, the fundamental principles of special relativity in the context of creating an alternative space-time model work and can be clearly demonstrated. This fact testifies to the fundamental possibility of creating an alternative model of the space-time characteristics of a physical object that does not conflict with the principles of special relativity. This is extremely important from the point of view of understanding space-time relationships and contributes to a general improvement in the understanding of modern concepts of constructing alternative models of space and time for their use to assess the quality of physical processes occurring in various spheres of modern scientific and social life.

Discussion

The invariance of the well-known equations of electrodynamics in relation to a specific group of transformations should be in constant, close connection with the various characteristics of transformations of partial differentials of the parameters of space and time. In the event that a connection of this kind will have observable consequences, then they can be expressed in certain problems of electrodynamics of bodies in a state of constant motion, despite the fact that the radiation source, the receiver, the interface of the media, as well as the media themselves move at very different speeds. In this context, there is a substantial interest in the experimental verification of the electrodynamic equations in the two- or three-dimensional case of displacements in the medium, taking into account the dispersion parameters [9].

Now, there are enough theories that are not at the forefront of modern science, moreover, today science has grown so much that millions of scientists are not able to fully grasp and comprehend it. Not all scientific questions have answers, even though science can put forward one answer option for the public and at the same time have several spare ones that determine the directions of subsequent scientific research in the future. At the same time, the public often does not realize that there are secondary answers to well-known questions that are available to the attention of the public [10].

Concerning the provisions of the Minkowski model, which represents the speed of light in the form of the world line at an angle of 45°C to the abscissa axis and the boundary of a space-time cone, in an alternative representation to this concept, the world line of a ray of light coincides with the line of one-dimensional space specifically at the origin emanating from the point of residence of a stationary observer at time $t=0$. In other words, this line goes directly through the origin of the observer's coordinate system and the point with the initial coordinates. This confirms the thesis that there is a connection of a photon exclusively with time, but by no means with space [2]. At the same time, it should be taken into account that time flows evenly for a static observer in an alternative model. For an observer who is in a dynamic state, when he moves in the direction from the observer who is at rest, time flows evenly, and when moving to a resting observer, such uniformity is lost. This allows a static observer to conclude that the object is gradually accelerating as it moves towards him.

Any event can be a logical consequence or cause of another event taking into account a time interval for the signal to pass between two given events. In particular, when the light is turned on at a distance of three magnitudes of length from a static observer, the movement of this light signal will take exactly three units of time, and this signal will be visible to the observer no earlier than through these three-time units. Until the time interval expires, the observer will be unaware of the very fact of turning on the light source [11].

In science, the temporal concept exists in close relationship with the principle of causality, which is used to order causal events within a certain period. In a substantial to temporal concept, a certain, previously established order acts as a primary factor and is introduced as a separate, independent postulate. Within the limits of the relativistic concept, for the consistent definition of a given temporal order, it is not the fact of establishment itself that is accepted, but the "fundamental possibility of establishing" a causal relationship between subjects and phenomena in the time field.

Since causes precede the effects in all situations, it becomes quite obvious that an introduction and an expanded understanding of the so-called temporal order is required to determine a given order of occurrence of the cause. At the same time, a strong connection should be taken into account between spatial and temporal characteristics. There is a close connection between these characteristics and the causal characteristic [12]. At the same time, for the entire temporal order, the concept of time in the present refers to the entire space, while in the causal aspect; the term "present" will refer to the event and its consequences. In this context, it is possible to formulate and suggest that in order to obtain objective and maximally complete information about the event and the nature of its course; it is not enough just to expect a signal (coming from the event-cause). To do this, a static observer should recognize information, relative to whom all phenomena occur in the system of its measurement: to send a signal to an event with a high probability of its return, or to agree in advance on the use of a certain system of signals from the observed system.

In particular, to determine the exact distance of the mirror from the observer, it is enough to direct a beam of light to a certain point, after reflection from which the beam will return and the time of its movement will become the estimated time of the experiment. It is necessary to pay attention to the fact that there is a coincidence of the world line of the beam velocity with the speed of light with the main spatial axis. From the point of view of the cause, it is not possible to obtain any information about the ray of light until it meets the observer [13]. Only after this meeting, it becomes possible to control the speed of movement of the light beam from the point of direction to the end.

Obtaining objective information about the nature of the relationship between spatial and temporal characteristics requires a certain amount of time, and its duration depends both on the speed of information dissemination and on the final location of the event. Any information that can be obtained by observing space-time relationships determines the results that can be obtained only if all experimental conditions are met, and these results are in full accordance with the basic postulates of the special theory of relativity.

In modern conditions, the search for new and discussion of existing, well-known consequences of the special theory of relativity, in particular, such as the search and propagation of gravity waves, the reflection of electromagnetic waves by objects of large size, and other consequences that have a significant impact on the resolution of problems of astrogation, can be manifested in various aspects of the influence on the processes of electromagnetic radiation propagation on the scale of space objects and should be taken into account when forming a more accurate space-time interpretation of events [14].

To date, there is a development of the trend of practical application of the principles of special relativity in various fields of science and technology, in particular, in electrodynamics and other scientific disciplines directly related to the theory of the electromagnetic field. In addition, this circumstance largely causes an increase in interest in conducting experimental verification of the basic equations of electrodynamics with different characteristics of the motion of media and in systems with different numbers of measurements. From the point of view of obtaining the possibility of conducting such experiments, in the very near future we should expect the identification of optimal spatio-temporal characteristics in terms of improving the quality of such experiments and the possibility of practical solutions with their help to actual problems of modern science and technology.

Various theories representing the categories of space and time and giving concrete ideas about their properties and most important characteristics contribute to the emergence of many physical interpretations of the true nature of these quantities [15]. The situation radically changes from the subjectivization of the parameters under consideration to the recognition of space and time as a fundamental category of any matter. To date, no scientific discipline, be it philosophy, physics, chemistry or higher mathematics has formed and presented clear definitions regarding the essence of the concepts of space and time and their physical meaning. Despite all these scientific disciplines, like many others, widely use these concepts. It should be noted that today the concepts of space and time play such an important role in the process of modern physical cognition that there is no such physical process that could be described qualitatively without the use of these categories. All scientific disciplines that exist today always strive for the highest quality representation of meaning, therefore, the importance of displaying the physical meaning of the concepts of space and time will not lose relevance in the context of the formation of new and interpretation of old scientific postulates [16].

The space-time characteristics indicated in Minkowski's research are only physical images, physical and mathematical concepts that are devoid of the properties of objective reality. The basic provisions of the geometry of real space and time can be determined by the characteristics of the motion of matter, as well as the entire spectrum of interaction of a material nature. Since the main characteristic of the space-time continuum is the ability to move, various variations of movement, as well as interactions of a purely material nature, determine a set of certain space-time characteristics [17]. For example, the so-called Minkowski space qualitatively reflects the metric characteristics of time and space, which can be caused by interactions of the electromagnetic order.

Within the framework of special relativity, the categories of space and time can be expressed as "pseudo-Euclidean diversity". Such a circumstance determines one of the fundamental differences between temporal and spatial coordinates. This is the Lorentz translation invariance of time and space. From this circumstance, the fundamental effects of the special theory of relativity directly follow, such as the relativity of length and duration, and the relativity of the simultaneous flow of various events occurring at different points in space [18].

It is appropriate to note the prevailing interpretation of the status of the property of space and time in modern relativistic physics. The principles of the special theory of relativity affirm the physical meaning of the interval of space and time, while essentially performing the opposition of the relative nature of the intervals of time and space in their constant connection with motion. Considering the greatest value of the speed of light as the limiting speed of any physical interaction, this theory has clearly demonstrated that any cause-and-effect relationships between physical phenomena and quantities cannot be realized without establishing the dependence between various aspects of the coordination of these physical quantities in the space-time field [19]. The connection between any two events can be established only if the light radiation between them passes a greater distance than there is a geometric distance, or passes a similar distance. In all other cases, these two events cannot be considered connected by a spatio-temporal connection, since excessively large distances between them and moments of the message should be taken into account.

Conclusions

The conducted scientific study of alternative ideas about the characteristics of space and time from the point of view of the fundamental principles of comparative relativity theory led to the following conclusions.

An alternative model of ideas about the properties of space-time acts as a model of a private subjective substance “observer-space-time”, which includes the observer as an integral part of the general model. At the same time, there is an inextricable connection between alternative ideas about the space-time continuum and the absolute space-time, which is in a state of constant expansion, where, in the presence of a three-dimensional Euclidean space, the absolute parameter of time has an isotropic, one-dimensional characteristic and any spatial point different from others retains the same characteristic of time at every moment. At the same time, the existence of an alternative space-time continuum begins immediately at the beginning of the experiment, since in this context there is a control of current events, subject to the creation of a preliminary agreement on options for obtaining information about events that have already occurred or without it, which affects the quality of the final information. Alternative ideas about the properties of space and time do not exclude the simultaneous existence of the past and the present. At the same time, the three-dimensionality of the time parameter determines its causal nature and close relationship with the temporal nature of the categories of space and time.

The light beam moving from the observer has no connection with time, it is connected exclusively only with space. When moving towards the observer, his connection with time is also evident. Time is anisotropic, as well as alternative space-time. All cause-and-effect relationships proceed with strict reference to time, since from the event that is the cause to the event that is the consequence, information is transmitted uniformly, at the same speed. With the described variant of obtaining information, it is not possible to notice any changes in the development of events around the observer. Instantaneous conclusions about remote events give results that are absolutely consistent with the principles of relativity theory. The model clearly demonstrates the geometry of space-time, as well as the cause of such information distortions.

References

[1] Pennec X, Sommer S, Fletcher T. Riemannian geometric statistics in medical image analysis. London: Academic Press; 2019.

[2] Bonito A. Nochetto R. Geometric partial differential equations. Amsterdam: North Holland; 2020.

[3] Ungar A. Beyond pseudo-rotations in pseudo-euclidean spaces. London: Academic Press; 2018.

[4] Christakos G. Spatiotemporal random fields. Oxford: Elsevier; 2017.

[5] Azimov D. Analytical solutions for extremal space trajectories. Oxford: Butterworth-Heinemann; 2017.

[6] Morgan F. Geometric measure theory. London: Academic Press; 2016.

[7] Hassani S. Special relativity. Oxford: Elsevier; 2017.

[8] Kogut J. Special relativity, electrodynamics, and general relativity. London: Academic Press; 2018.

[9] Gladyshev VO, Duffy MK, Morozov AN, Rowlands P, Gladysheva TM. Progress in the development of the theory of relativity and its physical interpretations. *B. of the Mos. St. Techn. Univ. named after N.E. Baum.* 2005;(4):109-23.

[10] Tolstykh VN. Unrecognized theories and their authors. *Par.: Philosoph. and Cul. Alm.* 2016;(8):149-63.

[11] Alho A, Calogero S. A stellar model with diffusion in general relativity. *J. of Geom. and Phys.* 2017;(120):62-2.

[12] McClain T. A global version of Günther’s polysymplectic formalism using vertical projections. *J. of Geom. and Phys*. 2021;(161):article number 104065.

[13] Leifer P. Inertial motion of the quantum self-interacting electron. *J. of Geom. and Phys*.2020;(151):article number 103637.

[14] Siddiqui AN, Murathan C, Siddiqi MD. The Chen’s first inequality for submanifolds of statistical warped product manifolds. *J. of Geom. and Phys*. 2021;(169)article number 104344.

[15] Perelman CC. The geometrization of quantum mechanics, the nonlinear Klein–Gordon equation, Finsler gravity and phase spaces. *J. of Geom. and Phys*. 2021;(162):article number 104068.

[16] Nagihara S, Williams DR, Nakamura Y, Kiefer WS, McLaughlin SA, Taylor PT. Availability of previously lost data and metadata from the Apollo Lunar Surface Experiments Package (ALSEP). *Planet. and Sp. Sc.* 2020;(191):article number 105039.

[17] Ancillai M, Costanza G, Monache GD, Tata ME. Study and prototyping of a permanent magnetic suspension for the alignment by gravity of the elevation angle for the next generation lunar reflector experiment. *Planet. and Sp. Sc*. 2020;(192):article number 105049.

[18] Rising JM, Leveson NG. Systems-theoretic process analysis of space launch vehicles. *J. of Sp. Saf. Engineer.*, 2018;(5(3-4)):153-83.

[19] Siddiqi MD, De UC. Relativistic magneto-fluid spacetimes. *J. of Geom. and Phys.* 2020;(170):article number 104370.

Альтернативна репрезентація простору та часу: геометричне розв'язання задач теорії відносності

Юрій Миколайович Шинкарюк

Науково-виробниче підприємство "Сілверхорст"
04071, вул. Введенська, 26, м. Київ, Україна

Анотація

Актуальність. Актуальність даного наукового дослідження зумовлена важливістю теоретичних питань альтернативного представлення категорій простору і часу з точки зору розробки геометричних розв'язків проблем теорії відносності, які є важливими у вирішенні багатьох практичних проблем, що виникають у різних галузях сучасної науки і техніки.

Мета. Метою даної роботи є формування альтернативного погляду на категорії простору і часу, що мають важливе практичне значення для створення геометричних розв'язків проблем, які відображають окремі принципи теорії відносності.

Методи. В основу методологічного підходу до побудови дослідницької роботи в даній науковій праці було покладено поєднання системного аналізу особливостей складання альтернативного представлення категорій простору і часу з аналітичним дослідженням особливостей побудови геометричних рішень проблем, що відображають різні аспекти загальної теорії відносності.

Результати. Результати даної дослідницької роботи відображають весь хід наукових досліджень і свідчать про відсутність протиріч у самому факті існування альтернативних просторово-часових моделей, як таких, що не відповідають фундаментальним принципам спеціальної теорії відносності.

Висновки. Результати та висновки цього дослідження мають важливе практичне значення з точки зору формування нових уявлень про положення спеціальної теорії відносності та можливості практичного використання геометричних моделей для вирішення складних проблем цієї теорії шляхом використання відкоригованих уявлень про реальні властивості простору і часу, а також мають важливе значення для співробітників конструкторських бюро, які займаються розробкою новітніх зразків високотехнологічної продукції і використовують у своїх розрахунках принципи спеціальної теорії відносності

Ключові слова: фізичні теорії, простір, геометричні аспекти, наука, наукові концепції

Scientific Herald of Uzhhorod University
Series “Physics”

Journal homepage: https://physics.uz.ua/en

Issue 51, 83-86

Received: 12.04.2022. Revised: 23.05.2022. Accepted: 03.06.2022

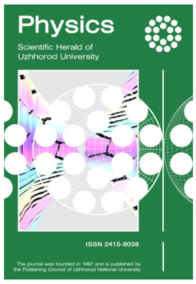

UDC 539.1
PACS 12.00.00
DOI: 10.54919/2415-8038.2022.51.83-86

Uzhhorod School of Atomic Physics and Quantum Electronics

Anna Gomonai*, Victoria Roman, Anatolij Zavilopulo

Institute of Electron Physics of the NAS of Ukraine
88017, 21 Universytetska Str., Uzhhorod, Ukraine

Abstract

This work is dedicated to the centenary of Ivan Prokhorovych Zapisochny, a well-known Ukrainian scientist in the field of atomic physics, physical and quantum electronics, Honored Scientist of Ukraine, laureate of the State Award of Ukraine in the field of science and technology and the Sinelnikov Award of the National Academy of Sciences of Ukraine. His name is associated with important results that contributed to the development of physics of electron and atomic collisions, vacuum-ultraviolet spectroscopy, nonlinear optics, electron-photon and ion-photon emission of metal surfaces, and quantum gas electronics. He and his disciples have a great merit in the creation of a whole series of original, sometimes unique, experimental setups and high-precision instruments for the study of numerous novel phenomena and effects in electron shells of atoms and ions at their collisions with electrons, laser-emitted photons and with each other as well as of atomic processes at interaction of electron, ion, and laser beams with solid surfaces and active media of metal vapor lasers and excimer molecules

Keywords: I.P. Zapisochny, school of atomic physics, quantum electronics

Вітчизняна наука в останні роки відчула серйозні виклики, які поставили її на межу виживання. Але навіть зараз, у період повномасштабної війни, коли наша держава переживає надзвичайно складний, болісний та важливий період боротьби за власну незалежність, право на свободу, право на життя у цивілізованому європейському суспільстві, українські науковці продовжують отримувати результати світового рівня. І саме сьогодні, як ніколи, важливим є продовження роботи на шляху до підготовки конкурентоспроможних, високоосвічених українських учених, а також підтримка пам’яті тих учених, які прославили Україну на весь світ та започаткували цілі напрями наукового дослідження. Саме тому, Інститутом електронної фізики НАН України 26-27 травня 2022 року було проведено Міжнародну наукову конференцію, присвячену 100-річчю від дня народження професора Івана Прохоровича Запісочного [1] (рис. 1).

Рисунок 1. Іван Прохорович Запісочний (1922–2001)

Suggested Citation:
Gomonai A, Roman V, Zavilopulo A. Uzhhorod school of atomic physics and quantum electronics. *Scientific Herald of Uzhhorod University. Series “Physics”*. 2022;(51):83-86.

*Corresponding author

З ініціативи І.П. Запісочного та завдяки його наполегливої науково-організаційної діяльності було не тільки засновано та розвинуто ужгородську наукову школу з атомної та квантової електроніки, а й у подальшому створено першу та єдину на Закарпатті академічну установу – Інститут електронної фізики НАН України. Це було результатом втілення плану організації центрів академічної науки в західних областях України, забезпечення високого рівня досліджень та налагодження транскордонного наукового співробітництва з вченими сусідніх держав. Наявний науковий доробок, інтелектуальний і кадровий потенціал, традиції, сформовані за весь період діяльності окремих академічних установ: відділу фотоядерних процесів Інституту фізики АН УРСР (вересень 1969 р.) та відділу теорії адронів Інституту теоретичної фізики АН УРСР (січень 1970 р.) – стали золотим фондом академічної науки на Закарпатті [2].

Варто наголосити, що передумовами відкриття першої на Закарпатті академічної установи були також всебічний розвиток і вагомі наукові досягнення фізиків Ужгородського державного університету та його провідних професорів: Ю.М. Ломсадзе, В.О. Шкоди-Ульянова, Д.В. Чепура, В.І. Лендєла – очільників кафедр теоретичної фізики, ядерної фізики та фізики напівпровідників, які разом зі студентами старших курсів і аспірантами в Ужгородському державному університеті (тепер національному) розпочали фундаментальні дослідження з актуальних проблем теоретичної фізики, ядерної фізики і фізики твердого тіла.

На сьогодні в Інституті електронної фізики НАН України ефективно працює чотири наукових відділи, в яких проводяться дослідження з актуальних проблем фізики та суміжних наук:

- фізики фотонних, електронних, іонних та атомних зіткнень,
- низькоенергетичної ядерної фізики,
- радіаційної і техногенно-екологічної безпеки,
- фізики лазерів на парах металів,
- оптичного приладобудування,
- фізико-хімічних основ і технології отримання, оброблення та застосування макроскопічних і мезоскопічних кристалів, плівок та склоподібних матеріалів.

На базі Інституту створено Центр колективного користування приладами «Лазерний спектроскопічний комплекс», метою якого є найбільш раціональне використання унікального, коштовного наукового обладнання та надання науково-технічних послуг всім зацікавленим вітчизняним та закордонним організаціям. Унікальним приладом є ядерно-фізична установка – мікротрон М-30. Це практично єдина в Україні установка з сертифікованим стендом для прикладних досліджень, зокрема у галузях космічного приладобудування, фізики реакторів, дозиметрії інтенсивних радіаційних полів, активаційного аналізу, а також радіаційної і техногенно-екологічної безпеки (рис. 2).

Рисунок 2. Інститут електронної фізики НАН України

Визначну роль у здобутті наукового авторитету Інституту протягом всіх років його існування відіграло регулярне проведення різних наукових форумів. Інститут був ініціатором і організатором понад 40 міжнародних наукових заходів. Одними з перших були: семінар-трикутник Ужгород – Дебрецен – Мішкольц, проведений у 1992 році, конференція, присвячена 75-річчю Академії наук України (1993 рік), міжнародний семінар «HADRONS-94», міжнародна нарада «Сучасні технології в медицині» (1994 рік). У 1997 році Інститут організував і провів конференцію «The Centenary of Electron» (EL-100), присвячену 100-річчю відкриття електрона, та був співорганізатором конференції “Неевклідова геометрія в сучасній фізиці”, яка з тих пір регулярно проводиться кожні два роки. У 2000 році Інститут започаткував Міжнародну конференцію «Елементарні процеси в атомних системах» (CEPAS), яка з тих пір проводиться кожні три роки і вже відбулася успішно у Гданську (Польща), Мішкольці (Угорщина), Клужі-Напоці (Румунія), Белграді (Сербія) та Братиславі (Словаччина). Знаменною подією 2021 року, в скрутні часи пандемії COVID-19, стало проведення Інститутом двох міжнародних наукових он-лайн форумів – Міжнародної конференції молодих учених та аспірантів «ІЕФ-2021» та Міжнародної конференції «50 років академічної науки на Закарпатті».

Цьогорічна конференція [3], яка присвячена ініціатору створення нашого Інституту, у зв'язку з військовим станом також була проведена онлайн, але цікавість до конференції від цього не згасла, а навпаки, розширила географію учасників. Обидва пленарні засідання були насичені цікавими доповідями та жвавими дискусіями учасників, які представили 75 доповідей від 200 співавторів. Серед учасників були як провідні вчені наукових установ НАН України та закладів вищої освіти, так і аспіранти й студенти та навіть школярі з різних міст України та зарубіжжя. Зокрема, з Києва, Харкова, Ужгорода, Сум, Дніпра, Чернігова, Дрогобича, Мукачева. Особливо приємно відзначити участь у роботі конференції провідних науковців з Німеччини, Польщі, Молдови, Японії, Франції, Італії, Сполучених штатів Америки, Китаю, Словаччини та Литви. Високий рівень представлених результатів показав, що напрями, які колись започаткував в Ужгороді Іван Прохорович Запісочний, є актуальними та широко досліджуваними і сьогодні (рис. 3).

Рисунок 3. Співробітники ІЕФ НАН України – учасники міжнародної онлайн конференції «Ужгородська школа з атомної фізики та квантової електроніки»

Відкрила конференцію директор Інституту, член-кореспондент НАН України Ганна Гомонай, яка озвучила вітання президента НАН України, академіка Анатолія Загороднього та академіка-секретаря Відділення фізики і астрономії НАН України, академіка Вадима Локтєва. У своїй доповіді Ганна Гомонай окреслила основні віхи життєвого шляху І.П. Запісочного – ученого і педагога, людини, яка помітно вплинула на хід подій, на життя і долю тих, хто був поруч. Зі спогадами про засновника на Закарпатті школи з атомної фізики і квантової електроніки, широко відомої й визнаної у всесвітній спільноті фізиків, виступили також професори ДВНЗ «Ужгородський національний університет» Людвик Шимон та Іван Шафраньош. Не менш цікавою була доповідь професора Університету Небраски-Лінкольна (США) Іллі Фабриканта про історію академічної науки Латвії та її зв'язок з професором І.П. Запісочним. У роботі конференції взяли участь також представники молодшого покоління наукової школи професора І.П. Запісочного, випускники аспірантури Інституту електронної фізики НАН України: Оксана Плекан (Італія), Віталій Феєр (Німеччина), Шандор Демеш (Франція) та Анна Островерх (м. Київ, Україна). Родзинкою конференції стали яскраві виступи наукового співробітника Харківського національного університету імені В.Н. Каразіна Олега Єрмакова та його учнів – студента Артема Гринченка (ХНУ ім. В.Н. Каразіна, Харків) та школярки Варвари Хміль (СЗШ №329 «Логос», Київ), які показали, що для науки немає віку та меж, а науковий шлях для людини може розпочатися ще в школі – через якісне викладання предметів і проведення невеликих досліджень разом з наставником. А найбільш цінним для всіх учасників було почути виступи науковців із найгарячіших точок російсько-української війни – Харкова, Сум та Дніпра, які показали своїм прикладом, що українців не здолати, незважаючи ні на що ми продовжуємо працювати, творити та розвивати нашу рідну Україну.

Список використаних джерел

[1] Запісочний ІП. Шлях у науку. Спогади. Ужгород: Мистецька лінія; 2002. 70 с.

[2] Гомонай ГМ, Завілопуло АМ. Вісн. НАН України, 2022;(5):77–86. doi: 10.15407/visn2022.05.077.

[3] Завілопуло АМ, Роман ВІ. Ужгородська школа з атомної фізики та квантової електроніки. До 100-річчя від дня народження професора Івана Прохоровича Запісочного; 2022 Трав 26-27; Ужгород. Ужгород: Видавництво ФОП Сабов А.М.; 350 с.

Ужгородська школа з атомної фізики та квантової електроніки

Гомонай Ганна Миколаївна, Вікторія Іванівна Роман,
Анатолій Миколайович Завілопуло

Інститут електронної фізики НАН України
88017, вул. Університетська, 21, м. Ужгород, Україна

Анотація

Ця робота присвячена знаменній ювілейній даті – 100-річчю від дня народження Івана Прохоровича Запісочного, відомого українського вченого в галузі атомної фізики, фізичної і квантової електроніки, заслуженого діяча науки України, лауреата Державної премії України в галузі науки і техніки та премії ім. К.Д. Синельникова НАН України. З його ім'ям пов'язані важливі результати, які сприяли розвитку фізики електронних і атомних зіткнень, спектроскопії вакуумно-ультрафіолетового діапазону, нелінійної оптики, електрон-фотонної та іон-фотонної емісії металевих поверхонь, газової квантової електроніки. Наукова школа І.П. Запісочного має великі заслуги у створенні цілої серії оригінальних, у тому числі унікальних, установок та прецизійного інструментарію для досліджень багатьох нових явищ і ефектів в електронних оболонках атомів і іонів при їх зіткненнях з електронами, фотонами лазерного випромінювання та між собою, досліджень атомних процесів при взаємодії електронних, іонних і лазерних пучків з поверхнею твердих тіл та активних середовищ лазерів на парах металів і ексимерних молекулах

Ключові слова: І.П. Запісочний, наукова школа з атомної фізики, квантова електроніка

НАУКОВИЙ ВІСНИК
УЖГОРОДСЬКОГО УНІВЕРСИТЕТУ
СЕРІЯ «ФІЗИКА»

Науковий журнал

Випуск 51. 2022

Заснований у 1997 р. Виходить двічі на рік

Оригінал-макет видання виготовлено
у редакційно-видавничому відділі Ужгородського національного університету

Редагування англомовних текстів:
С. Воровський, К. Касьянов

Комп'ютерна верстка:
К. Сосєдко

Підписано до друку 21.06.2022 р. Формат 60*84/8
Умовн. друк. арк. 10,2
Наклад 300 примірників

Адреса видавництва:
ДВНЗ «Ужгородський національний університет»
88000, вул. Волошина, 54, м. Ужгород
Закарпатська область, Україна
тел/факс: (03122) 3-20-24
E-mail: info@physics.uz.ua
www: https://physics.uz.ua/uk

SCIENTIFIC HERALD
OF UZHHOROD UNIVERSITY
SERIES “PHYSICS”

Scientific Journal

Issue 51. 2022

Founded in 1997. Published two times per year

The original layout of the publication is made
in the publishing department of Uzhhorod National University

Editing English-language texts:
S. Vorovsky, K. Kasianov

Desktop publishing:
K. Sosiedko

Signed for print 06/21/2022. Format 60*84/8
Conventional printed pages 10.2
Circulation 300 copies

Publishing Address:
Uzhhorod National University
88000, 54 Voloshyn Str., Uzhhorod
Transcarpathian region, Ukraine
Tel./fax: (03122) 3-20-24
E-mail: info@physics.uz.ua
www: https://physics.uz.ua/en